

GRAPHENE NEAR COMMENSURATION

A Dissertation
Presented to
The Academic Faculty

By

Stephen Spitz

In Partial Fulfillment
of the Requirements for the Degree
Doctor of Philosophy in the
School of Physics

Georgia Institute of Technology

May 2018

Copyright © Stephen Spitz 2018

GRAPHENE NEAR COMMENSURATION

Approved by:

Dr. Markus Kindermann, Advisor
School of Physics
Georgia Institute of Technology

Dr. Phillip N. First
School of Physics
Georgia Institute of Technology

Dr. Michael Pustilnik
School of Physics
Georgia Institute of Technology

Dr. Andrew Zangwill
School of Physics
Georgia Institute of Technology

Dr. Martin Short
School of Mathematics
Georgia Institute of Technology

Date Approved: March 30, 2018

There is nothing new to be discovered in physics now.

Lord Kelvin

To Lord Kelvin.

ACKNOWLEDGEMENTS

There are many people I must acknowledge for making this dissertation possible. First, thanks goes to my family for supporting me throughout my education on the long journey to a doctorate degree. Second, I thank my advisor, Dr. Markus Kindermann, for his introduction to a fascinating topic and his guidance through the research process. Finally, I'll always recall with fondness my fellow physics students. Completing my studies without their comradeship would have been no fun indeed.

I acknowledge NSF grant DMR-1055799 for support in completing this work.

TABLE OF CONTENTS

Acknowledgments	v
List of Figures	x
Summary	xiv
Chapter 1: Introduction	1
1.1 History of Graphene	1
1.2 Graphene Theory	2
1.3 Topology and Chern Number	5
1.4 Domain Walls	6
1.5 Valley Chern Number	7
Chapter 2: Bilayer Graphene	8
2.1 Bilayer Hamiltonian	8
2.2 Commensuration	9
2.3 Continuum Model	13
2.3.1 Perturbation Theory	14
2.3.2 Direct Coupling	16
2.3.3 Indirect Coupling	20

2.3.4	Non-perturbative Coupling	24
2.4	Summary	26
Chapter 3: Bilayer Graphene Near Commensuration		27
3.1	Available Tools	27
3.2	Local Lattice Stacking	29
3.2.1	Real Space Hamiltonian	32
3.2.2	Gauge Field Analysis	35
3.2.3	Network Models	37
3.3	Network Model: Near Zero Degrees	38
3.3.1	Semi-classical Picture	38
3.3.2	Network Model	41
3.4	Network Model: Near 38.2°	41
3.4.1	Gauge Fields	42
3.4.2	Network Model	47
3.4.3	Momentum Space Verification	52
3.4.4	Tight Binding Verification	56
Chapter 4: Peierls Transition Near 0°		67
4.1	Peierls Transition Theory	67
4.2	Analytic Framework	69
4.3	Mass Term	70
4.4	Peierls Transition	75

Chapter 5: Non-Perturbative Peierls Transition	79
5.1 Scaling Argument	79
5.2 Effective Model	81
5.2.1 Added Phase	82
5.2.2 Distorted Flat Band	84
5.3 In-Plane Phonon	85
5.3.1 Electronic Energy	87
5.3.2 Elastic Energy	88
5.3.3 Calculations	89
5.3.4 Verification of Phase Theory	98
5.4 Peierls Transition in an Electric Field	101
5.4.1 Electronic Energy	102
5.4.2 Elastic Energy	103
5.4.3 Calculations	103
5.4.4 Verification	107
5.5 Summary	109
Chapter 6: Conclusion	111
Appendix A: Physical Constants of Graphene	113
Appendix B: Gauge Fields Near 0°	114
Appendix C: Gauge Fields Near 38.2°	115

Symbol Index	119
References	122

LIST OF FIGURES

1.1	Graphene Lattice. The blue atoms are sublattice A and the red atoms are sublattice B.	2
1.2	Top view of Brillouin zone of graphene with inequivalent Dirac points (left). Dirac cone at the circled Dirac point viewed from the side (right).	4
2.1	Number of atoms in a commensurate bilayer of given angle. Even commensurations are red, odd commensurations are blue.	10
2.2	4 Atom Commensurations	10
2.3	28 Atom Commensurations	11
2.4	Dirac point connection for even and odd commensurations	12
2.5	28 Atom Commensurations	12
2.6	Even commensuration showing BZ of each layer and a solution to the coupling equation.	18
2.7	Indirect coupling through $\theta = 0^\circ$ commensuration term. The dashed arrows point from the Dirac point of layer two to the states of layer two that will couple to the Dirac point of layer one.	21
2.8	Indirect coupling through $\theta = 38.2^\circ$ commensuration term. The dashed arrows point from the Dirac point of layer two to the states of layer two that will couple to the Dirac point of layer one.	22
2.9	Schematic of twist angle. Each commensurate angle has a zone of influence where the effect is perturbative (blue) and non-perturbative (red).	25

3.1	Renormalization of the Fermi velocity as $\theta \rightarrow 0$. We see a series of magic angles with zero velocity.	28
3.2	The gray lines are the supercell for a bilayer very near 0° . The circles show a magnified view of regions of AA, AB, and BA stacking.	29
3.3	Decomposition of a rotation into a rotation plus a translation.	30
3.4	Magnitude of A_0 , A_z , A_x , and A_y of a near 0° commensuration. In each case there are 30 equally spaced contours in the given range in units of $\tilde{\gamma}_0$.	39
3.5	Semi-classically allowed states near 0° with $V_0 = \tilde{\gamma}_0$. Yellow regions have zero energy states. Blue regions do not.	40
3.6	Topological midgap states at AB/BA domain boundary. A tight binding calculation was performed on a strip of graphene. On the left is the strip with no domain wall. On the right is the strip with the domain wall. The two gap states are clearly visible. The additional midgap states are localized to the edge of the strip and will not show up in a continuous sample.	41
3.7	Magnitude of A_0 , A_z , A_x , and A_y of a near 38° commensuration. In each case there are 30 equally spaced contours in the given range in units of $\tilde{\gamma}_{38}$. .	43
3.8	Semi-classically allowed states near 38.2° . Yellow regions have zero energy states. Blue regions do not.	44
3.9	Local band structure along the line of degeneracy. Top left is one node and bottom right is the other node.	45
3.10	Two lowest energy bands midway on the link (blue), slightly away in the perpendicular direction to the link (yellow), and farther away (green).	46
3.11	Berry curvature at the Dirac point on either side of the degenerate line. The left panel is on the left of the degenerate line, and the right panel is on the right of the degenerate line. The curvature changes sign in each psuedovalley across the line.	46
3.12	Topological midgap states at domain boundary of near 38.2° bilayer. Inter-layer coupling is exaggerated for clarity.	47
3.13	A schematic of the network model. Six midgap states scatter amongst the nodes of a honeycomb lattice defined by SE odd regions.	48

3.14	Bands from the network model with $\lambda \in [0, 2\pi/3)$. The plotted values are the phase ϵ from Equation 3.27. This unitless phase is independent of system size. To convert to energy, it is necessary to multiply by a factor of v/L , where L is the length of a link.	53
3.15	Three dimensional plot of the network model bands with $\lambda = 1.3$. The Kagome structure of the bands is clear.	54
3.16	Bandstructure of a near 38.2° bilayer, as described by a momentum space matrix coupling the 818 lowest energy states of the separate graphene layers.	55
3.17	Fourier components of realistic coupling (blue) and artificial coupling (yellow). The red lines are the momenta corresponding to 0° and 38° commensuration effects.	57
3.18	Lowest energy eigenvector of commensuration at $\theta = 38.546^\circ$ with artificial coupling. $\gamma = .2t$. The red lines are the supercell.	58
3.19	Lowest energy bands of commensuration at $\theta = 38.546^\circ$ with artificial coupling.	60
3.20	Bands from the network model with $\lambda = \pi/2$ and $p \in [\pi/2, \pi]$	61
3.21	Set of low energy eigenvectors of commensuration at $\theta = 38.546^\circ$ with artificial coupling. $\gamma = .2t$. The red lines are the supercell.	63
4.1	Schematic of two Dirac cones shifted by opposite V_0 . On the left, the cones do not interact. On the right, they interact with a mass gap along the Dirac circle.	69
4.2	Phonon for a system at 11.6°	72
4.3	Gap induced by the phonon for a system at 11.6° . The solid line is the prediction derived in the text.	76
5.1	Schematic of near 38.2° with (right) and without (left) added phase on the links. The flat band undergoes a distortion.	79
5.2	Local band structure along the line of degeneracy. Top left is one node and bottom right is the other node.	81
5.3	Momentum of a zero energy state with (blue) and without (yellow) \mathbf{A}_0	83

5.4	Distortion of flat band predicted by the network model when $\delta\psi_1 = -\delta\psi_2 = .2$ and $\delta\psi_1 = 0$. We use $\lambda = 1.3$. Note axes are not orthogonal.	86
5.5	Extended phonon for system at 38.57°	90
5.6	Distortion of the network caused by background phonon flow. Dashed lines are the undistorted network. Black lines are the distorted network. System is at 38.57°	91
5.7	Localized phonon for system at 38.57°	97
5.8	Phase along a link with (yellow) and without (blue) the phonon. Parameters are exaggerated.	97
5.9	Flat band distortion for system at 38.57°	100
5.10	Predicted (solid) and measured bandwidth as a function of \tilde{l}_0	101
5.11	Extended phonon throughout the supercell. Displacement of both graphene layers is out of the page.	104
5.12	Flat band distortion for system at 38.6°	108
5.13	Predicted (solid) and measured bandwidth as a function of V_0	109

SUMMARY

For the past decade, graphene has been among the most heavily researched materials in condensed matter physics. In particular, its unusual electronic properties have spurred researchers to investigate new applications and theoretical insights. In this thesis, we focus on a system consisting of two sheets of graphene at a relative twist angle. The physics of this system has proved surprisingly rich and non-trivial. We summarize the current state of theoretical work on this system and extend this theory to cover a new twist angle regime, finding an exotic flat band state in the process. Finally, we investigate the possibility of Peierls-like transitions in all regimes.

CHAPTER 1

INTRODUCTION

1.1 History of Graphene

Graphene is a single layer of carbon atoms arranged in a honeycomb lattice. Its electrical properties were first studied in an effort to approximate graphite as independent layers of graphene [1].

Around 2004-2005, several groups managed to isolate few layer and single layer graphene [3–6]. A number of remarkable properties emerged, the most interesting being a linear dispersion relation. At energies near the Fermi level, the dispersion of electrons is governed by the massless Dirac equation.

Interest in single and few layer graphene rapidly expanded. The most obvious application was incorporating graphene into electrical circuits using, for instance, graphene transistors [7, 8]. However, there has also been copious theoretical work. Examples include tests of previously inaccessible high energy theory, integer and fractional quantum hall effects, and topological insulators [9–11].

In growing graphene, the result is typically several layers in a stack. Some methods result in layers that are rotated relative to one another, so called twisted multilayers or turbostratic graphene [12, 13]. Twisted bilayers provide a good model for twisted multilayers. Understanding twisted bilayers has proven key to understanding results from these experiments. In particular, it resolved the puzzle of how stacked graphene layers appear electronically uncoupled [14]. The problem also proved surprisingly non-trivial from a theoretical perspective. In the future, we may be able to exploit twist angle as a new degree of freedom to access novel physics and applications.

In this thesis, we first review the current state of twisted bilayer theory. Then we use

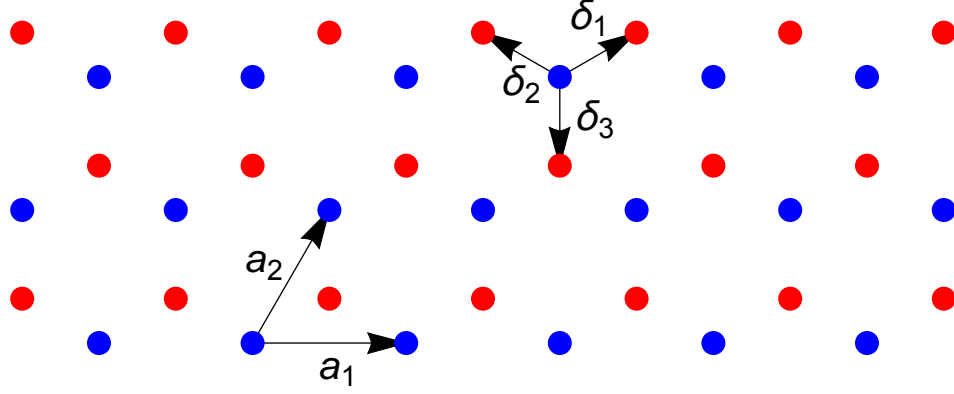


Figure 1.1: Graphene Lattice. The blue atoms are sublattice A and the red atoms are sublattice B.

this theory to explore two new ideas. First, we predict, find, and explain localization of low energy states at certain large rotation angles. Second, we examine the possibility of a Peierls transition.

1.2 Graphene Theory

Graphene is a two dimensional crystal of carbon atoms arranged in a honeycomb lattice. A portion of a graphene lattice is shown in Figure 1.1. The lattice consists of two sublattices, called the A and B sublattices. These are shown in red and blue in the figure. The basic properties of graphene can be derived from tight binding models. Details can be found in [15, 16].

In this thesis, \mathbf{a}_i denote the two lattice vectors, δ_i denote the three nearest neighbor vectors, and \mathbf{b}_i denote the two reciprocal lattice vectors. We choose the following geometry:

$$\mathbf{a}_1 = a(1, 0) \quad \mathbf{a}_2 = a\left(\frac{1}{2}, \frac{\sqrt{3}}{2}\right) \quad (1.1a)$$

$$\mathbf{b}_1 = \frac{2\pi}{a}\left(1, -\frac{1}{\sqrt{3}}\right) \quad \mathbf{b}_2 = \frac{2\pi}{a}\left(0, \frac{2}{\sqrt{3}}\right) \quad (1.1b)$$

$$\delta_1 = \frac{a}{2} \left(1, \frac{1}{\sqrt{3}} \right) \quad \delta_2 = \frac{a}{2} \left(-1, \frac{1}{\sqrt{3}} \right) \quad \delta_3 = a \left(0, -\frac{1}{\sqrt{3}} \right), \quad (1.1c)$$

where $a = 2.46\text{\AA}$ is the lattice constant of graphene . We also define $\delta = a/\sqrt{3}$ to be the interatomic distance, that is, the distance between nearest neighbors . In real space, we call the Hamiltonian for the nearest neighbor tight binding model H_G :

$$H_G = t \sum_{i=1}^N \sum_{j=\langle i \rangle} a_{\sigma i}^\dagger a_{\bar{\sigma} j}, \quad (1.2)$$

indexHG@ H_G where $a_{\sigma i}$ is the field operator for sublattice σ and unit cell i . The notation $\langle i \rangle$ signifies the unit cells connected to unit cell i by a nearest neighbor vector. The notation $\bar{\sigma}$ indicates the opposite sublattice from σ . The parameter t denotes the energy of nearest neighbor hopping .

Now we write the Hamiltonian in momentum space. We use κ for the momentum . In all that follows, we will set $\hbar = 1$, so κ is also a point in the reciprocal space of the lattice. The field operators are written:

$$a_{\sigma i} = \frac{1}{\sqrt{N}} \sum_{\kappa} a_{\kappa \sigma} e^{i\kappa \mathbf{R}_{i\sigma}}, \quad (1.3)$$

where $\mathbf{R}_{i\sigma}$ is the position of atom i in sublattice σ . The number N is the number of cells in the sample indexN@ N . The operator $a_{\kappa \sigma}$ is the destruction operator for a state of momentum κ on sublattice σ . In this momentum basis, the Hamiltonian is diagonal:

$$H_G = t \sum_{\kappa \sigma} \sum_{j=0}^2 a_{\kappa \sigma}^\dagger a_{\kappa \bar{\sigma}} e^{i\kappa \delta_j (\delta_{\sigma A} - \delta_{\sigma B})}. \quad (1.4)$$

At the two momentum space points, $\mathbf{K}_{v=1} = \frac{1}{3}\mathbf{b}_1 + \frac{2}{3}\mathbf{b}_2$ and $\mathbf{K}_{v=2} = \frac{2}{3}\mathbf{b}_1 + \frac{1}{3}\mathbf{b}_2$, the eigenvalues are zero . These are called the Dirac points. Now we expand the Hamiltonian around the Dirac point v , substituting $\kappa = \mathbf{K}_v + \mathbf{k}$. That is, \mathbf{k} is momentum measured with

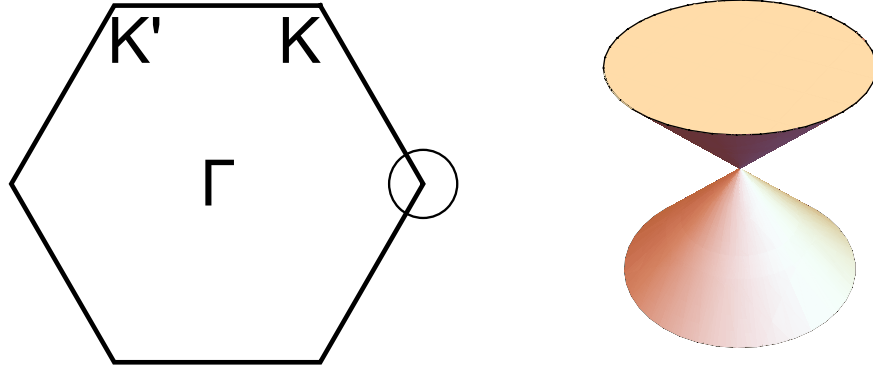


Figure 1.2: Top view of Brillouin zone of graphene with inequivalent Dirac points (left). Dirac cone at the circled Dirac point viewed from the side (right).

respect to the Dirac point . If we expand to first order in \mathbf{k} , we find:

$$H^{(v)}(k_x, k_y) = \frac{\sqrt{3}at}{2} \begin{pmatrix} 0 & e^{-\nu i 2\pi/3}(k_x - \nu i k_y) \\ * & 0 \end{pmatrix}, \quad (1.5)$$

where $\nu = \pm 1$ for $v = 1, 2$ respectively. The Hamiltonians $H^{(1)}$ and $H^{(2)}$ describe the physics near each of the Dirac points. We say graphene has two valleys, one for each Dirac point. The eigenvalues are clearly $\pm \sqrt{3}atk/2$ where k is the magnitude of distance to the Dirac point we choose to expand around. Thus, we see that near the Dirac points, the spectrum takes the form of two cones joined by a vertex at $E = 0$ with velocity $v = \sqrt{3}at/2$.

A schematic of the Brillouin Zone is shown in Figure 1.2. On the left, we see the hexagonal BZ with the two inequivalent Dirac points at the corners. On the right, we see an example of a Dirac cone which extends from each of the Dirac points.

For future convenience, we now define:

$$H^0 = vk [\cos(\phi - 2\pi/3)\sigma_x\tau_0 + \sin(\phi - 2\pi/3)\sigma_y\tau_z], \quad (1.6)$$

where k_x and k_y are now in the polar coordinates k and ϕ . We use σ for the Pauli matrices for the sublattice degree of freedom, and τ for the Pauli matrices for the valley degree of freedom. We use the representation:

$$\sigma_0 = \begin{pmatrix} 1 & 0 \\ 0 & 1 \end{pmatrix} \quad (1.7a)$$

$$\sigma_x = \begin{pmatrix} 0 & 1 \\ 1 & 0 \end{pmatrix} \quad (1.7b)$$

$$\sigma_y = \begin{pmatrix} 0 & -i \\ i & 0 \end{pmatrix} \quad (1.7c)$$

$$\sigma_z = \begin{pmatrix} 1 & 0 \\ 0 & -1 \end{pmatrix}. \quad (1.7d)$$

In other words, H^0 is the four dimensional Hamiltonian that describes the low energy theory at the two valleys.

1.3 Topology and Chern Number

We will make use of the topological index known as the Chern number. Thus, we give a brief definition for future reference. These ideas were first derived in [17] and a good reference is [18]. The Chern number is a topological index defined for any non-degenerate band. Given such a band with eigenvector $|n(\boldsymbol{\kappa})\rangle$ throughout the BZ, we define the Berry connection:

$$\mathbf{A}_C(\boldsymbol{\kappa}) = i \langle n(\boldsymbol{\kappa}) | \nabla_{\boldsymbol{\kappa}} | n(\boldsymbol{\kappa}) \rangle. \quad (1.8)$$

The Berry connection is not a gauge independent quantity. However, we may define the gauge independent Berry curvature:

$$\mathbf{B}_C(\boldsymbol{\kappa}) = \nabla_{\boldsymbol{\kappa}} \times \mathbf{A}_C(\boldsymbol{\kappa}). \quad (1.9)$$

Note, that in the case of a two dimensional system, we have the simplification:

$$B_C = 2\text{Im} \langle \partial_y n(\boldsymbol{\kappa}) | \partial_x n(\boldsymbol{\kappa}) \rangle. \quad (1.10)$$

The Chern number is then the integral of the curvature over the BZ:

$$C = \frac{1}{2\pi} \int_{\text{BZ}} B_C(\boldsymbol{\kappa}). \quad (1.11)$$

It is clear that the Chern number is quantized in integer units. The BZ has no boundary, and thus, an application of Stokes' Theorem gives $C = 0$ in the case where \mathbf{A}_C is differentiable throughout the BZ. If \mathbf{A}_C is not differentiable somewhere, we may divide the BZ into patches and use local gauges that ensure differentiability. Then we integrate the Berry connection over the boundaries of these patches. Over every boundary, we integrate in both directions, the only difference being a gauge. The difference in such integrals is the winding number of the gauge along the boundary and must be in units of 2π . Thus, the Chern number is quantized.

1.4 Domain Walls

The Chern number is a topological index that is robust to all continuous changes of the Hamiltonian that do not close the gap. As a topological index, we have an index theorem [19]. Consider a system with one region where $C = n$ and another region where $C = m$. The boundary of these regions is called a domain wall. The index theorem guarantees $n - m$ topologically protected midgap states along the domain wall. These states will propagate with some velocity, the sign of which is determined by the sign of $n - m$. In fact, this is the

origin of the Quantum Hall states that propagate along the edge of a topological insulator.

1.5 Valley Chern Number

In a system with Dirac valleys, like graphene, we may define another quantity called the valley Chern number [20]. This quantity originates with the observation that Berry curvature is localized to the valleys. If we evaluate the Chern number for a single valley in the continuum limit, we find the integrated Berry curvature over this valley is $C^v = \pm 1/2$, where we have the valley index, $v = 1, 2$. Note the Chern number is not quantized because the continuum limit is not periodic.

Now, we define the valley Chern number as the difference between the integrated Berry curvature of the two valleys:

$$C_v = C^1 - C^2. \quad (1.12)$$

For example, in monolayer graphene with constant mass, one valley contributes $1/2$ and the other valley contributes $-1/2$. Therefore, the Chern number of this system is zero, but the valley Chern number is one.

The same index theorem applies to the valley Chern number as the normal Chern number with the caveat that there must be no intervalley scattering. For instance, consider a sheet of graphene with real space mass such that we have a region of $C_v = 1$ and a region of $C_v = -1$. The normal Chern number is zero in both regions. However, the differing valley Chern number guarantees two topologically protected midgap states on the domain wall between the regions, provided the dynamics of the system is confined to the valleys, and there is no intervalley scattering.

CHAPTER 2

BILAYER GRAPHENE

Once we understand the spectrum of single layer graphene, we move to bilayer graphene. This is important because many growth methods result in multiple layers. In addition, as methods are developed to control twist angle [21], we can use this angle as another degree of freedom for manipulation of the graphene band structure.

2.1 Bilayer Hamiltonian

Consider a graphene bilayer with layer two rotated by θ relative to layer one. In general, we write the Hamiltonian:

$$H_{BG}(\mathbf{k}) = \begin{pmatrix} H^0 & H_{\perp} \\ * & H^{\theta} \end{pmatrix}, \quad (2.1)$$

where the diagonal blocks are the Hamiltonians of layer one and layer two respectively, and H_{\perp} describes the coupling between the layers. The Hamiltonian of layer one is simply the single layer graphene Hamiltonian of Equation 1.6. The Hamiltonian of layer two is the same but rotated by θ :

$$H^{\theta} = e^{-i\theta\sigma_z\tau_z/2} H^0 e^{i\theta\sigma_z\tau_z/2}. \quad (2.2)$$

Here and in what follows, the sublattice degree of freedom will be represented by the Pauli matrices σ , the valley degree of freedom by the Pauli matrices τ , and the layer degree of freedom by the Pauli matrices l .

It is sometimes advantageous for the diagonal blocks of H_{BG} to be identical. We may

accomplish this with the unitary rotation:

$$\bar{H} = e^{i(\theta l_z/2 + 2\pi l_0/3)\sigma_z\tau_z/2} H e^{-i(\theta l_z/2 + 2\pi l_0/3)\sigma_z\tau_z/2}, \quad (2.3)$$

where we are also gauging away the factor of $\exp(i2\pi/3)$ in H^0 . Thus, we have the rotated Hamiltonian:

$$\bar{H} = \begin{pmatrix} H^{\theta/2} & \bar{H}_\perp \\ * & H^{\theta/2} \end{pmatrix}, \quad (2.4)$$

where

$$H^{\theta/2} = e^{i(\theta/2 + 2\pi/3)\sigma_z\tau_z/2} H^0 e^{-i(\theta/2 + 2\pi/3)\sigma_z\tau_z/2} \quad (2.5a)$$

$$\bar{H}_\perp = e^{i(\theta/2 + 2\pi/3)\sigma_z\tau_z/2} H_\perp e^{-i(-\theta/2 + 2\pi/3)\sigma_z\tau_z/2}. \quad (2.5b)$$

We have completely defined the diagonal blocks $H^{\theta/2}$. We now turn to the question of the form of the interlayer coupling, \bar{H}_\perp . Commensuration plays a critical role in the interlayer coupling, as we see below.

2.2 Commensuration

In general, we consider two layers of graphene where layer two is rotated with respect to layer one by θ . Depending on θ , this system may or may not have translational symmetry. Systems that do have translational symmetry are called commensurate. Figure 2.1 plots commensurate systems by θ and the number of atoms in the commensurate supercell. There are only a few solutions with small numbers of atoms.

Figures 2.2 and 2.3 show the four smallest commensurations. In these figures, every

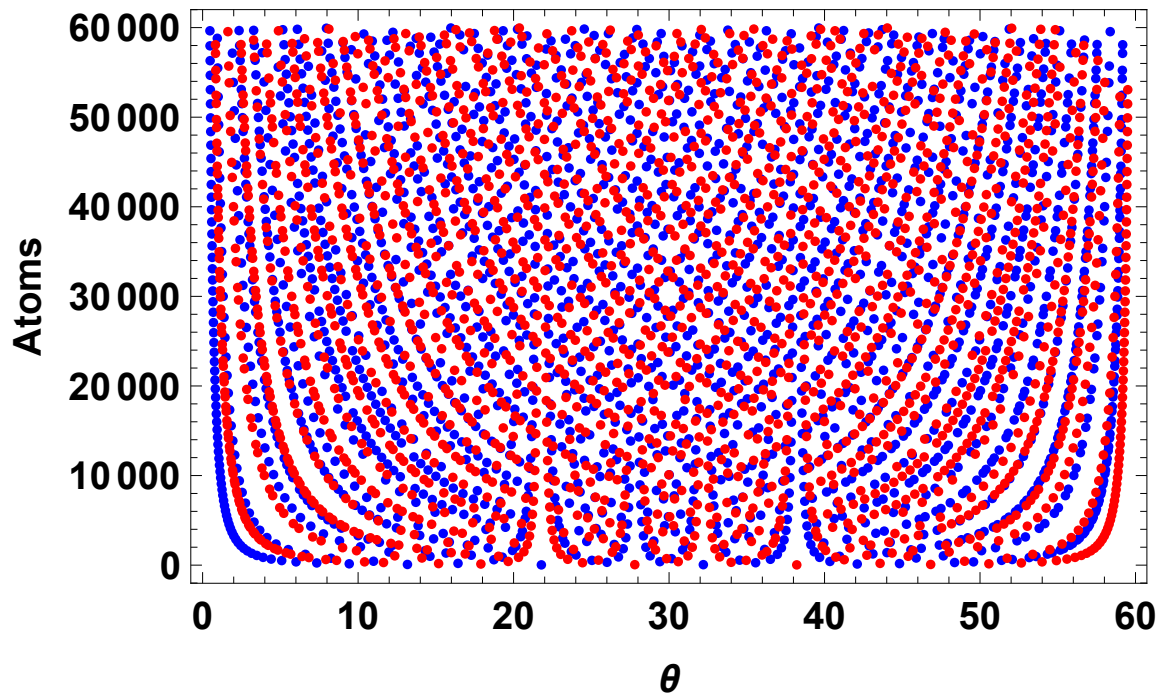


Figure 2.1: Number of atoms in a commensurate bilayer of given angle. Even commensurations are red, odd commensurations are blue.

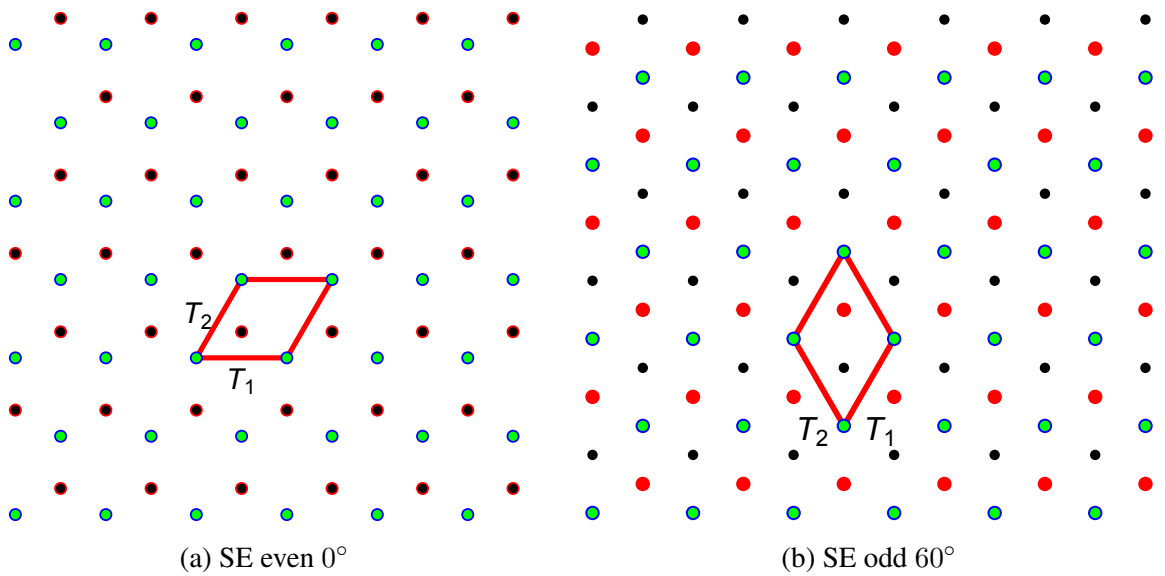


Figure 2.2: 4 Atom Commensurations

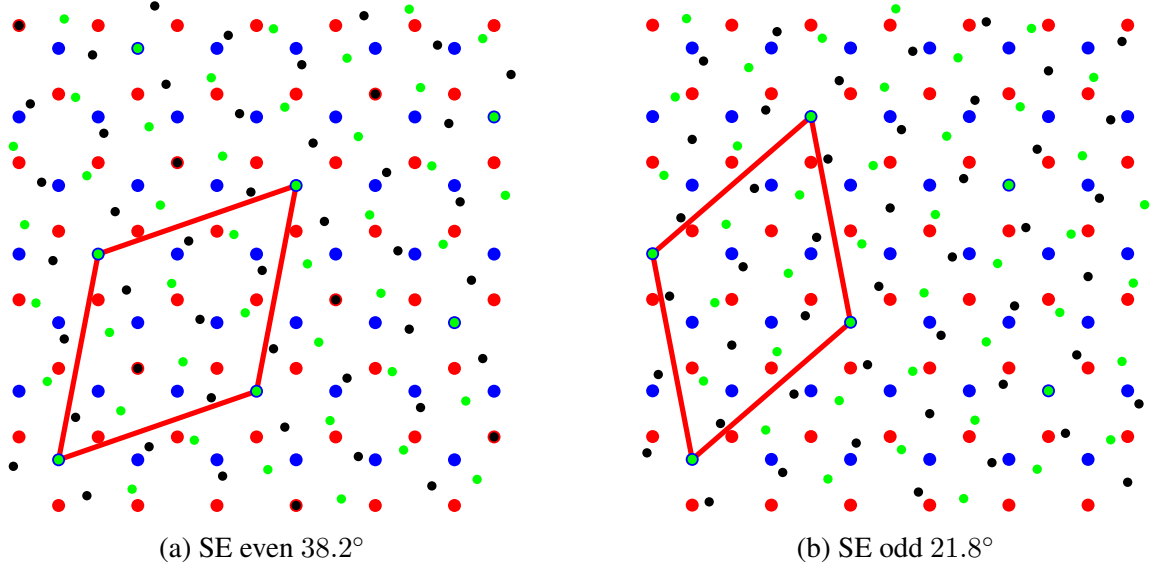


Figure 2.3: 28 Atom Commensurations

atomic sublattice/layer combination is a different color. The red lines indicate a unit supercell, the smallest pattern that repeats throughout the structure. These structures have only 4 and 28 atoms respectively.

The fact that they come in pairs of equal size is not a coincidence, but a general property of commensurations called sublattice exchange (SE) symmetry [22, 23]. Sublattice symmetry divides all commensurations into one of two groups: SE even or SE odd. In addition, every SE even commensuration at θ has an SE odd partner with the same number of atoms at $60^\circ - \theta$. The commensurations in Figures 2.2 and 2.3 show these partners.

We may define sublattice symmetry by the relations between the Dirac points. Let \mathbf{K}_{lv} be the unique Dirac point v of layer l . Every even commensuration satisfies $\mathbf{K}_{lv} = \mathbf{K}_{\bar{l}v}$, while every odd commensurations satisfies $\mathbf{K}_{lv} = \mathbf{K}_{\bar{l}\bar{v}}$. In this notation, \bar{l} means the opposite layer from layer l , and \bar{v} means the opposite valley from valley v . The equal signs are understood to be modulo a reciprocal superlattice vector. In other words, the two points are equivalent in the momentum space of the superlattice. The geometry of each case is shown in Figure 2.4, where the red arrows are reciprocal superlattice vectors.

Sublattice symmetry is interesting because it has a significant effect on the low energy

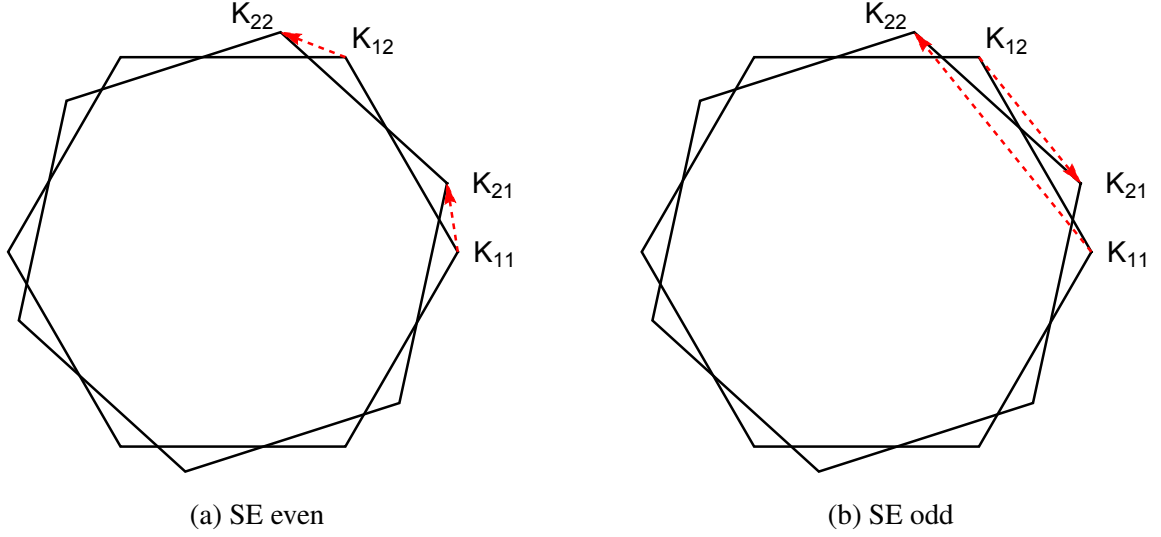


Figure 2.4: Dirac point connection for even and odd commensurations

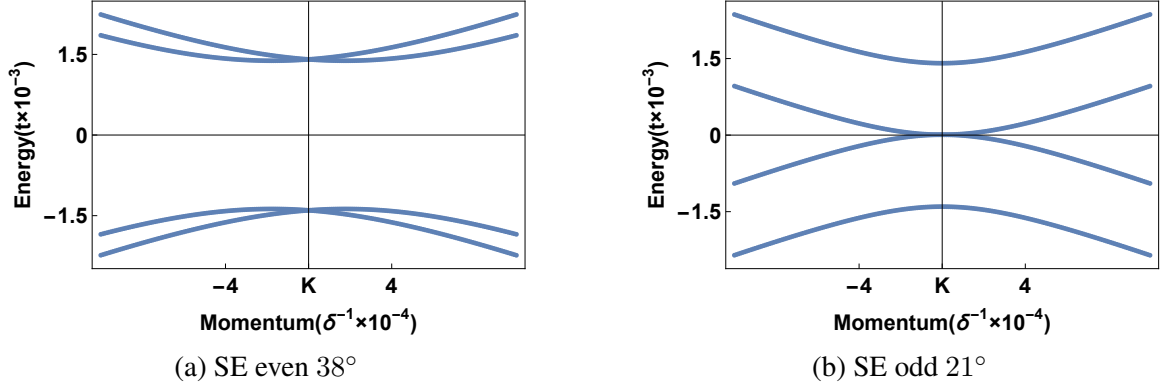


Figure 2.5: 28 Atom Commensurations

bands of any commensuration. We call this a commensuration effect because it depends on the structure being exactly at commensuration. In general, an SE odd commensuration effect can not open a gap by itself, while an SE even commensuration opens a gap (except at 0°). Figure 2.5 shows the bands for the 28 atom commensurations, created using simple tight binding models. Every commensuration (except 0°) has a low energy band structure identical to either the SE even or SE odd 28 atom band structure. The only difference is the scale of the low energy structure shrinks for larger commensurations. We will derive the source of this commensuration effect below.

2.3 Continuum Model

Commensurate angles are a very small subset of all possible rotation angles. Tight binding models require periodicity, so they only work for commensurate angles. To understand the vast majority of angles requires a theory without commensuration. The continuum model, first developed in [24], does not require commensuration. This model yields an effective Hamiltonian reproducing the low energy bands of the bilayer.

The unperturbed states are the single layer graphene states in each of the two layers near the Dirac points. The interlayer coupling matrix H_{\perp} then weakly couples these states. If the coupling is weak enough, we may apply perturbation theory to find the new eigenvalues and eigenvectors.

First, we must derive the coupling between the layers. The full Hamiltonian is:

$$H = H_{(1)} + H_{(2)} + H_{\perp} \quad (2.6a)$$

$$H_l = t \sum_{\sigma i} \sum_{j=\langle i \rangle} a_{l\sigma i}^{\dagger} a_{l\bar{\sigma} j} \quad (2.6b)$$

$$H_{\perp} = \sum_{\substack{l\sigma i \\ \sigma' j}} a_{l\sigma i}^{\dagger} a_{l\sigma' j} f(\mathbf{R}_{l\sigma i} - \mathbf{R}_{l\sigma' j}), \quad (2.6c)$$

where l is the layer index, σ is the sublattice index, $\bar{\sigma}$ indicates the opposite sublattice from σ , and $\langle i \rangle$ indicates unit cells linked by nearest neighbor hopping to the i th unit cell. The vector $\mathbf{R}_{l\sigma i}$ is the vector to the atom of sublattice σ in unit cell i of layer l . The function f is the real space form of the interlayer coupling .

The single layer terms are diagonal in momentum, as for single layer graphene. How-

ever, the interlayer term is more complicated. In momentum space, we find:

$$H_{\perp} = \sum_{\kappa l \sigma \sigma'} \sum_{\mathbf{G}_l \mathbf{G}_{\bar{l}}} a_{l\sigma\kappa}^{\dagger} a_{\bar{l}\sigma'\kappa+\mathbf{G}_l-\mathbf{G}_{\bar{l}}} \tilde{f}(\boldsymbol{\kappa} + \mathbf{G}_l) e^{i\mathbf{G}_l \boldsymbol{\delta}_{l\sigma B}} e^{-i\mathbf{G}_{\bar{l}} \boldsymbol{\delta}_{\bar{l}\sigma' B}}, \quad (2.7)$$

where \mathbf{G}_l is any reciprocal lattice vector of layer l . Note, we have also adopted the special notation $\boldsymbol{\delta}_{l\sigma B} = \boldsymbol{\delta}_l \boldsymbol{\delta}_{\sigma B}$. The first $\boldsymbol{\delta}_l$ is the nearest neighbor vector. The second δ is the Kronecker delta.

The quantity $\tilde{f}(\boldsymbol{\kappa} + \mathbf{G}_l)$ is the Fourier transform of the interlayer coupling function, which we define as:

$$\tilde{f}(\boldsymbol{\kappa}) = \frac{1}{A_0} \int_{-\infty}^{\infty} \int_{-\infty}^{\infty} f(\mathbf{r}) e^{i\boldsymbol{\kappa} \cdot \mathbf{r}} d^2 r, \quad (2.8)$$

where A_0 is the area of the unit cell of graphene. In the case of a radially symmetric interlayer coupling function, this reduces to the Hankel transform:

$$\tilde{\gamma}(\kappa) = \frac{2\pi}{A_0} \int_0^{\infty} x f(x) J_0(\kappa x) dx, \quad (2.9)$$

where $J_0(r)$ is the Bessel function.

The formula for H_{\perp} in Equation 2.7 is the central equation to understanding bilayer graphene. It says that the state in layer l at momentum $\boldsymbol{\kappa}$ couples to all states in layer \bar{l} at momentum $\boldsymbol{\kappa}$ plus any sum of reciprocal vectors of both layers, $\mathbf{G}_l - \mathbf{G}_{\bar{l}}$. This is entirely expected as the set of all such sums is identical to the set of reciprocal superlattice vectors. In other words, H_{\perp} couples any states differing by a reciprocal superlattice vector. The key point is that the energy scale of the coupling, $\tilde{f}(\boldsymbol{\kappa} + \mathbf{G}_l)$, involves the reciprocal vector of layer l , and not simply the reciprocal superlattice vector.

2.3.1 Perturbation Theory

Now we perform degenerate perturbation theory to find the low energy corrected bands. Since we are interested only in the low energy theory, we use $|\psi_{lgv}\rangle$ to mean a single layer

state of layer l and valley v with momentum \mathbf{K}_{lv} , that is, at the specified Dirac point . The index g specifies the positive or negative energy state of the particular Dirac cone. Therefore, we have an eight dimensional degenerate perturbation theory because there are eight states in the degenerate subspace. We define $H_{\perp}^{(n)}(\theta)$ to be the order n perturbative correction to the uncoupled Hamiltonian . The first order correction is:

$$H_{\perp}^{(1)}(\theta) = \langle \psi_{lgv} | H_{\perp} | \psi_{l'g'v'} \rangle . \quad (2.10)$$

We understand that each set of indices gives one element of the eight by eight matrix $H_{\perp}^{(1)}(\theta)$. The second order correction is:

$$H_{\perp}^{(2)}(\theta) = \sum_{\kappa l'' g''} \frac{\langle \psi_{lgv} | H_{\perp} | \psi_{l''g''}(\boldsymbol{\kappa}) \rangle \langle \psi_{l''g''}(\boldsymbol{\kappa}) | H_{\perp} | \psi_{l'g'v'} \rangle}{E_{l''g''}(\boldsymbol{\kappa})}, \quad (2.11)$$

where $|\psi_{lg}(\boldsymbol{\kappa})\rangle$ is the single layer graphene state of layer l'' with energy sign specified by g'' at $\boldsymbol{\kappa}$. Note, this state does not include the subscript v'' because it may not be near any particular valley. In general, the perturbation theory above results in three types of terms, which we describe now.

The first type of term is called direct coupling. This term describes the coupling of the degenerate subspace to itself. According to Equation 2.10, it can only be non-zero if the two Dirac points considered are coupled by H_{\perp} . Equation 2.7 demonstrates that H_{\perp} only couples states that differ by reciprocal superlattice vectors. We explained in Section 2.2 that this occurs if and only if the superlattice is commensurate [22]. Thus, we call this the commensuration term. Note, this term must be layer off-diagonal. In addition, while this term may be valley diagonal (SE even) or valley off-diagonal (SE odd), it cannot be both [22]. Therefore, the commensuration term is at most a two by two matrix. Since this term couples degenerate states, its effect will be large, and it is the origin of the gap mentioned previously.

The second type of term is called perturbative indirect coupling. These terms describe

the coupling of the degenerate subspace to higher energy states and then back. Thus, they appear as second order terms in the perturbative sum. Once again, the matrix elements can only be non-zero for states that differ by reciprocal superlattice vectors. Note, this term is layer-diagonal.

The third type of term is called non-perturbative indirect coupling. These are also second order in the perturbative theory. However, they describe coupling to a state outside the degenerate subspace that is too close in energy to be accurately described by perturbation theory. If such a term exists in the sum, perturbation theory is no longer accurate for the system, and we say the system is in the non-perturbative regime.

Even though only one term is called the commensuration term, we may associate every term in the perturbative sum with a possible commensuration of the system. All second order terms describe a link from a Dirac point to a point differing by a reciprocal superlattice vector. There exists a commensuration angle for which this coupling is direct, and we may associate this term with that commensurate angle. This association is useful because (as we will see below) the strength of the term depends on its associated commensuration angle, even if the system is not at that commensuration.

We now describe each term in more depth.

2.3.2 Direct Coupling

Recall direct coupling only occurs if there are reciprocal vectors that connect Dirac points of layer one to Dirac points of layer two. Solutions exist for any commensuration: for even commensurations, \mathbf{K}_{lv} connects to $\mathbf{K}_{\bar{l}v}$, while for odd \mathbf{K}_{lv} connects to $\mathbf{K}_{\bar{l}\bar{v}}$.

Thus, the term, $H_{\perp}^{(1)}(\theta)$ is composed of blocks of two by two matrices. These blocks either connect like valleys of each layer or opposite valleys depending on the even or odd nature of the commensuration. We add the valley labels to specify the blocks, $H_{\perp, vv'}^{(1)}(\theta)$.

According to Equation 2.7, the calculation of interlayer coupling requires solutions to the equation $\mathbf{K}_{1v} + \mathbf{G}_1 = \mathbf{K}_{2v'} + \mathbf{G}_2$, where \mathbf{G}_l is a reciprocal lattice vector of layer l .

Suppose we are at a commensuration angle c . Let \mathcal{G}_c be the set of all such solutions:

$$\mathcal{G}_c = \{(\mathbf{G}_1, \mathbf{G}_2) | \mathbf{K}_{1v} + \mathbf{G}_1 = \mathbf{K}_{2v'} + \mathbf{G}_2\}. \quad (2.12)$$

Now we define a function, N_c , that maps members of \mathcal{G}_c to the appropriate norm for measuring coupling strength:

$$N_c(\mathbf{G}_1, \mathbf{G}_2) = \|\mathbf{K}_{1v} + \mathbf{G}_1\|. \quad (2.13)$$

We next define the set of all norms of \mathcal{G}_c , and we order the results:

$$\mathcal{N}_c = \{N_c(g) | g \in \mathcal{G}_c\} = \{n_c^1, n_c^2, n_c^3, \dots\}. \quad (2.14)$$

We partition \mathcal{G}_c into subsets, $\mathcal{G}_c = \cup_i \mathcal{G}_c^i$, such that all members of a subset have the same value under the function N_c :

$$\mathcal{G}_c^i = \{(\mathbf{G}_1, \mathbf{G}_2) | (\mathbf{G}_1, \mathbf{G}_2) \in \mathcal{G}_c, N_c(\mathbf{G}_1, \mathbf{G}_2) = n_c^i\}. \quad (2.15)$$

We make the further definition that the norm of the subset is $|\mathcal{G}_c^i| = n_c^i$. Assuming the interlayer coupling obeys C_3 symmetry, all members of \mathcal{G}_c^i share the same associated coupling strength:

$$\tilde{\gamma}_c^i = \tilde{f}(\mathbf{K}_{1v} + \mathbf{G}_1) \quad \text{s.t.} \quad \mathbf{G}_1 \in \mathcal{G}_c^i. \quad (2.16)$$

In practice, we only care about the solutions in the set \mathcal{G}_c^1 and their associated coupling strength $\tilde{\gamma}_c^1$. This is because the Fourier transform of the interlayer coupling is exponentially decreasing with the length of its argument. Therefore, for a particular commensuration angle, c , we associate one coupling strength, $\tilde{\gamma}_c = \tilde{\gamma}_c^1$ and ignore the others. In addition, \mathcal{G}^1 always has three members, so we label the important solutions \mathbf{G}_l^i , where l denotes the layer

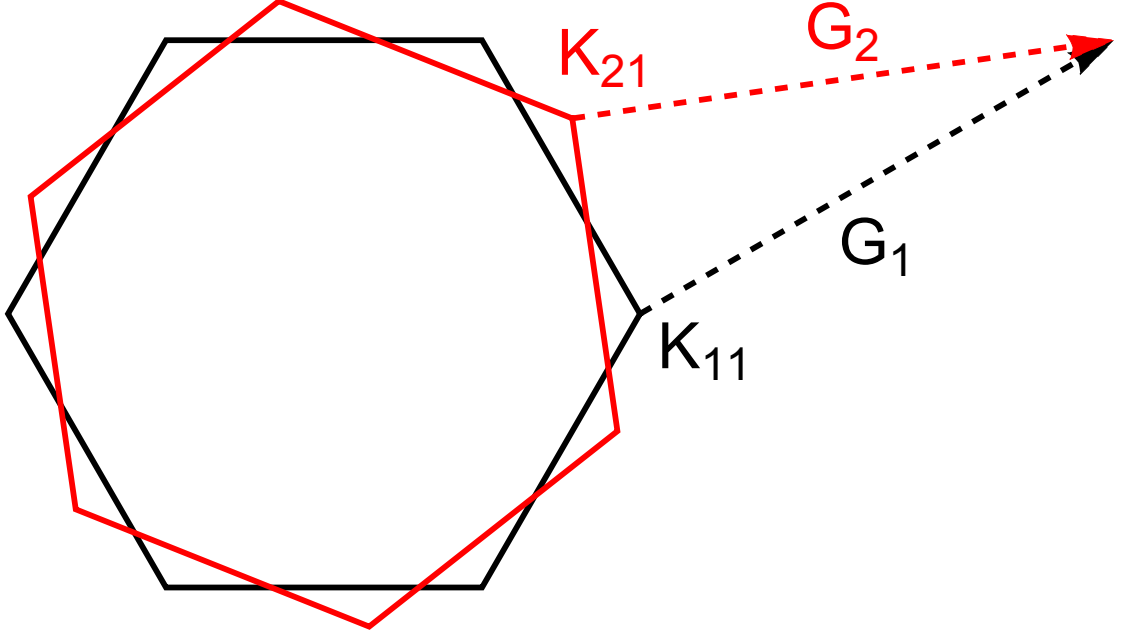


Figure 2.6: Even commensuration showing BZ of each layer and a solution to the coupling equation.

and i ranges from one to three for each possible solution. We have dropped the subscript c because we will only deal with one commensuration. In other words, once we choose a commensuration, we have an associated coupling strength and three reciprocal lattice vectors. In Figure 2.6, we show an even commensuration and one of the solutions. The two other solutions couple the other equivalent Dirac point pairs, and are the C_3 symmetric partners of the depicted solution.

Since only two valleys ever couple directly, we can separate $H_{\perp}^{(1)}$ into two by two blocks between valley v and v' . Therefore, we may write the interlayer coupling:

$$H_{\perp, vv'}^{(1)}(\theta) = \chi(\theta, v, v') \tilde{\gamma}_{\theta} \sum_{i=1}^3 \begin{pmatrix} 1 & e^{-i\nu \mathbf{G}_2^i \cdot \boldsymbol{\delta}_2} \\ e^{i\nu \mathbf{G}_1^i \cdot \boldsymbol{\delta}_1} & e^{i\nu \mathbf{G}_1^i \cdot \boldsymbol{\delta}_1} e^{-i\nu \mathbf{G}_2^i \cdot \boldsymbol{\delta}_2} \end{pmatrix}, \quad (2.17)$$

where $\nu = \pm 1$ for $v = 1, 2$, and $\chi(\theta, v, v')$ is an indicator function:

$$\chi(\theta, v, v') = \begin{cases} \delta_{vv'} & \theta \text{ is SE even} \\ \delta_{\bar{v}v'} & \theta \text{ is SE odd} \\ 0 & \text{otherwise} \end{cases} . \quad (2.18)$$

We may perform the sum to find the simplified form:

$$H_{\perp, vv'}^{(1)}(\theta) = \chi(\theta, v, v') 3\tilde{\gamma}_{\theta} \begin{pmatrix} 1 & 0 \\ 0 & e^{i\nu 2\pi q(\theta)/3} \delta_{vv'} \end{pmatrix}, \quad (2.19)$$

where $q(\theta) \in \{-1, 0, 1\}$ and depends on the specific geometry of the commensuration

In addition, odd commensurations have only one non-zero element and even commensurations have two non-zero elements. The phase twist in the element that pairs the B sublattices is the origin of the gap that opens in the SE even case. Note that $\theta = 0$ is unique among even commensurations because there is no phase twist and the gap does not open.

We may write the interlayer coupling in terms of the Pauli matrices:

$$H_{\perp} = \mathcal{O}(\theta) \frac{3\tilde{\gamma}_{\theta}}{2} (\sigma_0 + \sigma_z) \tau_x l_x + \mathcal{E}(\theta) \frac{3\tilde{\gamma}_{\theta}}{4} \left[(\sigma_0 + 3\sigma_z) \tau_0 l_x + (-1)^q \sqrt{3} (\sigma_0 - \sigma_z) \tau_z l_y \right], \quad (2.20)$$

where $\mathcal{O}(\theta) = 1$ if θ is an odd commensuration and zero otherwise, and $\mathcal{E}(\theta) = 1$ if θ is an even commensuration and zero otherwise. Thus, we have the total Hamiltonian:

$$\bar{H} = H^{\theta/2} l_0 + \bar{H}_{\perp}, \quad (2.21)$$

where \bar{H}_{\perp} is calculated from Equation 2.5b.

These matrices reproduce the earlier results concerning commensuration. In particular,

an even commensuration is gapped (except at zero degrees), while an odd commensuration is ungapped.

2.3.3 Indirect Coupling

Recall indirect coupling describes coupling from the degenerate subspace to non-zero energy states outside the degenerate subspace and then back. Figure 2.7 shows the momentum space picture for a system at arbitrary angle θ . At \mathbf{K}_{11} , there are zero energy states from layer one. At \mathbf{K}_{21} , there are zero energy states from layer two. If the system were at 0° then there would exist the set \mathcal{G}_0 of reciprocal superlattice vectors connecting \mathbf{K}_{11} and \mathbf{K}_{21} . At the current angle θ , these vectors couple states at \mathbf{K}_{11} instead to states of layer two at some higher energy.

In general, we take only the strongest couplings, that is the coupling corresponding to the set \mathcal{G}_0^1 . Thus, in Figure 2.7, we only consider the three states at the end of the dashed red arrows. In addition, we assume θ is close enough to commensuration that we may use the linear approximation around \mathbf{K}_{21} . Thus, the energy of these three states is $v\delta K$, where δK is their distance from \mathbf{K}_{21} . The scale of the coupling as dictated by perturbation theory is then, $\tilde{\gamma}_0/v\delta K$.

Figure 2.7 only describes the indirect coupling associated to the zero degree commensuration. However, terms exist for every commensuration not exactly realized by the system. In Figure 2.8, we see two Dirac points and one solution, \mathbf{G}_l , for the 38.2° commensuration. The zero energy states at \mathbf{K}_{11} will couple to the high energy states of layer two at the end of the dashed red arrows. Assuming we are close enough to commensuration to use the linear approximation of the Dirac cone, their energy is $v\delta K_c$. The scale of this coupling as dictated by perturbation theory is then $\tilde{\gamma}_{38}/v\delta K_c$.

For the general case, the energy scale is $\tilde{\gamma}_c/v\delta K_c$. We use δK_c to emphasize that this describes the closest approach of the two Dirac points in all momentum space.

The result of these indirect perturbative couplings is four decoupled two by two Hamil-

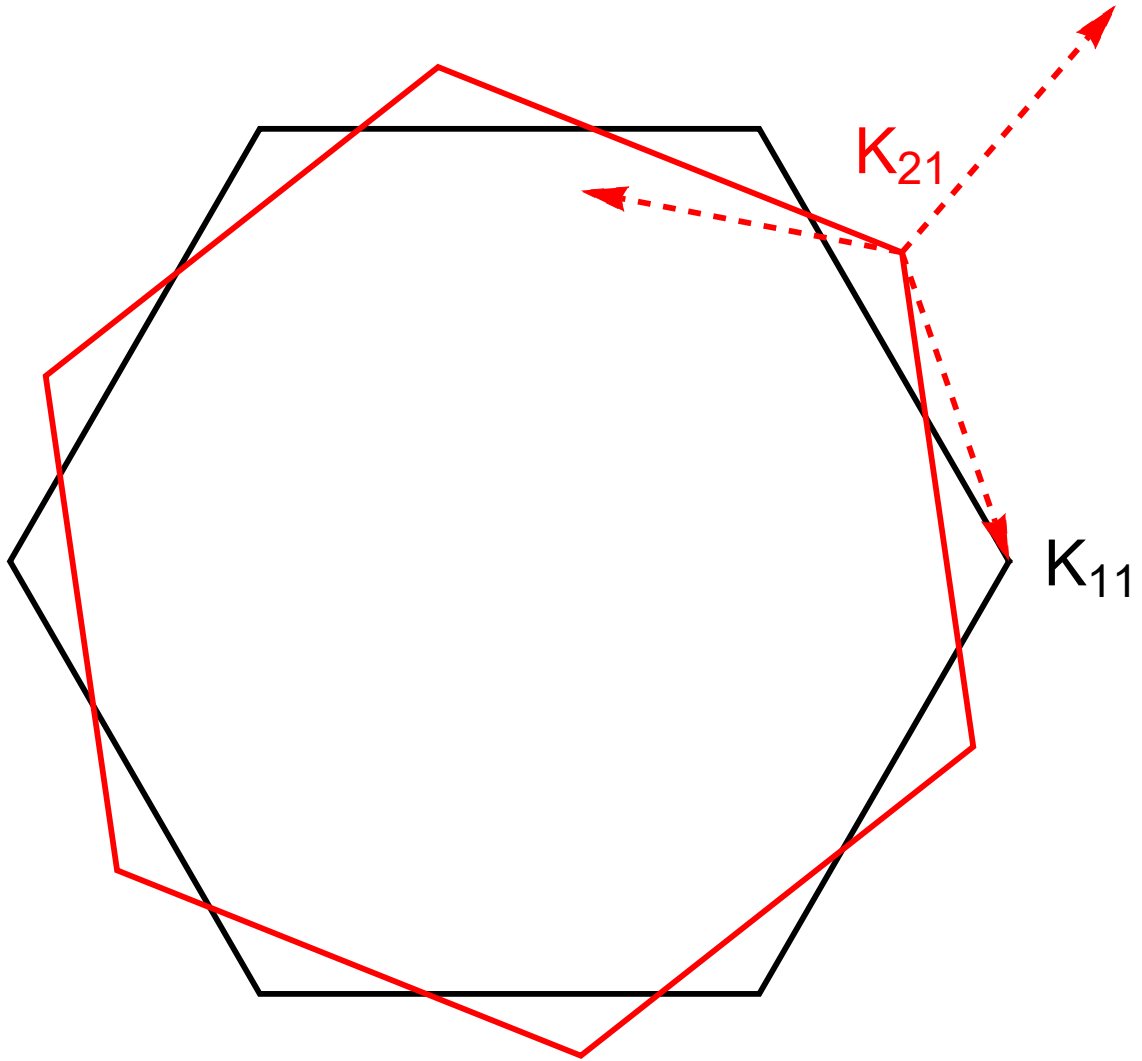


Figure 2.7: Indirect coupling through $\theta = 0^\circ$ commensuration term. The dashed arrows point from the Dirac point of layer two to the states of layer two that will couple to the Dirac point of layer one.

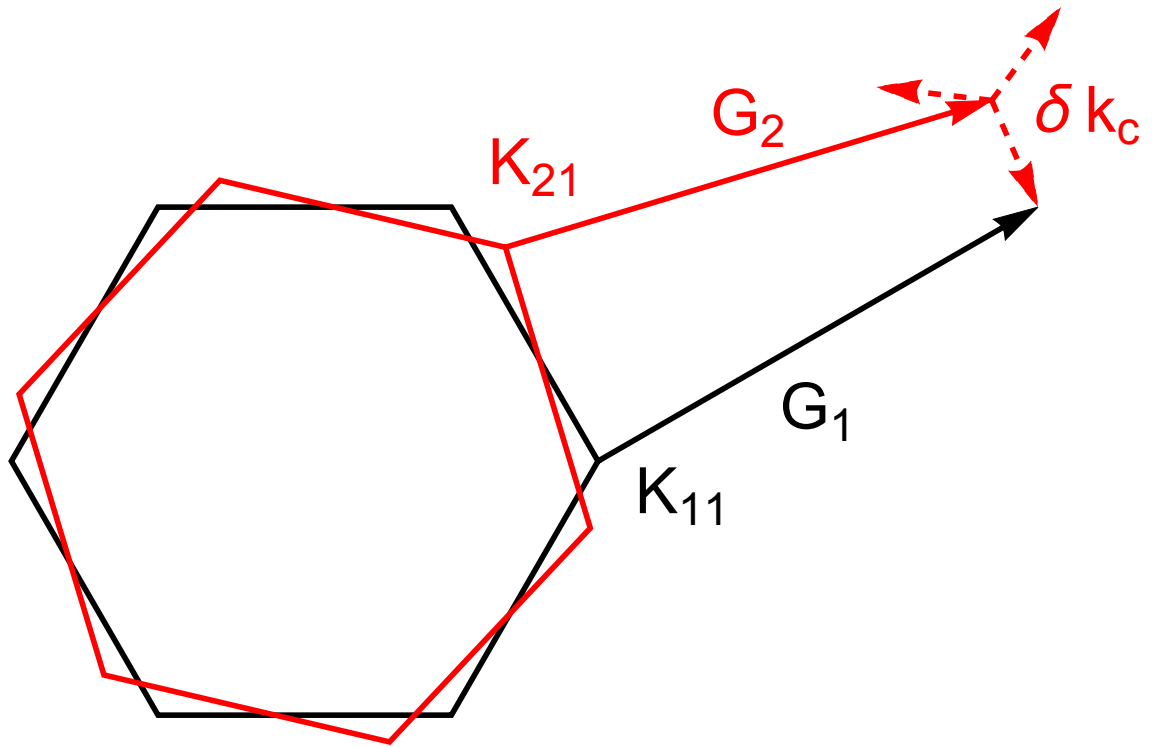


Figure 2.8: Indirect coupling through $\theta = 38.2^\circ$ commensuration term. The dashed arrows point from the Dirac point of layer two to the states of layer two that will couple to the Dirac point of layer one.

tonians, one for each layer valley combination. In the standard treatment of bilayer graphene, we choose an angle near zero. This allows us to discard all terms except those associated with the zero degree commensuration.

For each dashed arrow, we can derive a coupling matrix, and by adding them together we can perform perturbation theory. The unperturbed basis states are diagonal, and we choose the matrix representation:

$$H'^0 = -vk\sigma_3\tau_0l_0. \quad (2.22)$$

Recall that k is the momentum measured with respect to the Dirac point. To perform the calculation, we use the following approximation scheme:

$$\frac{\tilde{\gamma}_c}{v\delta K_c} \ll 1, k \ll \delta K_c, \theta \ll 1. \quad (2.23)$$

The first condition ensures we are in the perturbative regime. The second condition ensures we are close to the Dirac cones. The third condition ensures we can expand everything for small angle. We find that the second order indirect coupling correction, $H_{\perp}^{(2)}(\theta)$, is:

$$H_{\perp}^{(2)}(\theta) = \frac{\tilde{\gamma}_0^2}{t} \left(1 - \frac{3\sqrt{3}}{2\pi} \right) \sigma_0\tau_0l_0 + kv \frac{27\tilde{\gamma}_0^2}{4t^2\theta^2\pi^2} \sigma_3\tau_0l_0. \quad (2.24)$$

We can further simplify by using the expansion parameter, $\alpha = \tilde{\gamma}_c/v\delta K_c$. In this case, we use $c = 0^\circ$ because we are interested in the 0° commensuration. In general $\delta K_0 = 4\pi\theta L_0/3a^2$, where L_0 is the side length of the 0° commensuration unit cell. We find:

$$H_{\perp}^{(2)}(\theta) = \frac{\tilde{\gamma}_0^2}{t} \left(1 - \frac{3\sqrt{3}}{2\pi} \right) \sigma_0\tau_0l_0 + 9\alpha^2 vk\sigma_3\tau_0l_0. \quad (2.25)$$

There is a rigid shift and negative velocity renormalization. This effect was first derived in [24], but with an incorrect value for the shift.

While the near 0° case is the most studied regime, there is nothing in the theory that restricts us to these angles. We can perform a similar perturbative calculation near 38.2° . Instead of θ , we now use $\delta\theta$, the difference from commensuration, as our expansion parameter. To lowest order in $\delta\theta$, we find the correction:

$$H_{\perp}^{(2)} = \frac{27\tilde{\gamma}_{38}^2}{14\pi t\delta\theta}\sigma_0\tau_0l_0. \quad (2.26)$$

This is a rigid shift. If we go one order higher in $\delta\theta$, we can also see the velocity renormalization:

$$H_{\perp}^{(2)} = \frac{27\tilde{\gamma}_{38}^2}{14\pi t\delta\theta} + vk\left(\frac{27\tilde{\gamma}_{38}^2}{28\pi^2 t^2\delta\theta^2}\right)\sigma_3\tau_0l_0. \quad (2.27)$$

This can be further simplified and generalized to all angles by using $\alpha = \tilde{\gamma}_c/v\delta K_c$ and $\delta k_c = 4\pi\delta\theta L_c/3a^2$:

$$H_{\perp}^{(2)} = -q(\theta)\frac{27a^2\tilde{\gamma}_c^2}{2\pi tL_c^2\delta\theta}\sigma_0\tau_0l_0 + 9\alpha^2 vk\sigma_3\tau_0l_0. \quad (2.28)$$

Note the velocity renormalization is the same in all cases. However, the rigid shift is commensuration dependent. In particular, non-zero commensurations have a $1/\delta\theta$ term that is not present in the case of 0° .

2.3.4 Non-perturbative Coupling

We have seen that indirect coupling terms have an energy scale $\tilde{\gamma}_c/v\delta K_c$. As $\theta \rightarrow c$, we have $\delta K_c \rightarrow 0$. In other words, the perturbation parameter blows up, and perturbation theory is no longer valid. The range of angles for this non-perturbative regime depends on the numerator $\tilde{\gamma}_c$. This is expected to decrease exponentially and be irrelevant for all but the smallest commensurations, and in general we do not worry about such terms. However,



Figure 2.9: Schematic of twist angle. Each commensurate angle has a zone of influence where the effect is perturbative (blue) and non-perturbative (red).

near the smallest commensurations, non-perturbative angles are accessible.

We may estimate the non-perturbative range of angles using the formula $\delta\theta_c = \tilde{\gamma}_c/v|\mathcal{G}_c^1|$. For near zero degrees, we find an angle of about 1° . Indeed, the non-perturbative effects of this regime have been investigated. As $\theta \rightarrow 0$, there is a series of magic angles where the electron velocity vanishes. The first of these is predicted by the renormalization effect of perturbative theory, but the others are inaccessible to the perturbative theory and represent true non-perturbative physics [25]. Flat bands are interesting because they allow for electron interactions to dominate the physics of the system. In fact, such magic angle twisted bilayers have been constructed and unconventional superconductivity was observed [26, 27]. In addition, wavefunctions tend to localize to AA stacked regions [28, 29].

For near 38.2° , we find an angular range on the order of 0.01° . This angular range corresponds to system sizes of hundreds of nanometers. Thus, we need large systems to observe this effect. However, incorporation of interaction effects through renormalization theory is expected to scale the interlayer coupling term with system size [30]. The exact exponent of the scaling is uncertain, but it seems to be at least $1/2$. In this case, effects may become visible at system sizes down to tens of nanometers. We will explore this regime further in Chapter 3.

For larger commensurations, we may safely neglect the non-perturbative regime. In general, the exponential fall off of $\tilde{\gamma}_c$ ensures that system sizes become prohibitive.

2.4 Summary

We have fully developed the perturbative theory of bilayer graphene to second order. Figure 2.9 presents a schematic. We show two commensuration angles, θ_c and $\theta_{c'}$. For each angle, we have three regions that dictate how the given commensuration will affect a system at arbitrary angle θ .

If θ falls in the blue region, the commensuration has a perturbative effect. If θ falls in the red region, the commensuration has a non-perturbative effect. If θ is precisely at the commensuration, the effect is a direct coupling. The size of each of the first two regions is dictated by the appropriate Fourier component of the interlayer coupling.

Note, the schematic is inaccurate in the sense that there are many more than two commensuration angles. In fact, the commensuration angles are a dense subset of all angles. This means there are countably infinite such regions to consider for arbitrary angle. However, only the commensurations at 0° and 38.2° have large enough strength to appreciably affect the low energy electronic structure. Therefore, we restrict ourselves to these cases and safely ignore effects from all other commensurations.

CHAPTER 3

BILAYER GRAPHENE NEAR COMMENSURATION

In the previous chapter, we derived the complete theory of graphene bilayers at arbitrary twist angle. We derived perturbative corrections for systems near the smallest commensurations. In general, perturbation theory is a good tool for describing these angles and the problem is solved. However, this leaves the more difficult case of the non-perturbative regime. In this chapter, we examine the available tools to tackle this case and reveal new physics for systems near commensuration [31].

3.1 Available Tools

In the non-perturbative regime, we must adopt a different method to derive the low energy band structure. The simplest solution is to diagonalize full tight binding models for these systems. This has two disadvantages.

First, tight binding models require translational symmetry, while we want the band structure for arbitrary angle. This is not actually a problem. Given an arbitrary angle, we may choose a commensuration arbitrarily close to this angle for the tight binding model. The difference in band structure will only be the direct effect of the commensuration. However, in the non-perturbative regime the unit cells of these commensurations will be very large, and their effect will be exponentially small.

This solution creates the second problem. The size of the matrices becomes too large. The available computing power is insufficient for the system we want to study.

A different method is to tackle the problem in momentum space. Having derived the interlayer coupling in momentum space, we make the observation that the coupling states are arrayed in their own honeycomb lattice [25]. We can write a sparse matrix to describe the coupling induced between the two layers. This matrix has infinite dimension, but we

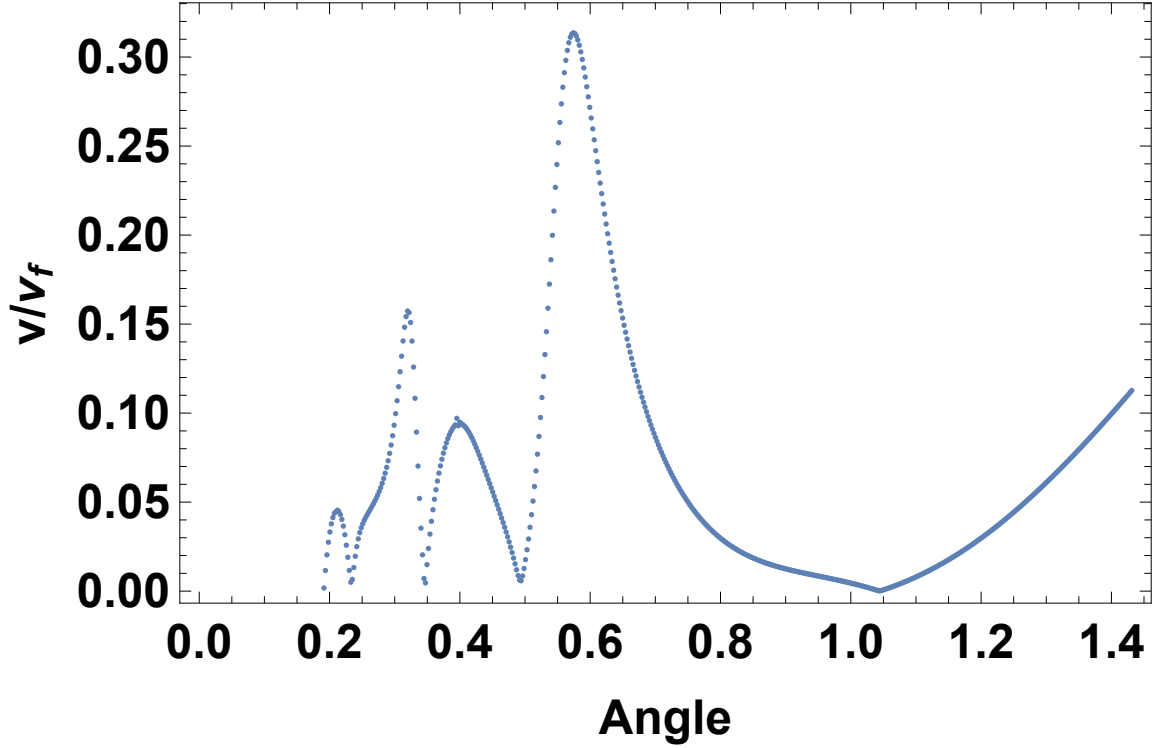


Figure 3.1: Renormalization of the Fermi velocity as $\theta \rightarrow 0$. We see a series of magic angles with zero velocity.

can truncate so that only states below a certain energy are included. In other words, we assume most of the bilayer states can be described by single layer states below a certain energy threshold. This is reasonable because higher energy states will have a larger energy denominator and less effect on the low energy electronic structure of the system.

In Figure 3.1, we use this method to reproduce the magic angles in the non-perturbative regime near 0° . As $\theta \rightarrow 0^\circ$, we see angles where the Fermi velocity is zero. This method is effective at saving some computational resources, but if we wish to extend this plot to lower angles, we must include more single layer states and will eventually have the same computational problem. In addition, it provides little insight into the physics of the system. We now turn to a different technique.

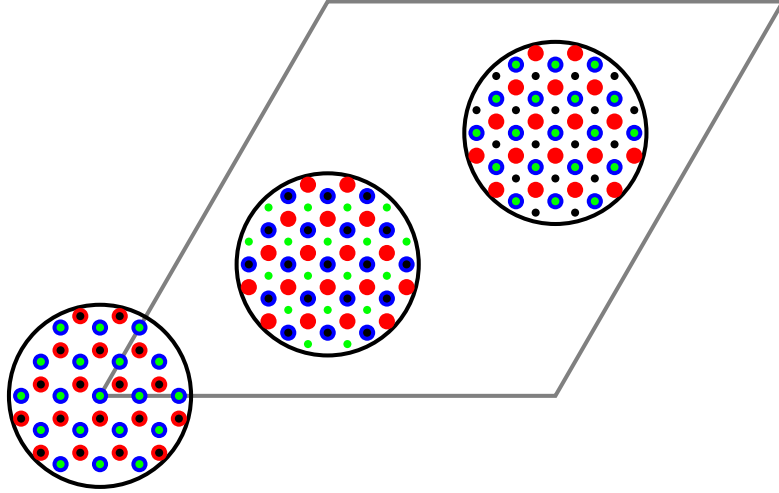


Figure 3.2: The gray lines are the supercell for a bilayer very near 0° . The circles show a magnified view of regions of AA, AB, and BA stacking.

3.2 Local Lattice Stacking

Consider a bilayer in the non-perturbative regime very near the 0° (or any other) commensuration. Although we must abandon perturbation theory, we can still achieve a local understanding of the electronic structure using the local stacking pattern in the supercell. For instance, at the origin, the lattice is locally nearly indistinguishable from a 0° commensurate lattice. In fact, at every point in the superlattice, the lattice is locally the 0° pattern plus an interlayer translation. Figure 3.2 shows a schematic. The gray lines are the supercell of a system very near 0° . The circles show a magnified view of the local lattice stacking in three special regions. In these regions, the stacking is locally AA, AB, and BA respectively.

In fact, if we choose any point in the supercell, the local stacking will be indistinguishable from AA stacking plus an interlayer translation that depends on the point we chose. In addition, there is nothing special about 0° . For a system very near a commensuration, θ_c , the local lattice stacking at any point in the supercell is nearly indistinguishable from the commensuration plus a position dependent translation.

Using Figure 3.3, we can derive the translation that gives us the local stacking. Let \mathbf{R}_i

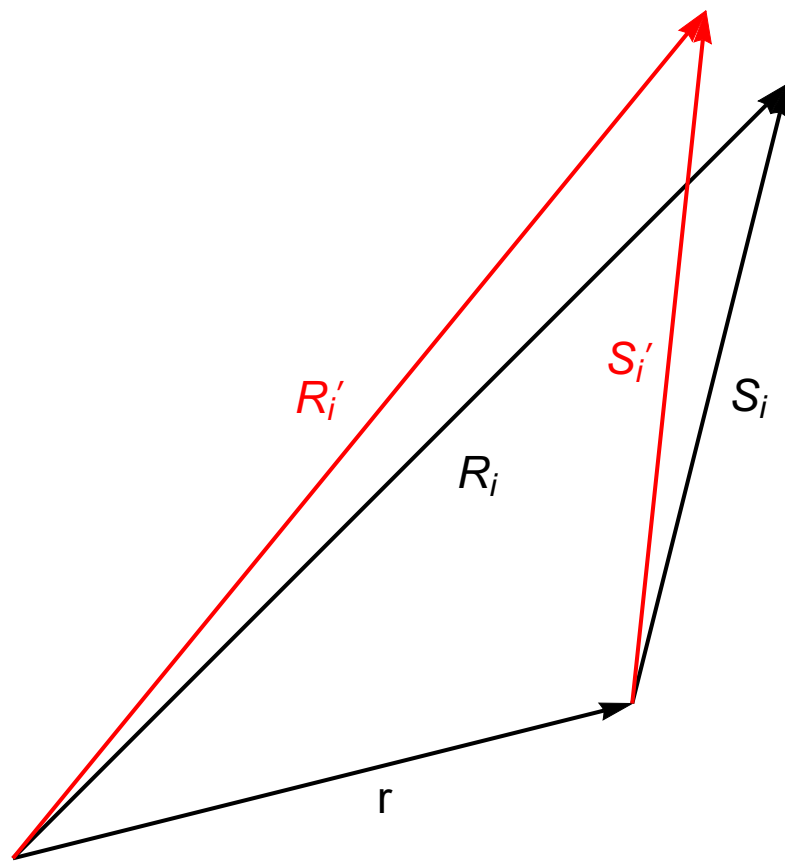


Figure 3.3: Decomposition of a rotation into a rotation plus a translation.

be the position of atom i in the commensuration with respect to the origin . Let \mathbf{R}'_i be the same atom but rotated with respect to the origin by some small angle $\delta\theta$. Let \mathbf{S}_i and \mathbf{S}'_i be the same positions, but measured with respect to the arbitrary point \mathbf{r} . The following relations hold:

$$\mathbf{S}_i = \mathbf{R}_i - \mathbf{r} \quad \mathbf{R}'_i = \text{rot}[\delta\theta]\mathbf{R}_i \quad \mathbf{S}'_i = \mathbf{R}'_i - \mathbf{r}. \quad (3.1)$$

Note \mathbf{S}'_i and \mathbf{S}_i are not related by a rotation. That is, the atomic sites are only related by a small rotation about the origin, not some other point. However, we seek a translation \mathbf{T} , such that if we shift the atomic sites by \mathbf{T} , these sites will be related by a rotation about the new origin to unrotated sites . That is, we seek \mathbf{T} that satisfies:

$$\mathbf{S}'_i = \text{rot}[\delta\theta](\mathbf{S}_i + \mathbf{T}) = \mathbf{R}'_i - \mathbf{r}. \quad (3.2)$$

Combining all the equations, we find:

$$\mathbf{T} = (1 - \text{rot}[-\delta\theta])\mathbf{r} = F\mathbf{r}, \quad (3.3)$$

where F is a matrix representation of \mathbf{T} that we will use in a later chapter .

Suppose we have a two layer system very near commensuration. Local to the origin, the system is very near commensuration, so that it appears almost indistinguishable from commensuration. Now select a new origin, \mathbf{r} . Local to \mathbf{r} , the system does not look like the commensuration but like the commensuration plus $\mathbf{T}(\mathbf{r})$. This proves that near an arbitrary \mathbf{r} , the lattice is locally the given commensuration plus the translation $\mathbf{T}(\mathbf{r})$. If we expand the translation to lowest order in $\delta\theta$, we find:

$$\mathbf{T} = 2r \sin\left(\frac{\delta\theta}{2}\right)\hat{\boldsymbol{\theta}} = r\delta\theta\hat{\boldsymbol{\theta}} + \mathcal{O}(\delta\theta^2)\hat{\boldsymbol{\theta}}, \quad (3.4)$$

where $\hat{\boldsymbol{\theta}}$ is the unit vector at \mathbf{r} pointing in the direction of increasing θ .

This confirms our intuition. The local lattice stacking in any region is just that of the origin plus the translation resulting from the twist by $\delta\theta$. This formula may be applied about any origin. The local lattice stacking may be corrected to an exact commensuration to good approximation by untwisting the lattice.

Knowing this translation, we can derive the local low energy Hamiltonian for any location in the superlattice. These Hamiltonians describe the semi-classical states that exist in a near commensurate superlattice. As the superlattice becomes large, this semi-classical approximation becomes good. At a few special points throughout the supercell, we will have the exact SE even and SE odd structures, while everywhere else will be an interpolation between them. This suggests we derive a general four by four Hamiltonian describing the superlattice throughout real space.

3.2.1 Real Space Hamiltonian

Let $H(\mathbf{r})$ be the effective low energy Hamiltonian of a bilayer near commensuration θ at \mathbf{r} in the superlattice. We can repeat the analysis of Equation 2.1. The diagonal blocks will be the same, but we expect the interlayer coupling to be a function of \mathbf{r} . We write the general Hamiltonian:

$$H(\mathbf{r}) = \begin{pmatrix} H^0 & H_{\perp}(\mathbf{r}) \\ * & H^{\theta} \end{pmatrix}. \quad (3.5)$$

To find $H_{\perp}(\mathbf{r})$, we return to Equations 2.7 and 2.17. Now, we add the translation $\mathbf{T}(\mathbf{r})$ to all sites in the second layer. This results in an additional factor multiplying each term of the sum:

$$H_{\perp, vv'}^{(1)} = \tilde{\gamma}_{\theta} \chi(\theta, v, v') \sum_{i=1}^3 e^{-i\nu \mathbf{G}_2^i \mathbf{T}(\mathbf{r})} \begin{pmatrix} 1 & e^{-i\nu \mathbf{G}_2^i \delta_2} \\ e^{i\nu \mathbf{G}_1^i \delta_1} & e^{i\nu \mathbf{G}_1^i \delta_1} e^{-i\nu \mathbf{G}_2^i \delta_2} \end{pmatrix}, \quad (3.6)$$

where again $\chi(\theta, v, v')$ is an indicator function that links like valleys for even commensuration.

surations and unlike valleys for odd commensurations. Note the addition of the translation breaks the symmetries that produced zero off-diagonal elements. We expect the translation to interpolate between the even and odd cases.

In general, we apply the same gauge transformation as in Equation 2.5b, so that the diagonal blocks are identical and the difference is absorbed into \bar{H}_\perp . We would like to write \bar{H}_\perp in terms of the Pauli matrices. Without loss of generality, we may focus solely on even commensurations. In other words, we will only consider commensurate angles that correspond to SE even systems. A system at or near an SE odd angle is also captured by this theory because all odd commensurations are even commensurations plus a translation. A theory that only includes even commensurations will be complete. Thus, we will now drop the valley degree of freedom, τ .

The full Hamiltonian is:

$$\bar{H} = H^{\theta/2} l_0 + \mathcal{A}_{i,j} \sigma_i l_j, \quad (3.7)$$

where $\mathcal{A}_{i,j}$ are all real numbers. The summation over repeated indices is implied. For generality, we allow the indices i, j to run over $x, y, z, 0$. However, the interlayer coupling can only involve terms with l_x and l_y . Later, we will add an interlayer electric field, which will correspond to an l_z term. However, here we may make the definition:

$$\mathbf{A}_i = (\mathcal{A}_{i,x}, \mathcal{A}_{i,y}). \quad (3.8)$$

In other words, we define \mathbf{A}_i as the vector with components $\mathcal{A}_{i,x}$ and $\mathcal{A}_{i,y}$. In addition, we will also define A_i to be the vector \mathbf{A}_i in the complex plane.

In addition, under these assumptions, the Hamiltonian \bar{H} has the following symmetry:

$$Pl_z \bar{H} Pl_z = -\bar{H}, \quad (3.9)$$

where P is inversion in momentum space. Since $\bar{H}(\mathbf{r})$ is the local Hamiltonian at \mathbf{r} , we

understand this symmetry to be local to r . Due to this symmetry, the local bandstructure will have particle hole symmetry after inversion of momentum. This symmetry has an important consequence. The bandstructure has no state at zero energy iff it is gapped. We now prove this statement.

First, we prove that if the bandstructure is gapped, the gap must include zero energy. If there is a gap, then there is an energy interval, (E_1, E_2) in which there are not states at any momentum. The symmetry guarantees if the interval is (E_1, E_2) at \mathbf{k} , it must be $(-E_2, -E_1)$ at $-\mathbf{k}$. However, the interval must be the same at all \mathbf{k} if the system is truly gapped. Therefore, $E_1 = -E_2$. If the gap has non-zero width, it must include zero energy. Thus, any gapped bandstructure has no zero energy state.

Second, we prove that the absence of zero energy state implies a gap. If there is no state at zero energy, there must be an interval around zero energy with no state. This is because we can exclude all cases where the bands approach zero energy but never touch it. The bands are continuous, so this could only happen in the limit of large k . However, we know in the limit of large k , the bands approach $\pm vk$, as in uncoupled graphene. Therefore, there is an interval around zero energy with no states.

Before beginning an analysis of these gauge fields, it is useful to have an intuition for how they distort the band structure. With all gauge fields set to zero, we have two coincident Dirac cones. The field \mathbf{A}_0 shifts these Dirac cones in opposite directions in energy. The fields \mathbf{A}_x and \mathbf{A}_y split the Dirac cones in momentum space. Finally, the field \mathbf{A}_z creates mass at the Dirac cones, opening gaps. These observations can all be verified by numerical experimentation.

We now try to quantify the behavior of the bands. In particular, we are interested in when the bands have degeneracy and when they have states at zero energy.

3.2.2 Gauge Field Analysis

In analyzing the gauge fields, we are interested in two criteria. First, we want to know when the Hamiltonian is not gapped. We proved above that this is equivalent to the condition that there is a state at zero energy. This will allow us to build a semi-classical picture of zero energy states throughout the supercell. Second, we want to know when the two Dirac equations implicit in the Hamiltonian have a degeneracy.

First, we set $\mathbf{A}_0 = 0$. There will exist a zero eigenvalue iff the determinant of the Hamiltonian is zero for some real value of momentum, that is:

$$\text{Det}[H(\mathbf{k})] = 0 \quad \text{for} \quad \mathbf{k} \in \mathbb{R}^2. \quad (3.10)$$

We write \mathbf{k} in polar coordinates (k, ϕ) and calculate the determinant. We introduce a, b, c to stand in for the coefficients of the polynomial. We find the determinant is:

$$\begin{aligned} \text{Det}[H(\mathbf{k})] &= av^4k^4 + 2bv^2k^2 + c = \\ &v^4k^4 + 2 \left[||A_z^2|| + (||A_y||^2 - ||A_x||^2) \cos 2\phi - (A_x\bar{A}_y + \bar{A}_xA_y) \sin 2\phi \right] v^2k^2 \\ &\quad + ||A_x^2 + A_y^2 + A_z^2||^2, \quad (3.11) \end{aligned}$$

where the unbolded A_i denote the vector \mathbf{A}_i in the complex plane. Recall that the z-component of all gauge fields is zero, so all gauge fields lie in the complex plane. The roots of this equation are then written:

$$k = \pm \frac{1}{v} \sqrt{-b \pm \sqrt{b^2 - c}}. \quad (3.12)$$

Finding the conditions for $k \in \mathbb{R}$ is equivalent to finding when the following two con-

ditions are satisfied:

$$b < 0 \quad b^2 > c. \quad (3.13)$$

Since b must be negative, we know it must also satisfy:

$$b \leq -\sqrt{c} = -\|A_x^2 + A_y^2 + A_z^2\|. \quad (3.14)$$

The coefficient b is a simple sinusoidal function of ϕ . Therefore, the critical values are identical to the extremal values. We find the maximum and minimum occur for:

$$\phi = \frac{1}{2} \arctan \frac{(A_x \bar{A}_y + \bar{A}_x A_y)}{(\|A_x\|^2 - \|A_y\|^2)} + n \frac{\pi}{2} \quad n \in \text{integers}. \quad (3.15)$$

Using the critical values of ϕ , we find b is restricted to the interval:

$$\|A_z^2\| - \|A_x^2 + A_y^2\| \leq b \leq \|A_z^2\| + \|A_x^2 + A_y^2\|. \quad (3.16)$$

Combining Equations 3.14 and 3.16 and using the reverse triangle inequality, we arrive at the condition:

$$b = \|A_z^2\| - \|A_x^2 + A_y^2\| = -\|A_x^2 + A_y^2 + A_z^2\|. \quad (3.17)$$

This equality in turn requires that $\|A_z^2\| \leq \|A_x^2 + A_y^2\|$ and that A_z^2 is anti-parallel to $A_x^2 + A_y^2$. If both these conditions are satisfied, we will have zero energy states at:

$$k = \pm \frac{1}{v} \sqrt{\|A_x^2 + A_y^2 + A_z^2\|} \quad (3.18a)$$

$$\phi = \frac{1}{2} \arctan \frac{(A_x \bar{A}_y + \bar{A}_x A_y)}{(\|A_x\|^2 - \|A_y\|^2)} \quad (3.18b)$$

Now, we reintroduce A_0 . Once again introducing a, b, c for the coefficients, the determinant is:

$$\begin{aligned} \text{Det}[H(\mathbf{k})] &= av^4k^4 + 2bv^2k^2 + c = \\ &v^4k^4 + 2 \left[\|A_z^2\| - \|A_0^2\| + (A_y^2 - A_x^2) \cos 2\phi - (A_x \bar{A}_y + \bar{A}_x A_y) \sin 2\phi \right] v^2k^2 \\ &\quad + \|A_x^2 + A_y^2 + A_z^2 - A_0^2\|^2. \end{aligned} \quad (3.19)$$

The form of the roots and the conditions placed on b are the same as for the case without A_0 . Now when we maximize with respect to ϕ , we find the limits on b :

$$\|A_z^2\| - \|A_0^2\| - \|A_x^2 + A_y^2\| \leq b \leq \|A_z^2\| - \|A_0^2\| + \|A_x^2 + A_y^2\|. \quad (3.20)$$

In this case, the discriminant is not necessarily zero, and there will be four different solutions for k . There is an interval in which b may reside:

$$\|A_z^2\| - \|A_0^2\| - \|A_x^2 + A_y^2\| \leq b \leq -\|A_x^2 + A_y^2 + A_z^2 - A_0^2\|. \quad (3.21)$$

Since b will attain the lower limit for some ϕ , we know that there will be at least some zero energy state as long as:

$$\|A_z^2\| - \|A_0^2\| - \|A_x^2 + A_y^2\| \leq -\|A_x^2 + A_y^2 + A_z^2 - A_0^2\|. \quad (3.22)$$

3.2.3 Network Models

The analysis of the gauge fields reveals that under the right conditions bilayers near commensuration display a mosaic of gapped and ungapped regions. We find the latter often percolate throughout the system, forming topologically protected wires. The system can display an emergent topologically protected network. This will occur if different gapped

regions of the supercell are topologically inequivalent. For a large enough system, protected midgap modes will appear on the boundaries of these regions. Then the electronic structure of the whole system within the gap is equivalent to that of this network.

Below, we will develop two important examples of network models: near zero degrees with bias, and near 38.2° .

3.3 Network Model: Near Zero Degrees

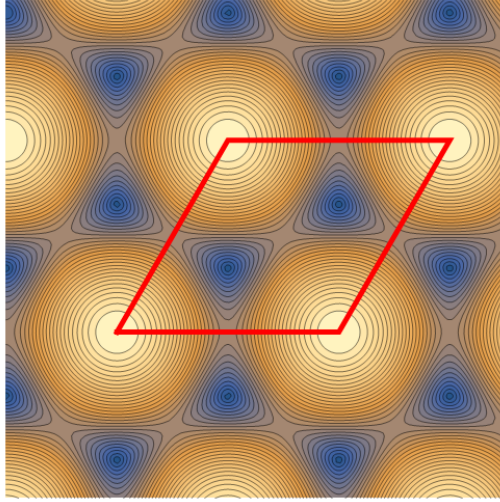
The near zero case is the most well-studied twisted bilayer in the literature. We have already explained the non-perturbative regime exhibits localization in AA stacked regions and a series of magic angles. This localization is not due to local gaps. In fact, this system has $A_z = 0$ everywhere and has no local gap. However, we now apply an interlayer bias V_0 . This bias locally gaps AB and BA stacked regions with opposite mass, creating a topologically protected network [29]. The forms of the gauge fields are given in the Appendix. Their graphical form is shown in Figure 3.4.

3.3.1 Semi-classical Picture

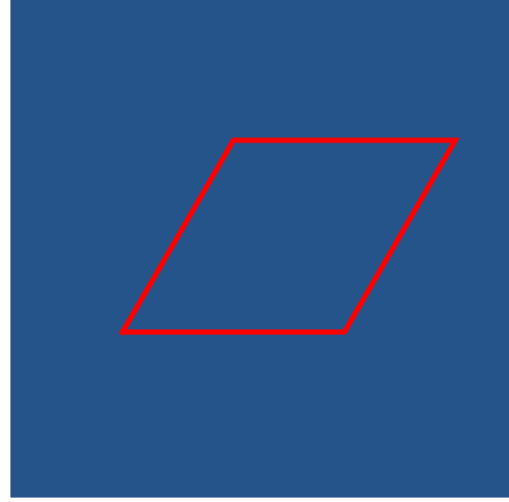
Near zero degrees there is no mass gauge field, and thus no possibility for a gap. The interlayer bias provides another avenue for opening a gap. Using the same technique as in the general case, we derive a condition for the existence of zero energy states:

$$-||A_0^2|| - V_0^2 - ||A_x^2 + A_y^2|| \leq -||A_x^2 + A_y^2 - A_0^2||^2 - V_0^4 - 2V_0^2(||A_x^2|| + ||A_y^2|| + ||A_0^2||). \quad (3.23)$$

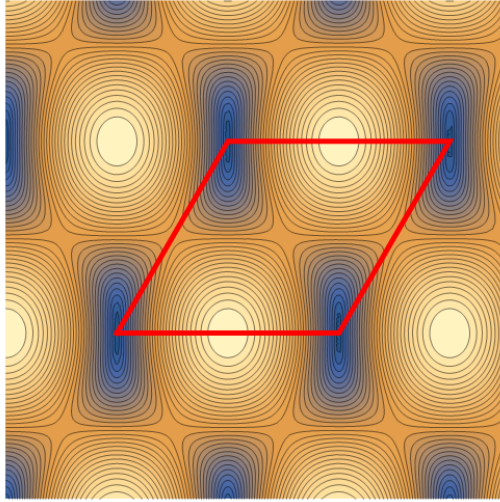
Semi-classically, we expect electron density to be expelled from gapped regions. States of the supercell must be confined to locally ungapped regions. In Figure 3.5, we show regions of the supercell that have a zero energy state. We see that electron density must be confined to a hexagonal network.



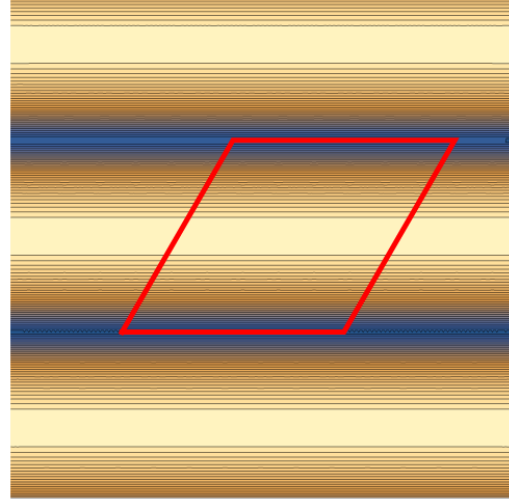
(a) $A_0 \in (0, 3)$



(b) $A_z \in (0, 0)$



(c) $A_x \in (0, 1)$



(d) $A_y \in (0, \sqrt{3})$

Figure 3.4: Magnitude of A_0 , A_z , A_x , and A_y of a near 0° commensuration. In each case there are 30 equally spaced contours in the given range in units of $\tilde{\gamma}_0$.

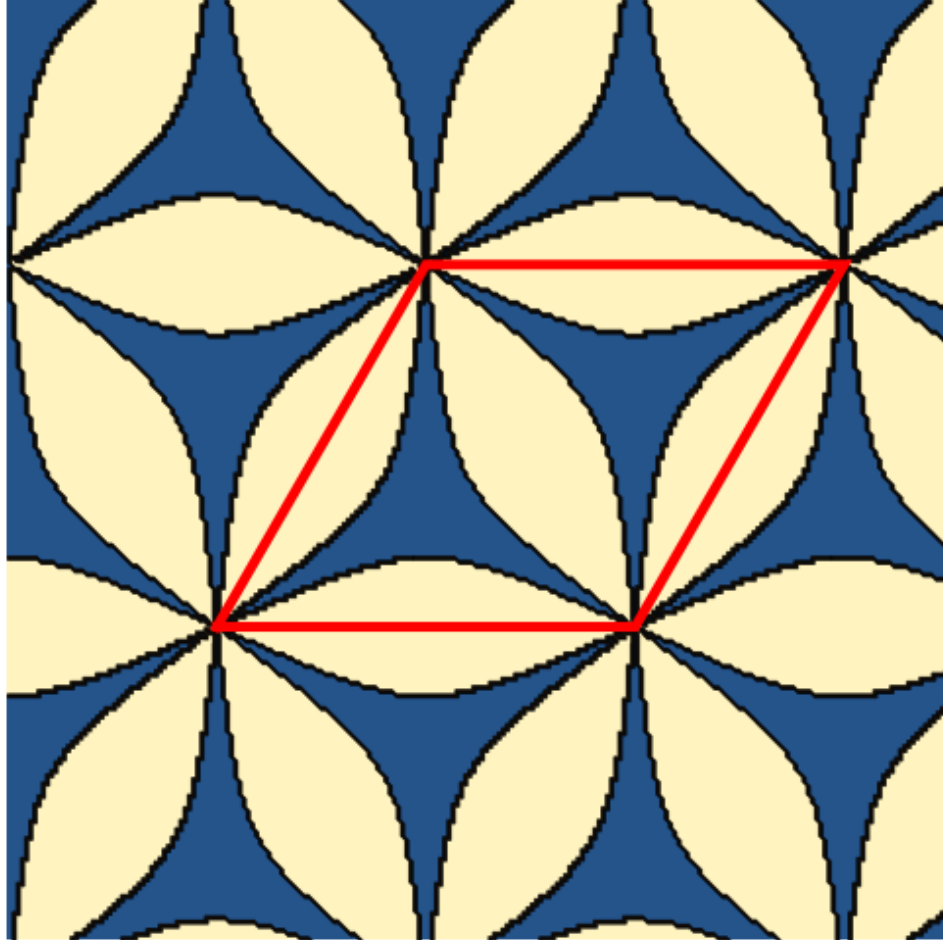


Figure 3.5: Semi-classically allowed states near 0° with $V_0 = \tilde{\gamma}_0$. Yellow regions have zero energy states. Blue regions do not.

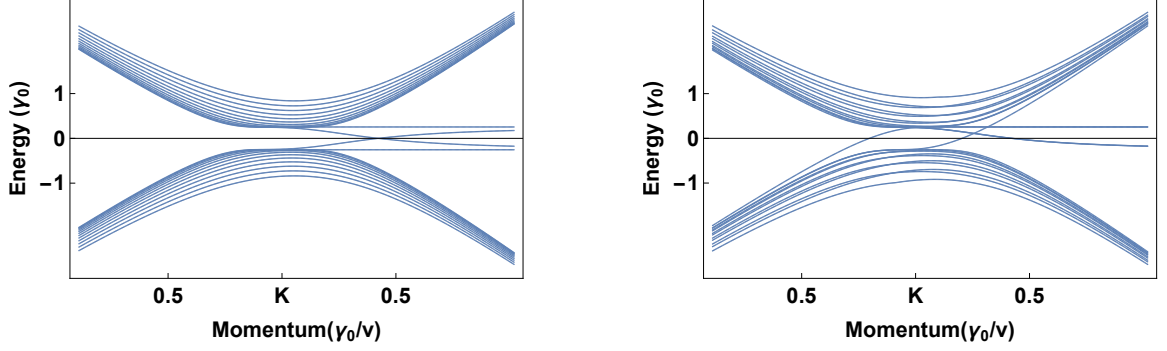


Figure 3.6: Topological midgap states at AB/BA domain boundary. A tight binding calculation was performed on a strip of graphene. On the left is the strip with no domain wall. On the right is the strip with the domain wall. The two gap states are clearly visible. The additional midgap states are localized to the edge of the strip and will not show up in a continuous sample.

3.3.2 Network Model

The emergent topology for this system was established in [32]. The gapped regions alternate between AB and BA stacking throughout the supercell. It can also be shown that AB and BA regions display opposite valley Chern numbers of ± 1 . Therefore, whenever we cross from one gapped region to another, we observe a gap closing and a net change in Chern number of ± 2 .

The ± 2 change in Chern number means there will be two topologically protected modes per valley in the ungapped regions. Each of these travel in the same direction. We verify these gap states with a tight binding model on a strip of graphene. In the middle of the strip is a domain wall separating AB and BA stacked regions under a bias. The results are shown in Figure 3.6. On the left is the strip with no domain wall. On the right is the strip with the domain wall. The two gap states are clearly visible. The additional midgap states are localized to the edge of the strip and will not show up in a continuous sample.

3.4 Network Model: Near 38.2°

Once we enter the non-perturbative regime near 38.2° , the gauge fields take a qualitatively different form. We note that $\tilde{\gamma}_{38} \sim 2.3\text{meV}$. Thus, we expect the effect to be smaller.

However, we may compensate for this by approaching the angle closer.

3.4.1 Gauge Fields

The exact expressions for the gauge fields are reproduced in the Appendix. Note, we use non-orthogonal coordinates for those equations out of convenience. In Figure 3.7 , we reproduce the graphical form of these fields.

Figure 3.8 shows the semi-classical picture. Lines connecting SE odd nodes semiclassically have states because the spectrum is gapless. Near these gapless lines, the gap is small, and the A_0 can shift states to zero energy. Thus, in some region near the line there still exist semi-classical states at zero energy. As the mass gauge field increases towards the SE even regions, the mass gauge field overwhelms everything, creating an insurmountable gap, and there are no semi-classical states at zero energy.

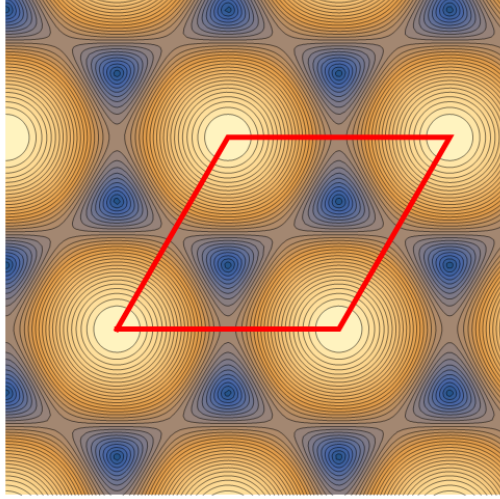
A general analytic solution for the semiclassical, local electronic structure is not possible. However, we can find solutions in special cases. We reproduce these here. Exactly at the corners of the supercell, the local stacking is SE even. The analytic solution is:

$$\begin{aligned} E(k) &= \pm \sqrt{9\tilde{\gamma}_{38}^2 + v^2k^2 \pm 3\tilde{\gamma}_{38}vk\sqrt{-\cos\theta + \sqrt{3}\sin\theta + 2}} \\ E(k) &= \pm \sqrt{9\tilde{\gamma}_{38}^2 + v^2k^2 \mp 3\tilde{\gamma}_{38}vk\sqrt{-\cos\theta + \sqrt{3}\sin\theta + 2}}. \end{aligned} \quad (3.24)$$

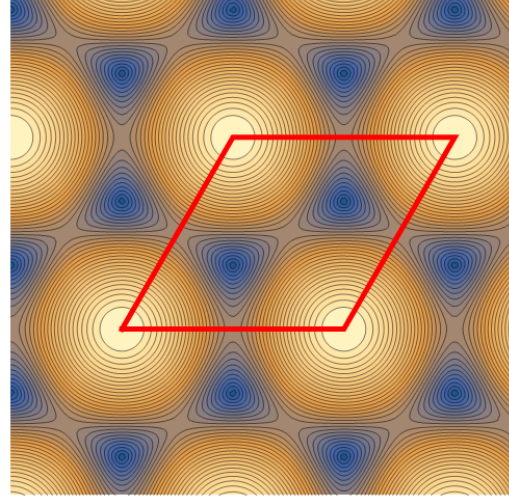
At the two SE odd points, the bands are:

$$\begin{aligned} E(k) &= \pm \frac{1}{\sqrt{2}} \sqrt{9\tilde{\gamma}_{38}^2 + 2v^2k^2 \pm 3\tilde{\gamma}_{38}\sqrt{9\tilde{\gamma}_{38}^2 + 4v^2k^2}} \\ E(k) &= \pm \frac{1}{\sqrt{2}} \sqrt{9\tilde{\gamma}_{38}^2 + 2v^2k^2 \mp 3\tilde{\gamma}_{38}\sqrt{9\tilde{\gamma}_{38}^2 + 4v^2k^2}}. \end{aligned} \quad (3.25)$$

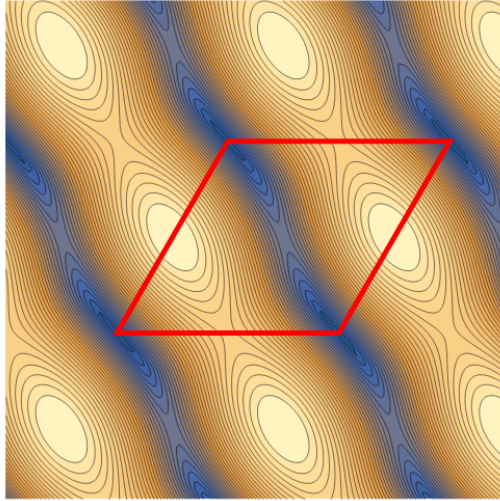
In both cases, the bands are radially symmetric. The even solution is gapped and the odd solution is ungapped, as expected. Away from these points, the situation is more complicated. Along the lines connecting SE odd nodes, there are degenerate states. We show the two lowest states along this line in Figure 3.9. At the SE odd nodes, we have the nor-



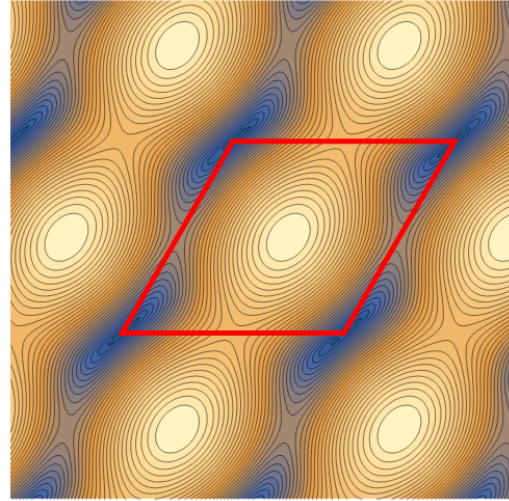
(a) $A_0 \in (0, .57)$



(b) $A_z \in (0, 2.95)$



(c) $A_x \in (0, 1.89)$



(d) $A_y \in (0, 1.96)$

Figure 3.7: Magnitude of A_0 , A_z , A_x , and A_y of a near 38° commensuration. In each case there are 30 equally spaced contours in the given range in units of $\tilde{\gamma}_{38}$.

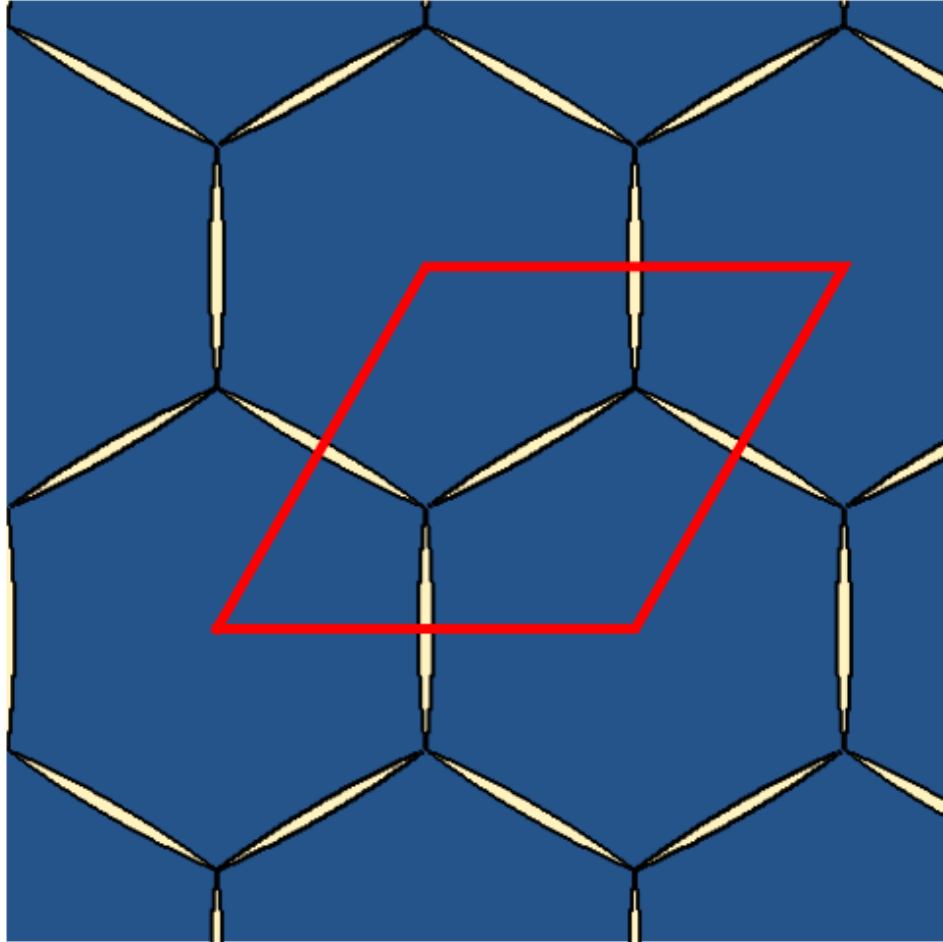


Figure 3.8: Semi-classically allowed states near 38.2° . Yellow regions have zero energy states. Blue regions do not.

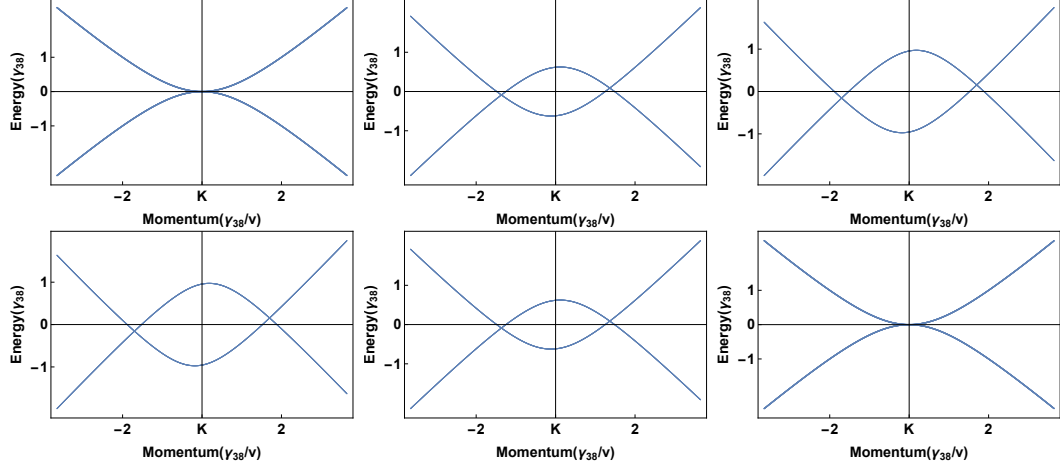


Figure 3.9: Local band structure along the line of degeneracy. Top left is one node and bottom right is the other node.

mal odd commensuration band structure. As we move along the line, there are two isolated points with degenerate states. Locally the bands are linear near these degenerate points, so we consider them Dirac pseudovalleys. The separation between the pseudovalleys increases until the halfway point of the link. As we move towards the opposite node, the pseudovalleys rejoin.

Along this line, only the solution exactly halfway between SE odd nodes is simple:

$$\begin{aligned}
 E(k) &= \pm 2\tilde{\gamma}_{38} \mp \sqrt{\sqrt{7}\tilde{\gamma}_{38}^2 \mp \tilde{\gamma}_{38}vk + \sqrt{7}v^2k^2} \\
 E(k) &= \pm 2\tilde{\gamma}_{38} \pm \sqrt{\sqrt{7}\tilde{\gamma}_{38}^2 \mp \tilde{\gamma}_{38}vk + \sqrt{7}v^2k^2}.
 \end{aligned} \tag{3.26}$$

Away from the line of degeneracy, the pseudovalleys become gapped. Figure 3.10 shows the two lowest bands exactly at the midway point of the link (blue), and then as we move in the direction perpendicular to the link. The gap opens and becomes larger as we move away. The topological invariants of these pseudovalleys are the key to understanding the network model. We turn to these invariants now.

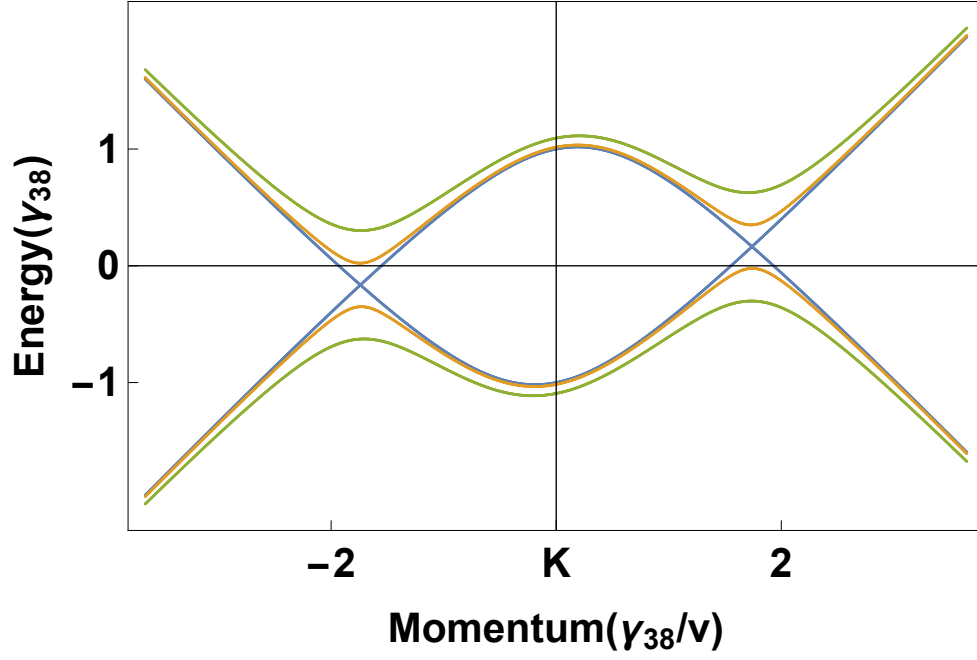


Figure 3.10: Two lowest energy bands midway on the link (blue), slightly away in the perpendicular direction to the link (yellow), and farther away (green).

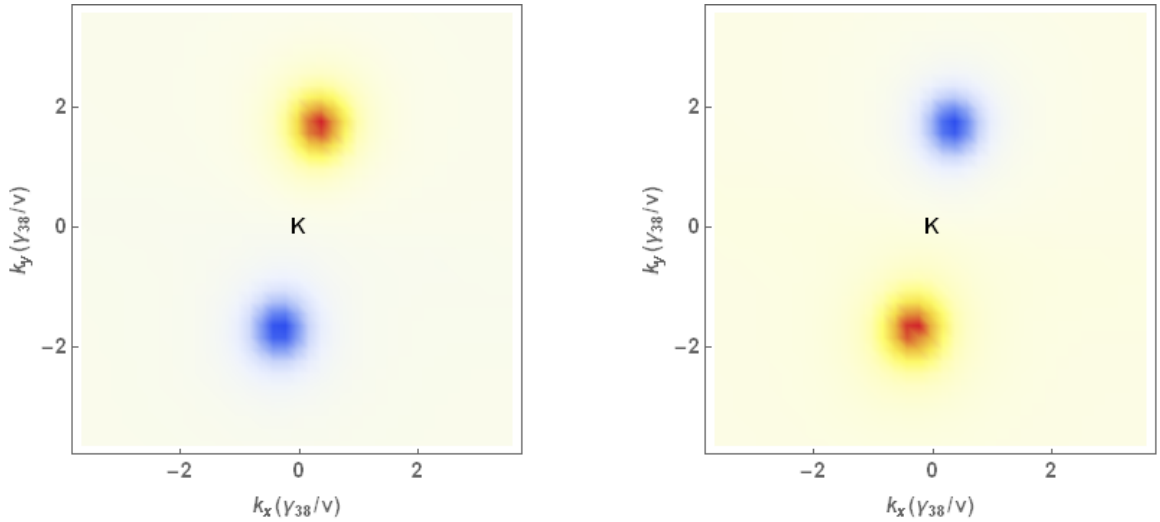


Figure 3.11: Berry curvature at the Dirac point on either side of the degenerate line. The left panel is on the left of the degenerate line, and the right panel is on the right of the degenerate line. The curvature changes sign in each pseudovalley across the line.

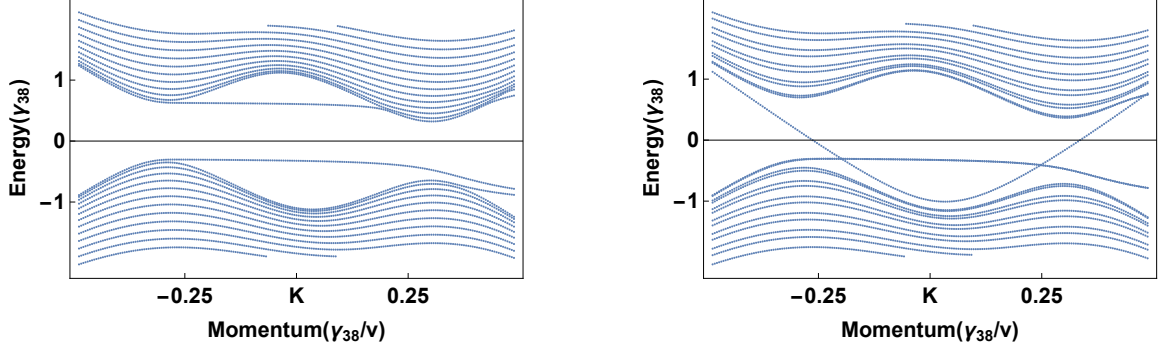


Figure 3.12: Topological midgap states at domain boundary of near 38.2° bilayer. Interlayer coupling is exaggerated for clarity.

3.4.2 Network Model

We now introduce a network model to describe the low energy band structure of the superlattice. The key point is the existence of topologically protected modes originating with the pseudovalleys described above. In Figure 3.11, we plot the Berry curvature at the bilayer Dirac point on either side of the degenerate line. The two pseudovalleys are clearly visible with opposite curvature. In addition, the curvature in each pseudovalley changes sign across the degenerate line. This leads us to define the pseudovalley Chern number (see Section 1.5). Each pseudovalley has equal and opposite Chern number of $\pm 1/2$ that changes across the degenerate line. Thus, the pseudovalley Chern number changes by two across the degenerate line. This implies the degenerate lines are domain walls, along which we will find two midgap states. Each pseudovalley originates one of the midgap states. Because the sign change is opposite for each pseudovalley, the midgap states are counter-propagating.

We verify this argument with a tight binding model. In Figure 3.12, we show the bands of a bilayer strip with a domain wall as in the near 38° system. We use couplings derived from the local low energy Hamiltonians for the near 38° system. On the left, we use couplings that imply equal valley Chern numbers on both sides of the domain wall. Thus, we see no midgap states. On the right, we use couplings that imply opposite valley Chern numbers on both sides of the domain wall. Two counterpropagating midgap states appear.

We model these states as a network of SE odd nodes arranged in a honeycomb lattice

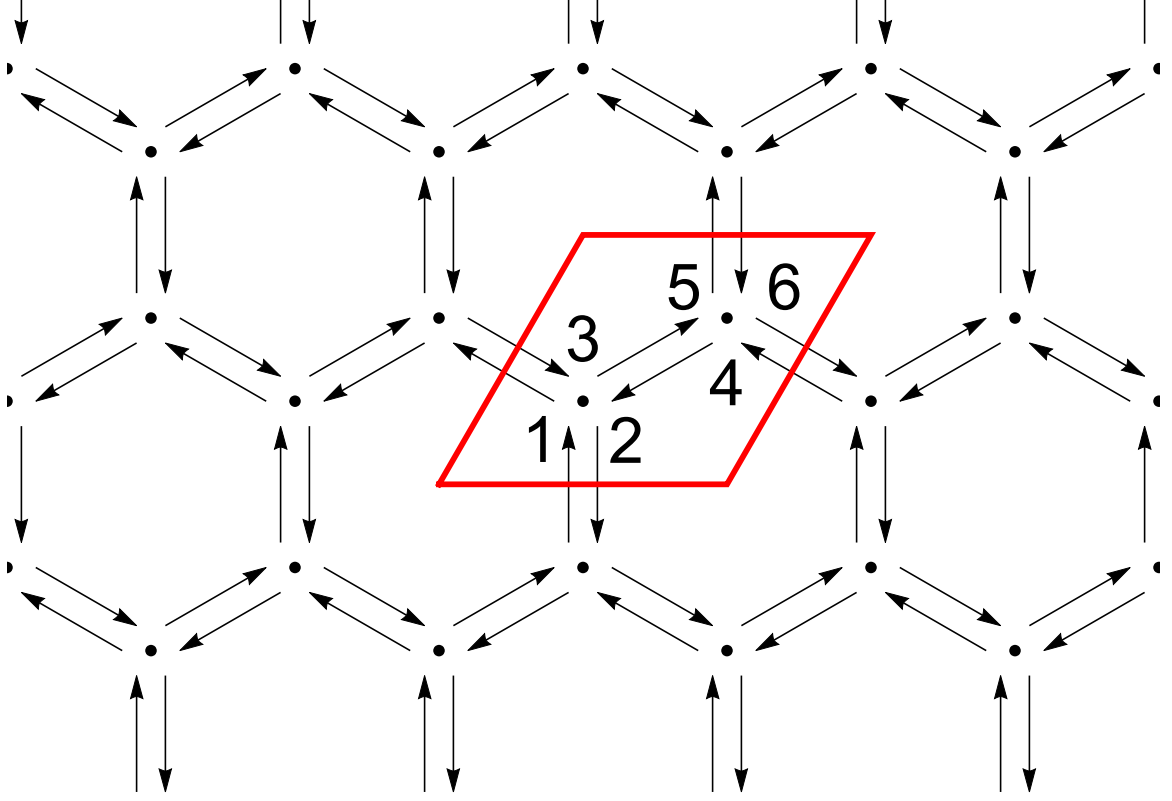


Figure 3.13: A schematic of the network model. Six midgap states scatter amongst the nodes of a honeycomb lattice defined by SE odd regions.

connected by one state traveling in each direction along the gapless lines in Figure 3.8. A schematic of the network is shown in Figure 3.13. Each arrow represents one of the topologically protected midgap states. The red lines represent the unit cell of the network. We see we need six states per unit cell.

There are three incoming and three outgoing states at each node. Let $|\psi\rangle_I$ be the six-dimensional vector of incoming states and $|\psi\rangle_O$ be the six-dimensional vector of outgoing states. We number these states as in Figure 3.13. We seek a model of the scattering of these six states.

First, we note that in the limit of large systems, scattering between the topologically protected nodes only occurs at the SE odd nodes. Scattering only occurs when the states satisfy the relation of Equation 2.12. In other words, the modes must be connected in momentum space by reciprocal superlattice vectors. This implies that the pseudo-valleys

of the local band structure must satisfy this relation. In the large system limit, the local band structure does not change. However, momentum vectors of the scattering process shrink. As these vectors shrink, only exponentially weak scattering processes will connect the topologically protected states. For a very large system, only the node itself, where the pseudo-valleys are coincident, will host any appreciable scattering.

Thus, as an electron percolates through the network, we consider two different processes. First, an electron in an incoming mode scatters off a node into the three associated outgoing states of that node. We use the unitary matrix U to describe this process. Second, an electron traverses a link from one node to another. We use the unitary matrix $e^{i\epsilon}M(\mathbf{k})$ to describe this process. The matrix M describes the geometry of the network and contains the momentum dependence, that is the Bloch phase picked up by electrons moving through the system. The real number ϵ is the phase picked up by traversing a link. The states of the system must satisfy:

$$|\psi\rangle_O = U |\psi\rangle_I = e^{i\epsilon}UM(\mathbf{k}) |\psi\rangle_O. \quad (3.27)$$

We have an eigenvalue equation with eigenvalue $e^{i\epsilon}$. Based on our analysis of the network, we also know that the energy $E = \epsilon v/L$, where L is the length of the link and v is the velocity of the traversing state. Thus, we can find the energy of the network of states.

We now turn to the form of the scattering matrix U . In general, we write:

$$U = \begin{pmatrix} U_1 & 0 \\ 0 & U_2 \end{pmatrix} \quad (3.28a)$$

$$U_j = e^{i\lambda_j J_j} \quad \text{for } J_j \text{ Hermitian}, \quad (3.28b)$$

where U_j describes the scattering at node j . Consider the first node. We divide the

matrix J_j into three components:

$$J_j = J_{j,0} + J_{j,r} + J_{j,i}, \quad (3.29)$$

where $J_{j,0}$ is proportional to the identity, $J_{j,r}$ is totally real, and $J_{j,i}$ is totally imaginary. Because J_j is Hermitian, each of these components is also Hermitian. We now use the symmetry of the network to restrict the scattering matrix.

First, we have C_3 symmetry. C_3 rotations about a node relate all scattering processes through that node of equal handedness. That is, all scattering processes involving the electron turning left (right) must be equal. In the case of $J_{j,r}$, opposite handed scattering processes are equal by hermiticity. Thus, all elements of $J_{j,r}$ are equal. We may absorb the equal diagonal elements into $J_{j,0}$ and assume $J_{j,r}$ is zero on its diagonal. In the case of $J_{j,i}$, opposite handed scattering processes are opposite sign by hermiticity. Thus, all elements of $J_{j,i}$ are of equal magnitude with sign determined by handedness.

Second, there is reflection symmetry along the link. This reverses the handedness of one of the scattering processes, ensuring that all scattering processes are equal in sign. Therefore, all elements of $J_{j,i}$ are zero.

Finally $J_{j,0}$ is just a constant prefactor which we parametrize with $\lambda_j^{(0)}$. Therefore, we find the scattering at node j is described by:

$$U_j = e^{i\lambda_j^{(0)}} e^{i\lambda_j J_{j,r}} \quad (3.30a)$$

$$J_{j,r} = \begin{pmatrix} 0 & 1 & 1 \\ 1 & 0 & 1 \\ 1 & 1 & 0 \end{pmatrix}. \quad (3.30b)$$

We have four parameters: $\lambda_j^{(0)}$ and λ_j for $j = 1, 2$. However, we have the additional

symmetry of point reflection on the center of the line connecting the nodes. This relates each mode at node one to a mode at node two. Since we have already determined the modes at a single node are related by C_3 symmetry, the additional reflection symmetry requires $U_1 = U_2$. Thus, we reduce to the two parameters λ and $\lambda^{(0)}$. The latter is simply a rigid shift and can be discarded. Thus, we have reduced the scattering to a single free parameter λ .

The matrix M depends on the geometry of the problem. Given our conventions, we find:

$$M = \begin{pmatrix} 0 & 0 & 0 & 0 & 0 & e^{i2\pi k_1} \\ 0 & 0 & 0 & 0 & e^{i2\pi k_2} & 0 \\ 0 & 0 & 0 & 1 & 0 & 0 \\ 0 & 0 & 1 & 0 & 0 & 0 \\ 0 & e^{-i2\pi k_2} & 0 & 0 & 0 & 0 \\ e^{-i2\pi k_1} & 0 & 0 & 0 & 0 & 0 \end{pmatrix}, \quad (3.31)$$

where k_1 and k_2 correspond to the projection of momentum onto the reciprocal super-lattice vectors .

Solving the eigenvalue problem, we find the bands shown in Figure 3.14. We show bands for increasing λ , restricted to the interval $[0, 2\pi/3)$. All λ differing by $2\pi/3$ are equivalent because systems differing by $2\pi/3$ are the same up to a rigid shift in phase. This is evident from the relation:

$$e^{i2\pi S_1/3} = e^{-i2\pi/3} I_3, \quad (3.32)$$

where I_3 is the three by three identity matrix . In other words, increasing λ by $2\pi/3$ only multiplies the eigenvalue equation by an overall phase and shifts all arguments of eigenvalues by the same amount.

We see that for most values of λ , the bands are similar to those of a Kagome lattice. In

particular, we have two dispersive bands with a pair of Dirac cones at the Dirac points of the supercell, and one completely flat band. When $\lambda = 2n\pi/3$, we have total reflection at the nodes. This produces the expected degenerate flat bands. When $\lambda = \pi/3$, the system crosses over from having the flat band on top versus on bottom.

In Figure 3.15, we show a three dimensional plot for $\lambda = 1.3$. Here we very clearly see all three Kagome bands. The bandwidth, B , is the difference between the highest and lowest energy state of one Kagome triple . We find:

$$B = \frac{v}{L} \begin{cases} 2\pi - 3\lambda & 2(n+1)\pi/3 \leq \lambda < 2n\pi/3 \\ 3\lambda & 2n\pi/3 \leq \lambda < 2(n+1)\pi/3 \end{cases}, \quad (3.33)$$

where L is the length of a link. Thus, the bandwidth depends on the scattering parameter, but it is always bounded above by $\pi v/L$.

3.4.3 Momentum Space Verification

To verify the network model, we turn to the methods outlined at the beginning of this chapter. Recall the first method was to truncate a matrix involving all single layer states coupled by the interlayer function. The matrix has the form:

$$H = \begin{pmatrix} H_{(1)} & H_{\perp} \\ * & H_{(2)} \end{pmatrix}. \quad (3.34)$$

$H_{(1)}$ and $H_{(2)}$ are block diagonal matrices that contain the Dirac Hamiltonians describing the low energy states of each layer . The vector \mathbf{q}_l^i is the momentum space location of the Dirac point of state i in layer l . Thus, we have:

$$H_{(l)} = \text{diag}_i[H_0(\mathbf{q}_l^i)], \quad (3.35)$$

where i ranges over all the states included in the momentum space truncation and diag

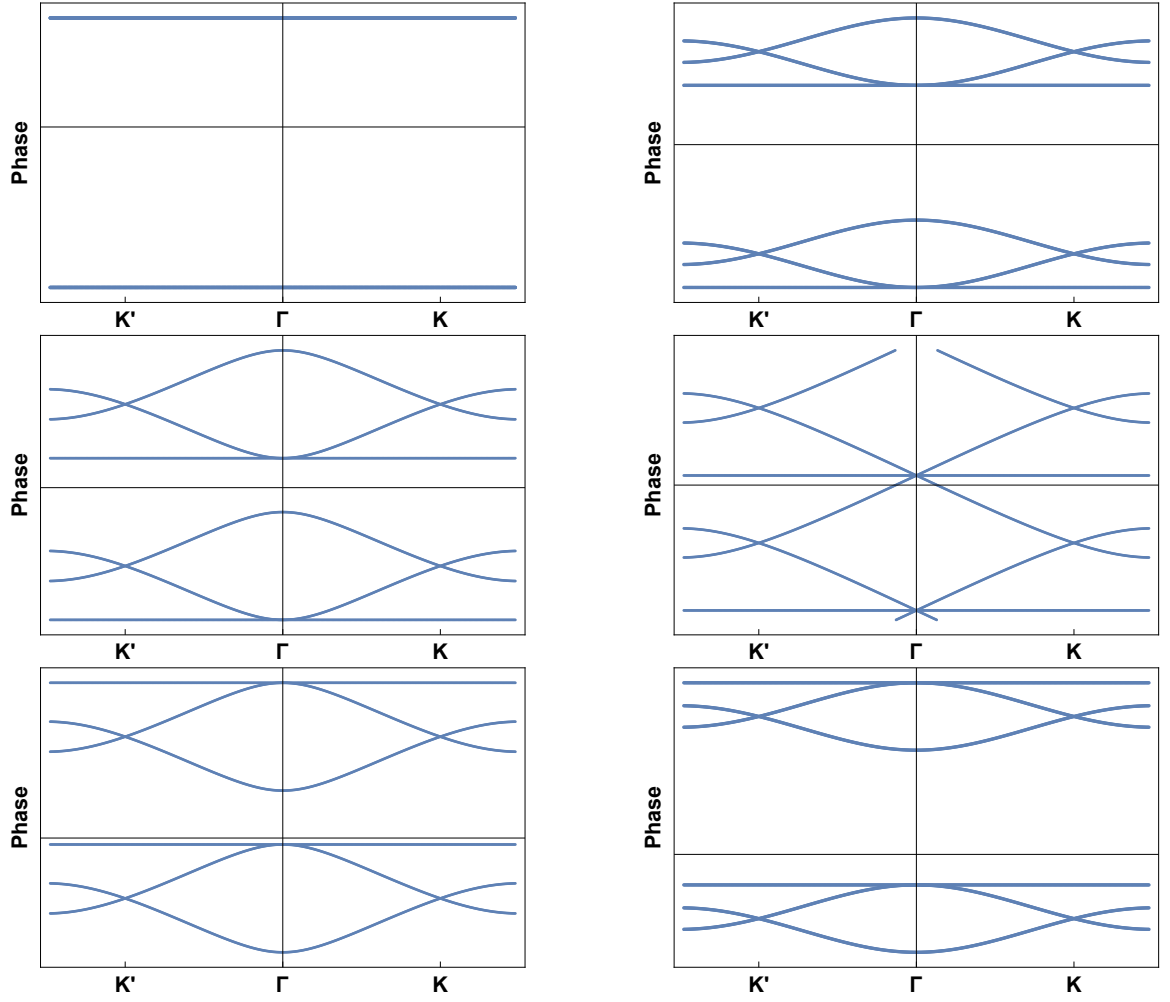


Figure 3.14: Bands from the network model with $\lambda \in [0, 2\pi/3)$. The plotted values are the phase ϵ from Equation 3.27. This unitless phase is independent of system size. To convert to energy, it is necessary to multiply by a factor of v/L , where L is the length of a link.

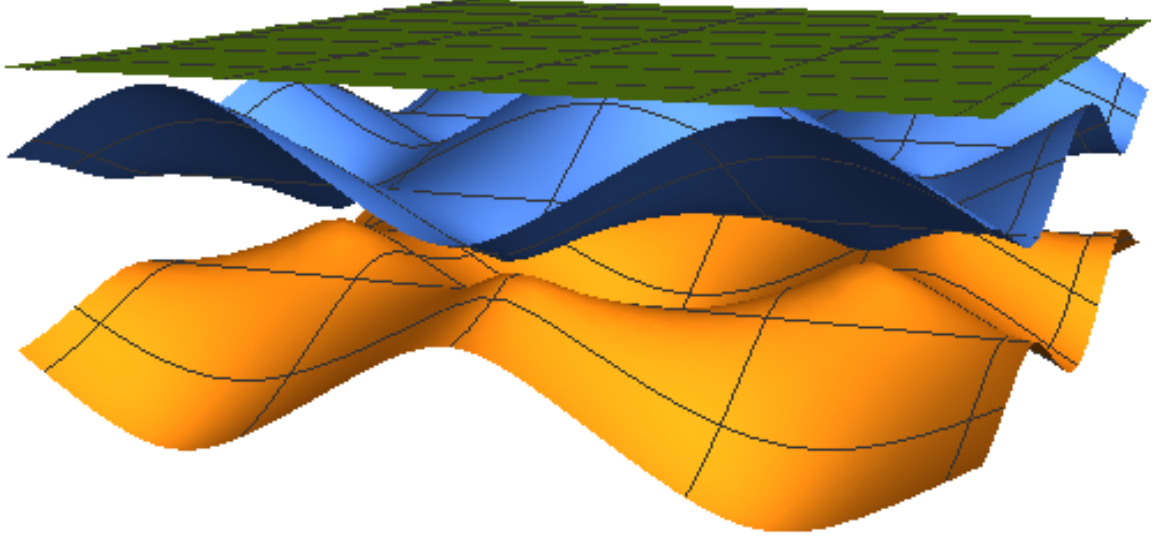


Figure 3.15: Three dimensional plot of the network model bands with $\lambda = 1.3$. The Kagome structure of the bands is clear.

indicates arranging the arguments in diagonal blocks . The blocks themselves are:

$$H_0(\mathbf{q}_l^i) = (\mathbf{k} - \mathbf{q}_l^i)\boldsymbol{\sigma}_l, \quad (3.36)$$

where $\boldsymbol{\sigma}_l$ are the Pauli matrices corresponding to layer l . Note that σ_l includes any rotation that is present in layer l .

The interlayer coupling H_\perp describes how the Dirac equations couple between the layers. For every state i , we consider the three states of the opposite layer to which it couples most strongly. The matrix form of these couplings is:

$$H_\perp^1 = \tilde{\gamma}_{38} \begin{pmatrix} 1 & 1 \\ e^{-i2\pi/3} & e^{-i2\pi/3} \end{pmatrix} \quad (3.37a)$$

$$H_\perp^2 = \tilde{\gamma}_{38} \begin{pmatrix} 1 & e^{i2\pi/3} \\ e^{i2\pi/3} & e^{-i2\pi/3} \end{pmatrix} \quad (3.37b)$$

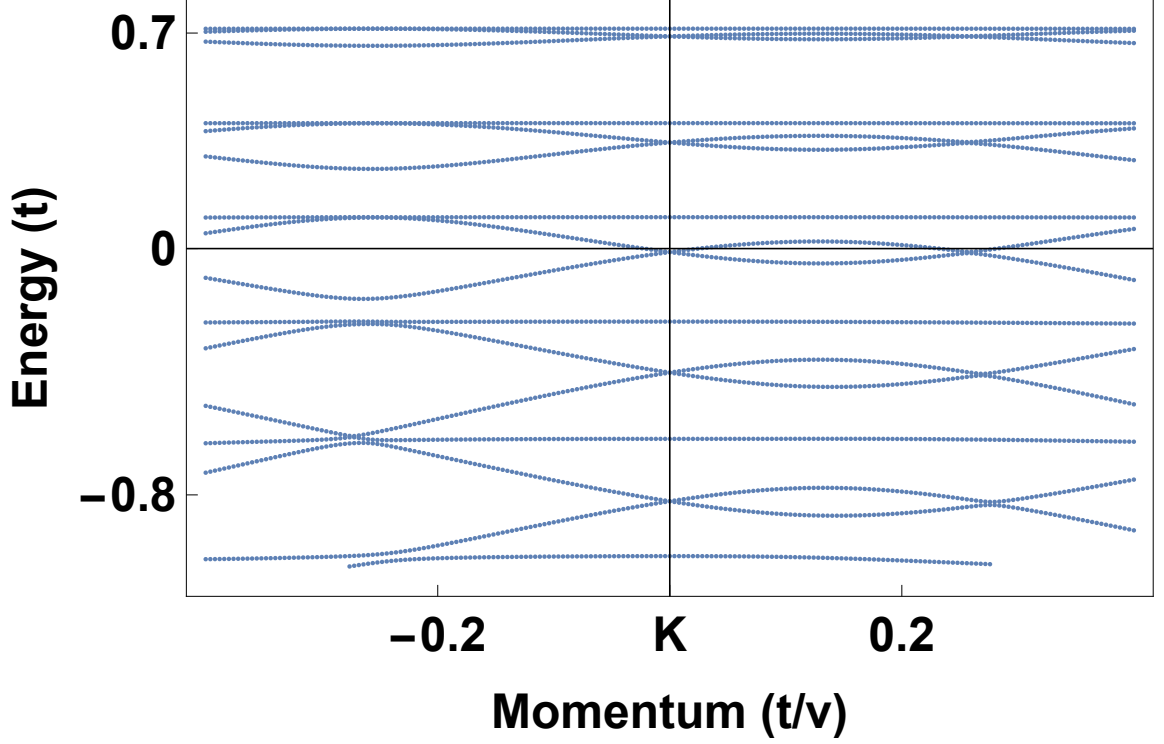


Figure 3.16: Bandstructure of a near 38.2° bilayer, as described by a momentum space matrix coupling the 818 lowest energy states of the separate graphene layers.

$$H_{\perp}^3 = \tilde{\gamma}_{38} \begin{pmatrix} 1 & e^{-i2\pi/3} \\ 1 & e^{-i2\pi/3} \end{pmatrix}. \quad (3.37c)$$

These are simply the three terms in the sum of Equation 2.17. Thus, every diagonal block will couple to three diagonal blocks of the opposite layer with the three couplings above.

We construct such a matrix for a near 38.2° bilayer with $\delta\theta$ such that $\tilde{\gamma}_{38}/v\delta K = 5.2$. We include 16 momentum space hops, resulting in a low energy matrix of dimension 818. The resulting band structure is shown in Figure 3.16.

We clearly see the expected Kagome band pattern. However, this method gives no insight into the real space localization of these states. For this, we turn to a tight binding model.

3.4.4 Tight Binding Verification

The second verification method is to construct a tight binding model. An immediate question is the functional form of the interlayer coupling $f(\mathbf{r})$. To create a realistic model, we choose a short range Gaussian of length l_r with a cut-off of length l_0 for computation efficiency:

$$f_1(r) = \gamma e^{-r^2/l_r^2} \Theta(l_0 - r). \quad (3.38)$$

In practice, we will choose l_0 such that $\exp(-l_0^2/l_r^2) \ll 1$. To choose the other parameters, we refer to the physical constants in Appendix A. We choose a value for l to match the known ratio $\tilde{\gamma}_0/\tilde{\gamma}_{38} = 48$ [22, 24]. This yields about $l_r = .665\delta$, where δ is the interatomic distance of graphene. We choose $\gamma = .39\text{eV} = .14t$ to match the known value $\tilde{\gamma}_0 = .11\text{eV} = .039t$. We can calculate the dimension of the matrix we would have to diagonalize to achieve the non-perturbative regime by calculating the angle for which $\tilde{\gamma}_{38} = v\delta K_{38}$, where δK_{38} is the momentum space difference between the nearest Dirac points of the two layers:

$$\sin \frac{\delta\theta}{2} = \frac{\delta K_{38}}{2|\mathcal{G}_{38}^1|} = \frac{3\tilde{\gamma}a}{8\pi\sqrt{7}v}. \quad (3.39)$$

We find $\delta\theta = .000086$. To find the size of the system, we find the area of the supercell, A , corresponding to this angle:

$$A = \frac{\sqrt{3}a^2}{14\delta\theta^2} + \mathcal{O}(\delta\theta^{-1}). \quad (3.40)$$

Then, the number of sites in the model is:

$$N_A = 4\frac{A}{A_0} = \frac{4}{7\delta\theta^2} = 7.3 \times 10^8, \quad (3.41)$$

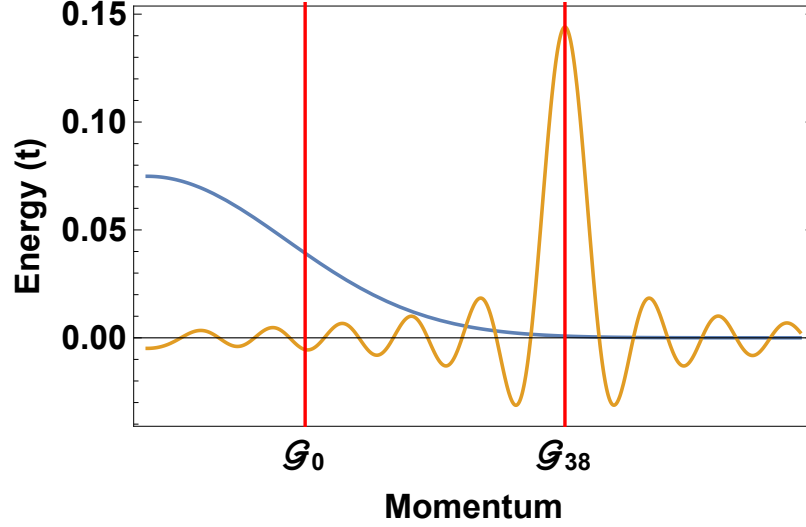


Figure 3.17: Fourier components of realistic coupling (blue) and artificial coupling (yellow). The red lines are the momenta corresponding to 0° and 38° commensuration effects.

where A is the area of the supercell and A_0 is area of the unit cell of graphene.

Diagonalization of a matrix this large is not feasible for us. Thus, we need to artificially enhance the strength of the coupling. In general, if we wish to maximize the effect of the commensuration at angle c , we need to maximize the Fourier component: $\tilde{\gamma}_c = \tilde{f}(\mathbf{K}_1 + \mathbf{G}_1)$ where (recalling Equation 2.12) $\mathbf{G}_1 \in \mathcal{G}_c^1$. One possibility is:

$$f_1(r) = \gamma J_0(|\mathcal{G}_c^1| r) \Theta(r - l_0), \quad (3.42)$$

where J_0 is the Bessel function of order zero and l_0 is a cutoff for computational efficiency. The prefactor γ controls the strength of the coupling. For the 38.2° commensuration, $|\mathcal{G}_{38}^1| = 4\pi\sqrt{7}/3a$. This coupling is a good choice because its Hankel transform approaches a delta function at the appropriate Fourier component as $l_0 \rightarrow \infty$.

In Figure 3.17, we plot the Fourier transform of the realistic coupling and the artificial coupling. We see that the artificial coupling is heavily concentrated on the 38.2° commensuration. Thus, it is a good choice for seeing the non-perturbative effects.

Now, we plot an energy eigenvector of the tight binding model. We look at the Dirac point and choose the state with energy closest to zero. The eigenvector is shown in Figure

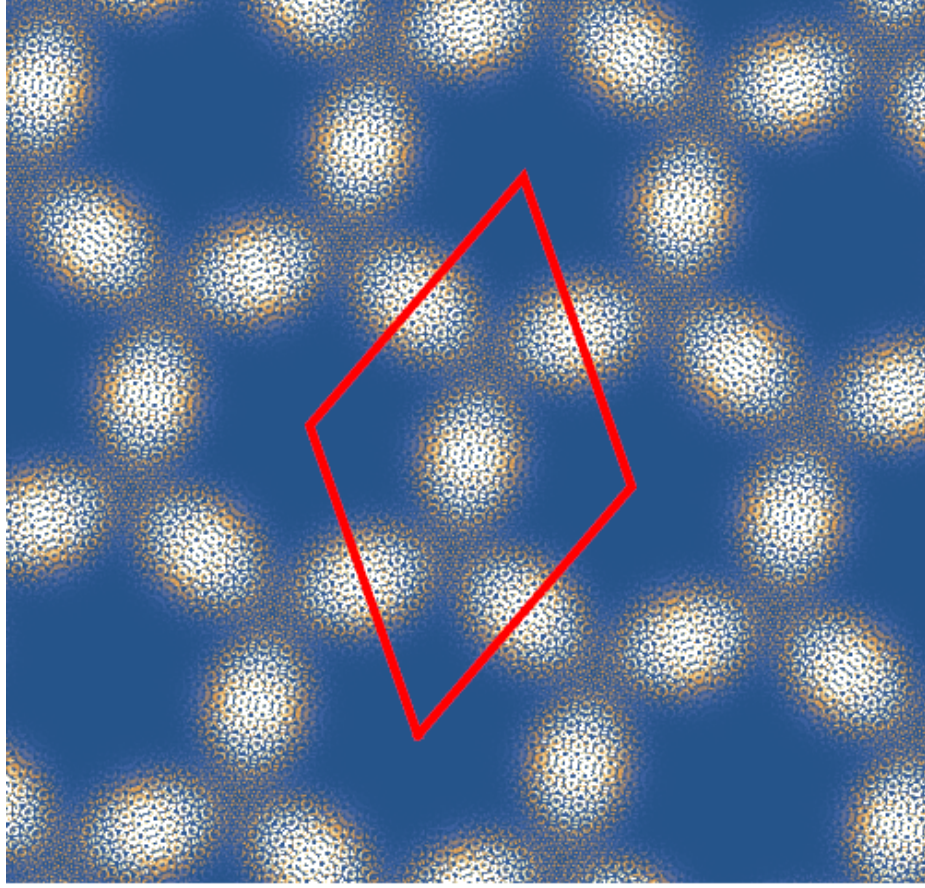


Figure 3.18: Lowest energy eigenvector of commensuration at $\theta = 38.546^\circ$ with artificial coupling. $\gamma = .2t$. The red lines are the supercell.

3.18. The pattern here is at $\theta = 38.546^\circ$ with 16972 atoms. The artificial coupling used has $\gamma = .2t$ and $l_0 = 6\delta$. This yields $\tilde{\gamma}_{38}/v\delta K_{38} = 2.6$. The red lines indicate the supercell. Electron density is expelled from the SE even regions as predicted. The density localizes to points halfway between the SE odd regions in a Kagome lattice pattern. This localization explains why we see the Kagome bands in the network model. The electron states localize in a Kagome pattern, producing an effective Kagome lattice on the scale of the supercell.

Next, we plot the wavefunctions for states at the Dirac point, but with energies farther from zero. The result is shown in Figure 3.21 for energies ranging from $-.143t$ to $.169t$. Close to zero energy we get several states in this Kagome form. As we move away from zero, we see variations in the pattern. However, the new patterns remain confined to the honeycomb network, even as they can enter farther into the SE even regions.

The band structure is shown in Figure 3.19. For the states with wavefunctions in the Kagome localization pattern, we get the Kagome triplet of one flat band and two dispersive bands touching at one point. The higher energy states with more complex localization have distorted Kagome triples. We can explain this with a simple extension of the network model.

We add a new process to the network model: backscattering at the middle of each link. We parametrize this process by adding the parameter p to the transfer matrix M .

$$M(\mathbf{k}) \rightarrow \cos(p)I + i \sin(p)M(\mathbf{k}). \quad (3.43)$$

We see that $p = \pi$ corresponds to total reflection on the links, while $p = \pi/2$ corresponds to total transmission. The bands for $p \in [\pi/2, \pi]$ are shown in Figure 3.20. First, we see that the flat band is robust to this backscattering. The main effect is to change the three band pattern into a six band pattern by introducing an asymmetry. At some critical p there is a triple degeneracy at Γ . For large p , both flat bands switch to the same dispersive pair and the other dispersive pair is left with no flat bands. We see all these patterns in Figure 3.19. Therefore, we conclude the network model captures the important physics of the system. In the limit of very large systems, only scattering at the nodes is present, and we will have perfect Kagome triplets.

We can also use the artificial coupling to refine our estimate of the real system size where these effects will become visible with a realistic coupling function. By scanning over γ in the artificial coupling, we first start to see localization around $\tilde{\gamma}_{38}/v\delta K_{38} = 1/2$. We then calculate the system size and find $\delta\theta = .00017$. This implies:

$$T_1 = \frac{a}{\sqrt{7}\delta\theta} = 3851\delta = 547\text{nm}, \quad (3.44)$$

where T_1 is the norm of a unit superlattice vector .

Therefore, we expect the network effect to dominate systems near 38.2° for supercells

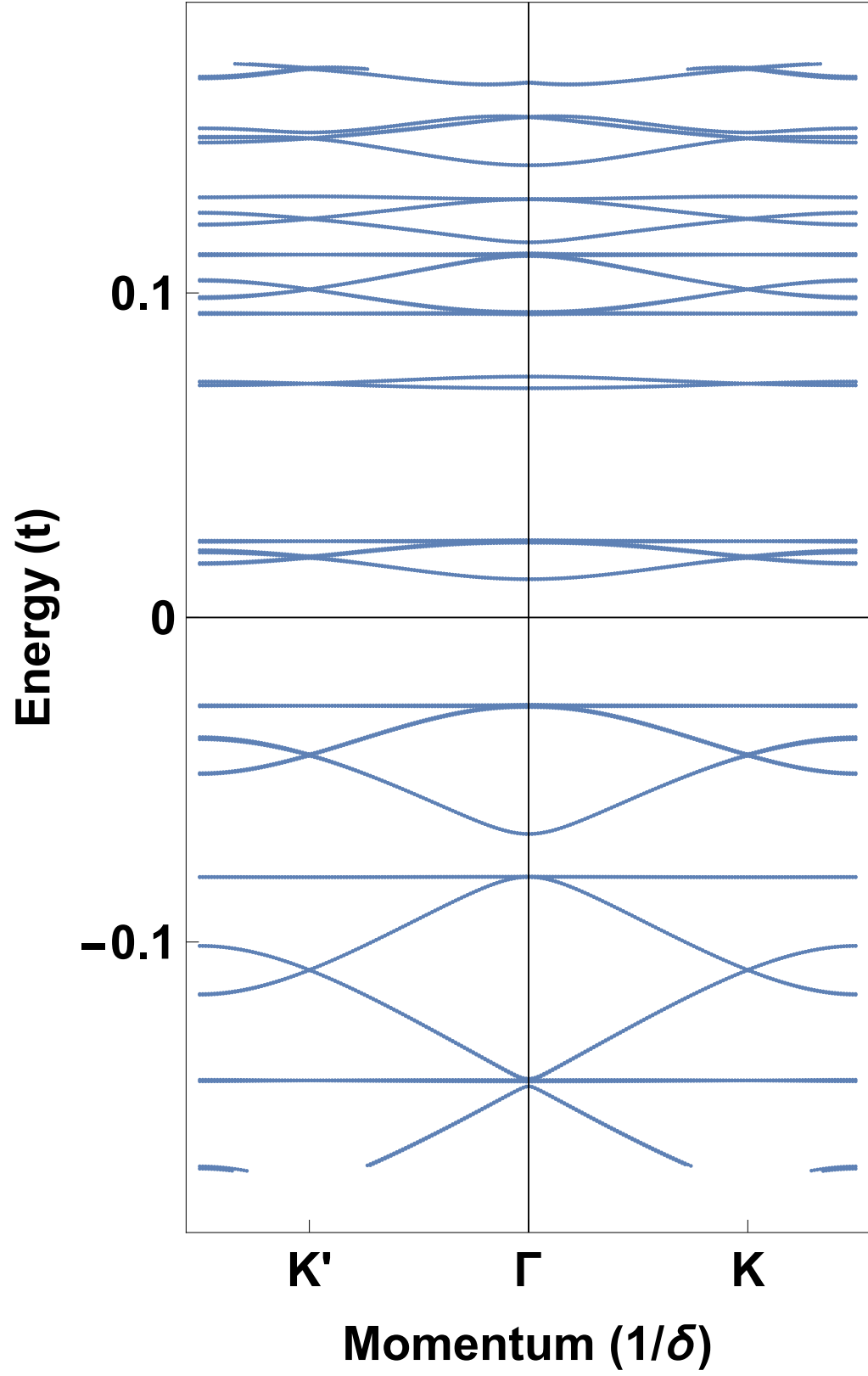


Figure 3.19: Lowest energy bands of commensuration at $\theta = 38.546^\circ$ with artificial coupling.

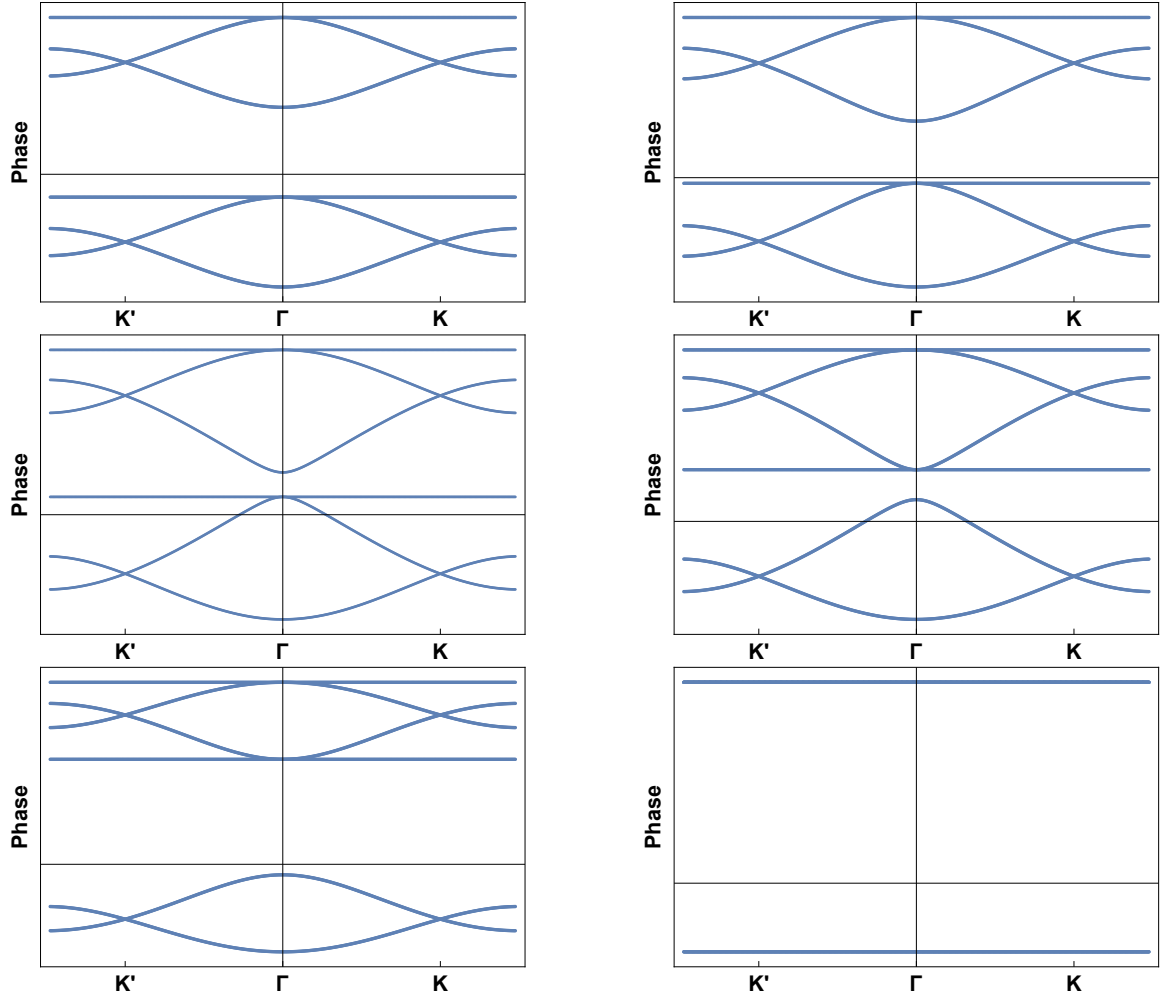


Figure 3.20: Bands from the network model with $\lambda = \pi/2$ and $p \in [\pi/2, \pi]$.

of size 547nm on a side and larger. In other words, we require a period in the commensuration pattern of about 547nm.

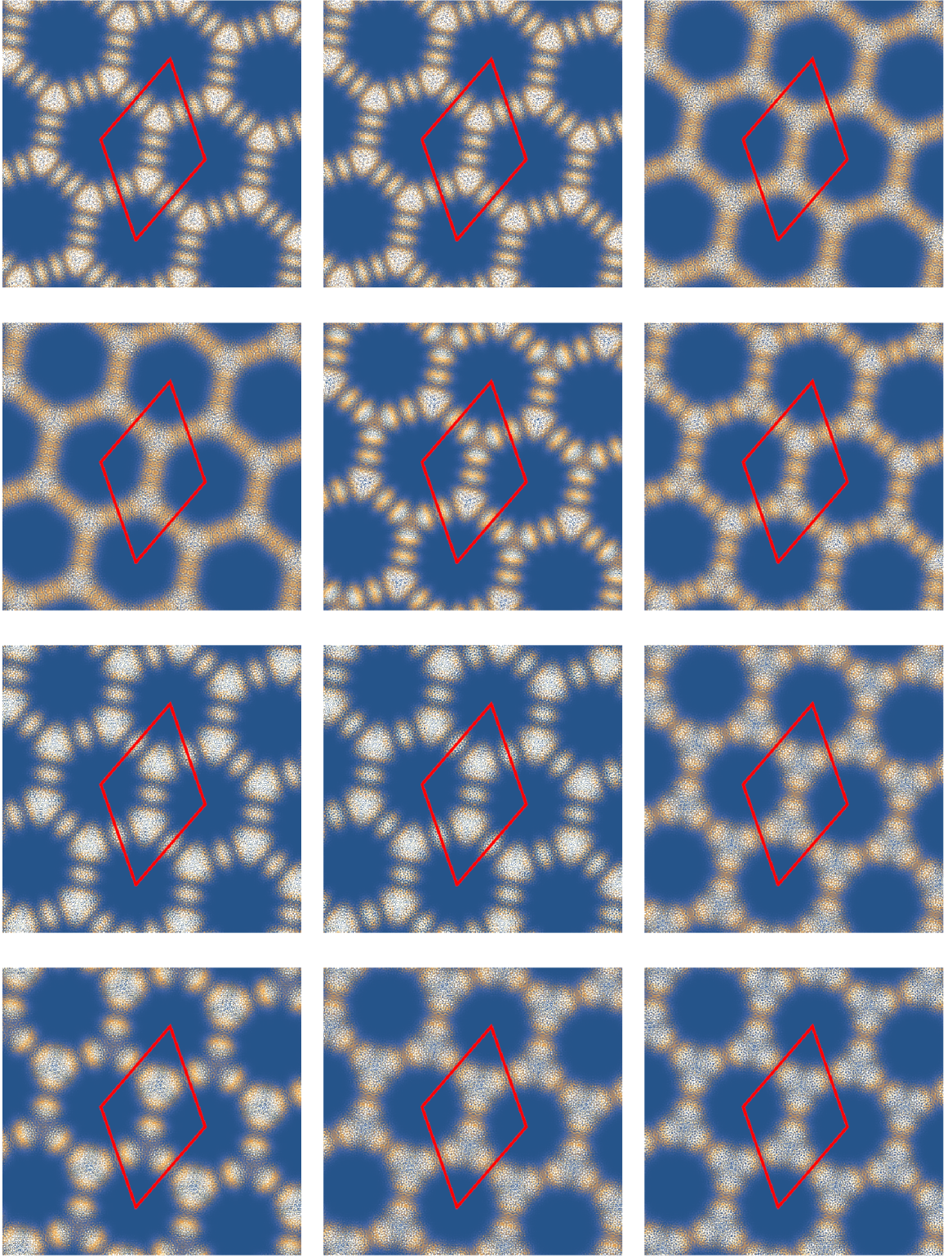


Figure 3.21: Set of low energy eigenvectors of commensuration at $\theta = 38.546^\circ$ with artificial coupling, $\gamma = .2t$. The red lines are the supercell.

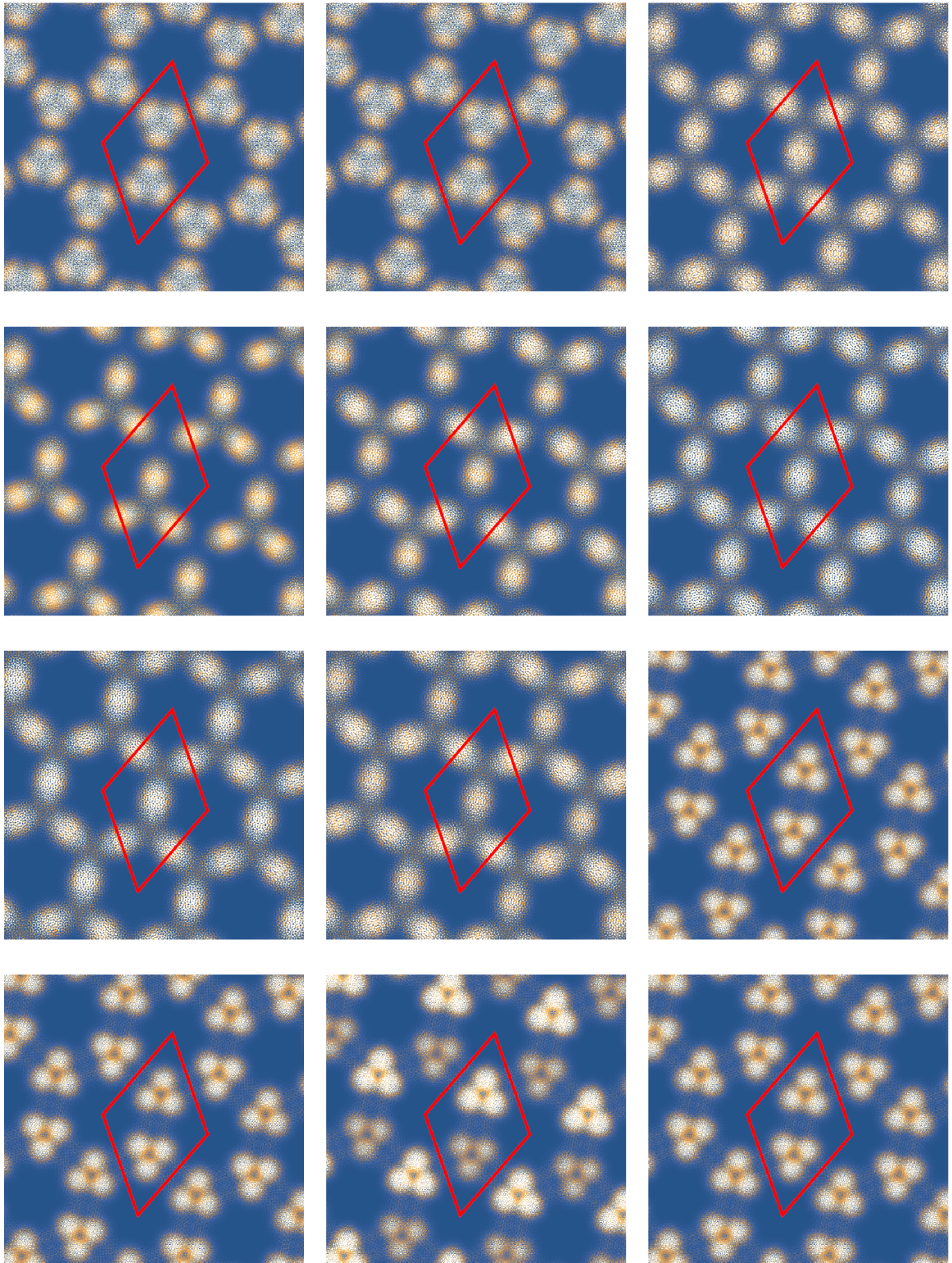


Figure 3.21: Continued (repeated from page 63)

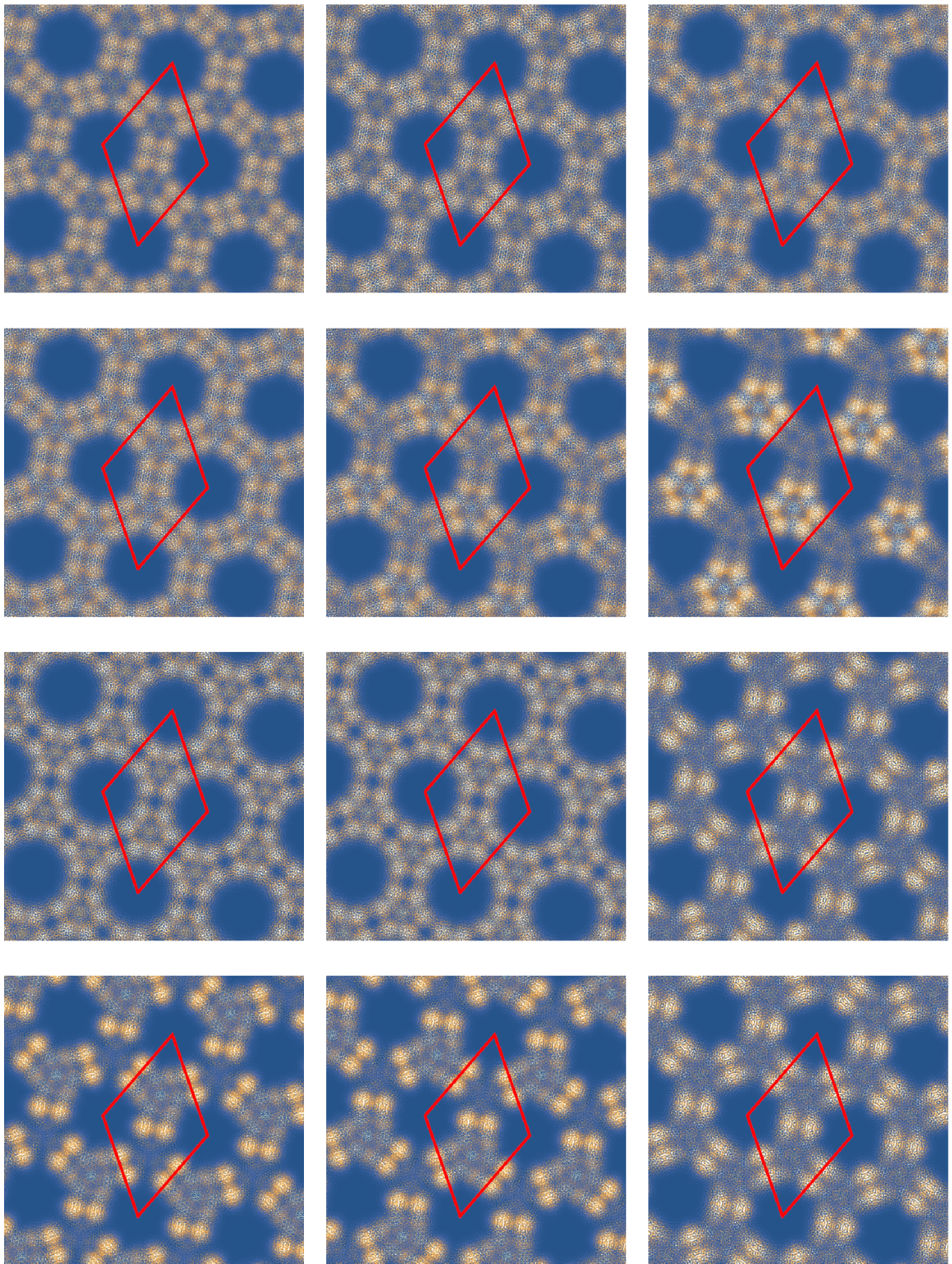


Figure 3.21: Continued (repeated from page 63)

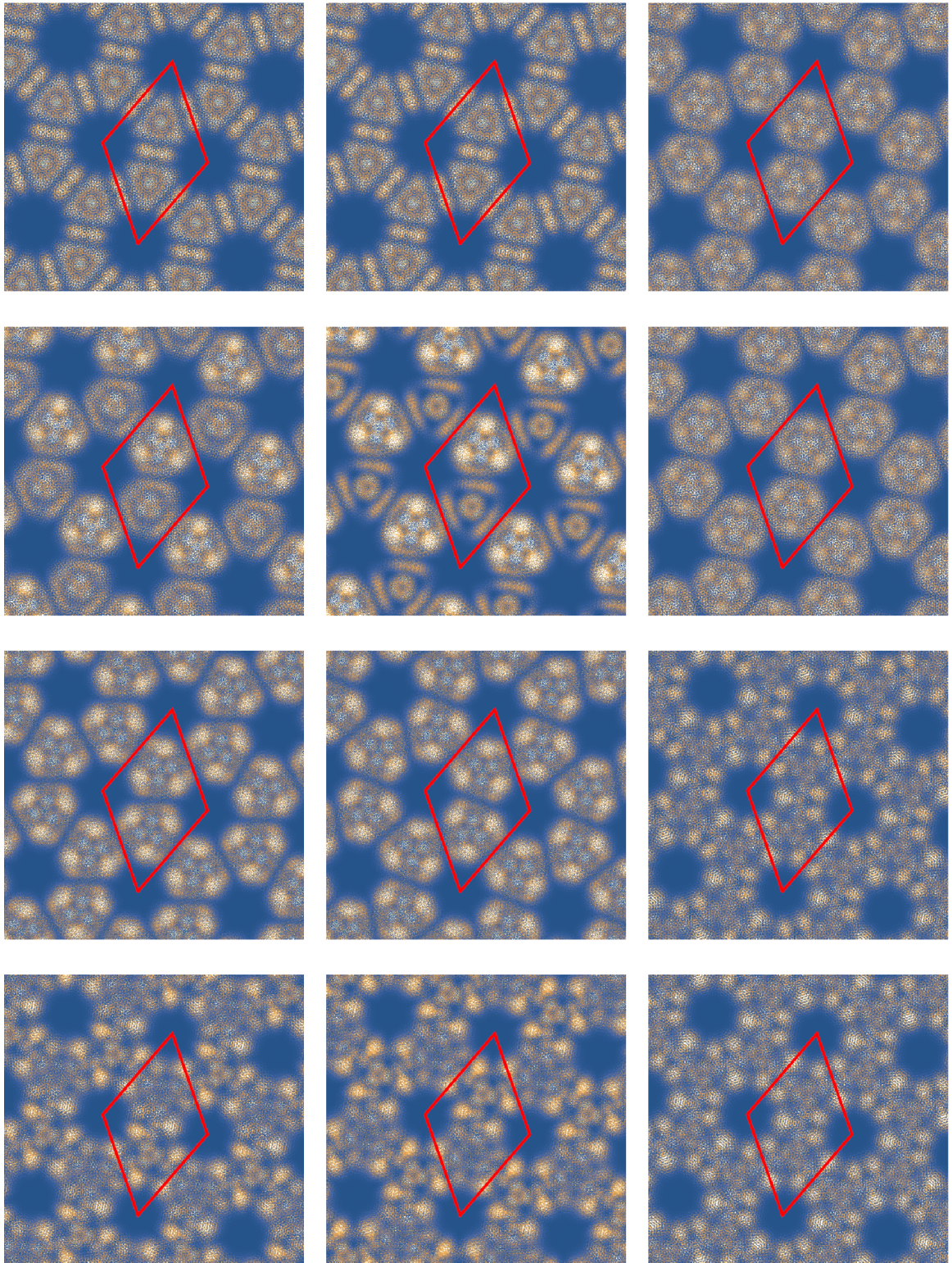


Figure 3.21: Continued (repeated from page 63)

CHAPTER 4

PEIERLS TRANSITION NEAR 0°

We now turn to the possibility of a Peierls transition in bilayer graphene. In this chapter, we will review the theory of Peierls transitions and then examine the case of a bilayer near 0° [33]. In the next chapter, we will turn to the near 38.2° case.

4.1 Peierls Transition Theory

The Peierls transition describes the spontaneous distortion of a lattice at low temperature. In particular, Peierls realized that one dimensional chains are unstable because there exist phonon distortions that lower the valence band energy more than they increase the lattice elastic energy. The basic outline of the argument is simple. Consider a one dimensional atomic chain. If all atoms are equally spaced, the electronic dispersion is a simple cosine:

$$E(k) = 2t \cos k \quad k \in [0, 2\pi). \quad (4.1)$$

Recasting the same problem with a two atom basis, we can fold the previous bands to find:

$$E(k) = \pm 2t \cos k/2 \quad k \in [0, 2\pi). \quad (4.2)$$

It is now possible to open a gap at the degenerate point $k = \pi$ with the addition of a phonon. In real space, this corresponds to a distortion of the lattice, breaking the sublattice symmetry and causing the chain to transition from a conductor to an insulator. Suppose the phonon opens a gap of size m that we will refer to as mass. If we are at half filling, the filled electron states will be pushed down in energy by the gap opening. The total energy

per unit length gained by pushing the states down is:

$$U_{\text{elec}} = 2 \frac{1}{2\pi} \int_0^{k_f} \left(\sqrt{v^2 k^2 + m^2} - vk \right) dk = \frac{m^2}{4v} \left(1 - \log \frac{m}{4vk_f} \right) + \mathcal{O} \left[\left(\frac{m}{vk_f} \right)^3 \right]. \quad (4.3)$$

The upper limit k_f is any momentum sufficiently large to capture all the downward shift. The mass is related to the amplitude of the phonon, u_0 , by:

$$m \propto \frac{u_0}{a} t, \quad (4.4)$$

where a is the lattice constant. This is because if an atom shifts by a , the energy change will be order t . In general, the elastic energy cost per unit length is:

$$U_{\text{elas}} \propto \left(\frac{u_0}{a} \right)^2 \frac{t}{a}. \quad (4.5)$$

This is because the cost of shifting an atom by a , is the in-layer coupling t . We square u_0/a because we expect a quadratic dependence for a harmonic potential. We divide by a to get the energy per unit length.

Because U_{elas} goes as u_0^2 and U_{elec} has a term that goes as $-u_0^2 \log u_0$, there always exists a u_0 small enough that the electronic energy gain is greater than the elastic energy cost. The inevitable conclusion is that if any linear atomic chain is cooled sufficiently, it will spontaneously distort and become an insulator. Note that this is a scaling argument. While we know a critical temperature for a metal-insulator transition exists, we must calculate the appropriate prefactors to determine if it is attainable in experiments.

The classic Peierls argument will not work for a single layer of graphene. The key to the argument is the logarithmic divergence of the electronic energy gain in m . This, in turn, rests critically on the dimensionality of the system. For instance, the argument would fail



Figure 4.1: Schematic of two Dirac cones shifted by opposite V_0 . On the left, the cones do not interact. On the right, they interact with a mass gap along the Dirac circle.

for the Dirac point of graphene. In that case, the integral is:

$$U_{\text{elec}} = 2\pi \frac{1}{4\pi^2} \int_0^{k_f} k \left(\sqrt{v^2 k^2 + m^2} - vk \right) dk, \quad (4.6)$$

which has a lowest order term proportional to m^2 . Although a phonon may open a gap, the energy gained will not in general compensate for the cost of the distortion. There have been proposals to circumvent this problem. For instance, out of plane phonons restore the one dimensional nature of the problem, leading to a Peierls distortion [34]. In addition, one could consider complex nesting vectors that couple more states and also lead to a Peierls distortion [35]. Here we try a different approach.

4.2 Analytic Framework

The basis for our first approach is to use bilayer graphene under a perpendicular electric field. This restores the one dimensional nature of the Peierls integral because the Dirac point becomes a Dirac line. Thus, we will also restore the scaling argument that guarantees a Peierls transition.

Consider a sample of bilayer graphene in the perturbative regime near 0° . We now apply a bias, $V_0 \ll t$. Neglecting interlayer coupling, we have a doubly degenerate Dirac circle around each Dirac point. To find a Peierls transition, we introduce a distortion, $\mathbf{u}(\mathbf{r})$ over the sample that opens a gap of mass m over this Dirac circle. A schematic cross section is shown in Figure 4.1.

In order for the distortion to be energetically favorable, the energy gained by the valence

band per unit area, U_{elec} , must be greater than the elastic energy gained by the lattice per unit area, U_{elas} . Assuming we have a mass gap, m , we can derive the energy gained by the valence band per unit area:

$$U_{\text{elec}} = \frac{V_0}{v\pi} \int_0^{k_f} \left(\sqrt{v^2 k^2 + m^2} - vk \right) dk, \quad (4.7)$$

where we have introduced a momentum cut-off k_f , such that $vk_f \ll V_0$.

$$U_{\text{elec}} = \frac{V_0 m^2}{4\pi v^2} \left(1 + 2 \log \frac{2vk_f}{m} \right) + \mathcal{O} \left[\left(\frac{m}{vk_f} \right)^3 \right], \quad (4.8)$$

where we have integrated and then expanded in the limit, $m \ll vk_f$. We have recovered the logarithmic dependence by using the bias to restore the one dimensional character of the problem. This logarithmic divergence will make the Peierls transition possible once again.

The phonon that created the mass gap will have some amplitude, u_0 . We anticipate that the mass will be proportional to u_0 and the elastic energy will be proportional to u_0^2 . Therefore, the total elastic energy cost will be proportional to m^2 . Just as in the one dimensional case, we are guaranteed a Peierls transition for a sufficiently small m . The only question is the temperature at which this transition will occur.

4.3 Mass Term

In choosing a phonon, we must consider two factors. First, the phonon should induce a large mass all the way around the Dirac circle. Second, the phonon should have a low elastic energy cost. Consider a phonon of the form:

$$\mathbf{u}(\mathbf{r}) = \frac{u_0}{K} \sum_{n=1}^3 \mathbf{K}_{1v}^n \sin(\delta \mathbf{K}_n \mathbf{r} - 2\pi n/3), \quad (4.9)$$

where \mathbf{K}_{lv}^n are the three shortest length equivalent Dirac points of layer l and $\delta \mathbf{K}_n = \mathbf{K}_{2v}^n - \mathbf{K}_{1v}^n$. Note, for v we may choose either valley. Also, K is the norm of any of the

bmK_{lv}^n . The calculation will be the same. We will apply this phonon to the second layer. This phonon is a good choice because it induces a large coupling between K_{1v} and K_{2v} . Therefore, one can hope it will open a mass gap. In addition, it uses the long wavelength δK_n to accomplish this coupling. We show the real space vector field of this phonon in Figure 4.2. The red lines indicate the supercell of a near zero degree system.

Now we derive the mass gap from the phonon. We will perform perturbation theory using the coupling induced between single layer states by the phonon. First, we divide this effect into two parts, H_{\parallel}^u and H_{\perp}^u . H_{\parallel}^u describes the coupling through the phonon between states in the same layer. H_{\perp}^u describes coupling through the phonon between states in opposite layers. We now estimate the size of both effects to show we may neglect H_{\parallel}^u .

We expect the phonon to couple states that differ in momentum by δK_n . The states at the Dirac points of layer one differ in momentum by exactly δK_n from the states at the Dirac points of layer two. Therefore, the phonon induces direct coupling between these states. The perturbative correction is of order $u_0\tilde{\gamma}_0/a$.

For states in the same layer, the coupling is second order. In other words, a state at the Dirac point couples to a higher energy state and back to itself. The size of the coupling is of order $(\nabla t_{\parallel}\delta u_0\delta K)^2/v\delta K$. Here ∇t_{\parallel} is the gradient of the nearest neighbor hopping energy and δ is the interatomic distance. We may neglect H_{\parallel}^u in the regime where:

$$\frac{u_0}{a} \ll \frac{\tilde{\gamma}_0}{v\delta K} = \alpha \ll 1. \quad (4.10)$$

That we are truly in this regime will be verified below. However, it makes sense. The system size, and thus α , is a parameter we will choose to be as large as possible while still being much less than one. In addition, we expect u_0 , the phonon amplitude that results in a Peierls transition to be very small. We will see that it is small enough to satisfy this regime.

Now we derive the exact form of the interlayer perturbation. In second quantization,

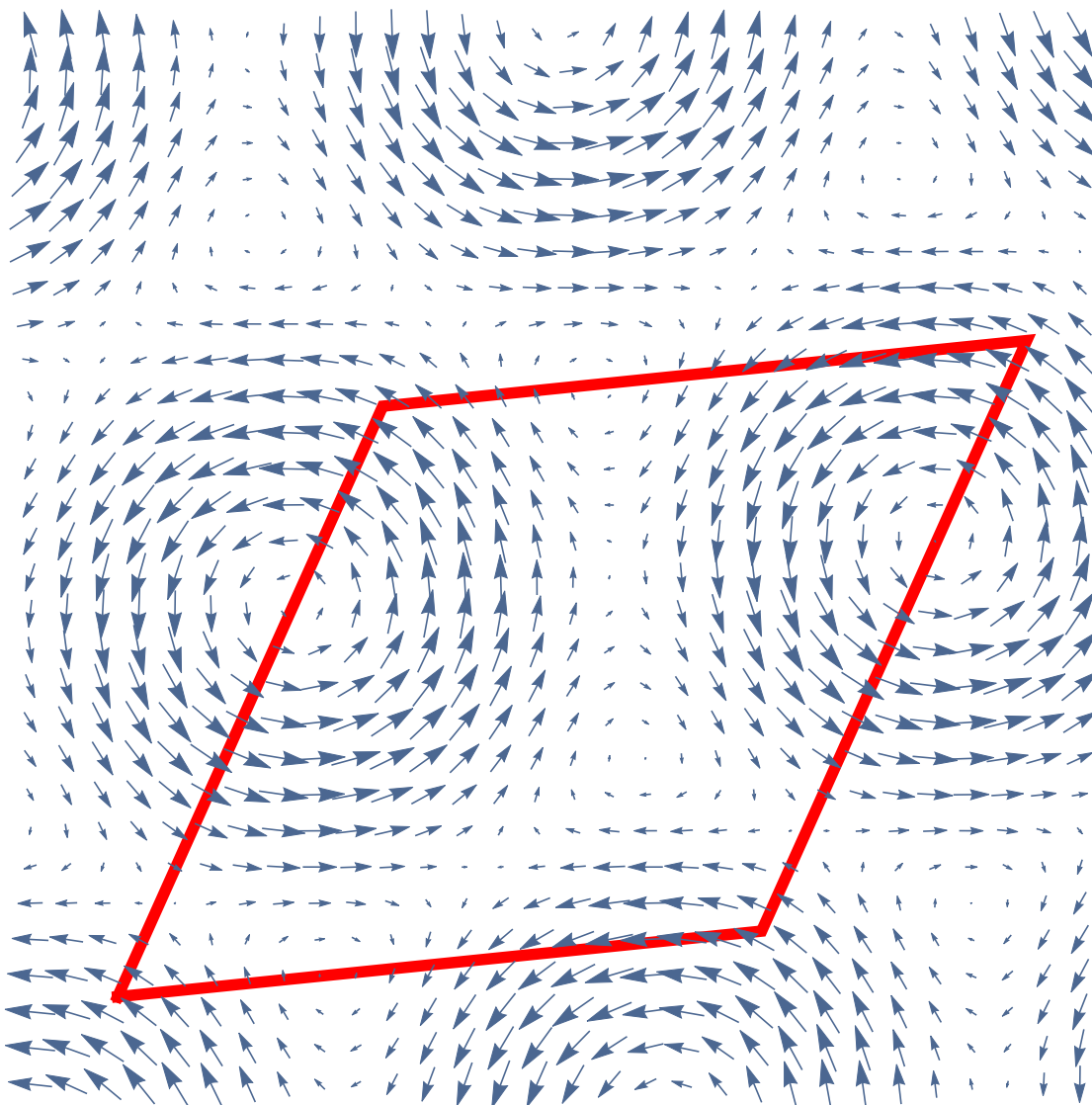


Figure 4.2: Phonon for a system at 11.6° .

the interlayer part of the Hamiltonian is now written:

$$H_{\perp} = \sum_{ij\sigma\sigma'} a_{1i\sigma}^{\dagger} a_{2j\sigma'} f(\mathbf{R}_{1i\sigma} - \mathbf{R}_{2j\sigma'}^u), \quad (4.11)$$

where $\mathbf{R}_{2j\sigma}^u = \mathbf{R}_{2j\sigma} + \mathbf{u}(\mathbf{R}_{2j\sigma})$ denotes position of the atom of layer 2, site j , and sublattice σ with the addition of the phonon distortion. Note, we are only distorting layer 2. For the lattice creation and annihilation operators, we substitute the Fourier transform:

$$a_{li\sigma} = \frac{1}{\sqrt{N}} \sum_k a_{lk\sigma} e^{-i\mathbf{k}\mathbf{R}_{li\sigma}}. \quad (4.12)$$

We find:

$$H_{\perp} = \sum_{ij\sigma\sigma'kk'q} a_{1k\sigma}^{\dagger} a_{2k'\sigma'} \tilde{f}(\mathbf{q}) e^{-i\mathbf{q}(\mathbf{R}_{1i\sigma} - \mathbf{R}_{2j\sigma'}^u)} e^{i\mathbf{k}\mathbf{R}_{1i\sigma}} e^{-i\mathbf{k}'\mathbf{R}_{2j\sigma'}}. \quad (4.13)$$

Assuming $q\mathbf{u} \ll 1$, we can treat the phonon as small. The lowest order term is the interlayer coupling without any phonon distortion. The first order correction due to the phonon is:

$$H_{\perp}^u = \sum_{ij\sigma\sigma'kk'q} a_{1k\sigma}^{\dagger} a_{2k'\sigma'} \tilde{f}(\mathbf{q}) e^{i(\mathbf{k}-\mathbf{q})\mathbf{R}_{1i\sigma}} e^{-i(\mathbf{k}'-\mathbf{q})\mathbf{R}_{2j\sigma'}} [q\mathbf{u}(\mathbf{R}_{2j\sigma'})]. \quad (4.14)$$

The sin in the form of the phonon is composed of a positive and a negative exponential:

$$\mathbf{u}(\mathbf{r}) = \frac{u_0}{2iK} \sum_{n=1}^3 \mathbf{K}_{1v}^n [e^{i(\delta\mathbf{K}_n\mathbf{r} - 2\pi n/3)} - e^{-i(\delta\mathbf{K}_n\mathbf{r} - 2\pi n/3)}]. \quad (4.15)$$

We break H_{\perp} into the sum of two terms, $H_{\perp}^{u,+}$ and $H_{\perp}^{u,-}$. $H_{\perp}^{u,+}$ includes the positive exponential of the phonon and $H_{\perp}^{u,-}$ includes the negative exponential of the phonon. Let

us examine the coupling from positive exponential, $H_{\perp}^{u,+}$. We find:

$$H_{\perp}^{u,+} = \frac{u_0}{2K} \sum_{ij\sigma\sigma'kk'qn} a_{1k\sigma}^{\dagger} a_{2k'\sigma'} \tilde{f}(\mathbf{q}) e^{i(\mathbf{k}-\mathbf{q})\mathbf{R}_{1i\sigma}} e^{-i(\mathbf{k}'-\mathbf{q})\mathbf{R}_{2j\sigma'}} (\mathbf{q}\mathbf{K}_{1v}^n) e^{i\delta\mathbf{K}_n\mathbf{R}_{2j\sigma'}} e^{-i2\pi/3}. \quad (4.16)$$

Now, we separate out the dependence on sublattice:

$$H_{\perp}^{u,+} = \frac{u_0}{2K} \sum_{\sigma\sigma'kk'qn} a_{1k\sigma}^{\dagger} a_{2k'\sigma'} \tilde{f}(\mathbf{q}) e^{i(\mathbf{k}-\mathbf{q})\delta_{1\sigma}} e^{-i(\mathbf{k}'-\delta\mathbf{K}_n-\mathbf{q})\delta_{2\sigma'}} \sum_{ij} e^{i(\mathbf{k}-\mathbf{q})\mathbf{R}_{1i}} e^{-i(\mathbf{k}'-\delta\mathbf{K}_n-\mathbf{q})\mathbf{R}_{2j}} (\mathbf{q}\mathbf{K}_{1v}^n) e^{-i2\pi/3}. \quad (4.17)$$

Now, we perform the lattice sums to arrive at the following conditions in momentum space:

$$\mathbf{k} + \mathbf{G}_1 = \mathbf{k}' - \delta\mathbf{K}_n + \mathbf{G}_2 = \mathbf{q}. \quad (4.18)$$

Given that $\mathbf{k}' - \delta\mathbf{K}_n = \mathbf{k}$, we have the exact same condition as for the direct coupling of a 0° commensuration (See Equation 2.12). Recall, the set of all $(\mathbf{G}_1, \mathbf{G}_2)$ satisfying this equation was defined to be \mathcal{G}_0 . This set is partitioned into subsets of equal coupling strength, and we only keep the set of strongest coupling, \mathcal{G}_0^1 . There are three solutions in \mathcal{G}_0^1 , which we label $(\mathbf{G}_1^n, \mathbf{G}_2^n)$. For each n , $(\mathbf{G}_1^n, \mathbf{G}_2^n)$ satisfies Equation 4.18, for that specific $\delta\mathbf{K}_n$.

The term involving the negative exponential, $H_{\perp}^{u,-}$, will satisfy the equation:

$$\mathbf{k} + \mathbf{G}_1 = \mathbf{k}' + \delta\mathbf{K}_n + \mathbf{G}_2 = \mathbf{q}. \quad (4.19)$$

In this case, there is no direct coupling because there are no \mathbf{G} vector solutions. Therefore, we neglect the term $H_{\perp}^{u,-}$ and set $H_{\perp}^u = H_{\perp}^{u,+}$.

Substituting the solutions to Equation 4.18 into H_{\perp}^+ , we find that $\mathbf{q} = \mathbf{K}_{1v}^n$. We arrive at a simple sum over n :

$$H_{\perp}^+ = \frac{u_0 \tilde{\gamma}_0}{2} K \sum_n e^{i\mathbf{G}_1^n \delta_{1\sigma}} e^{-i\mathbf{G}_2^n \delta_{2\sigma'}} e^{-i2\pi n/3}. \quad (4.20)$$

Without the extra phase factor, this would clearly result in the coupling term $3u_0 \tilde{\gamma}_0 K \sigma_0 \tau_0 l_x / 2$. That is, the coupling induced by the phonon is identical to the interlayer coupling of an AA stacked bilayer, scaled by the prefactor, $u_0 K / 2$. If we include the extra phase, the sum results in an odd commensuration effect of the same size. This results in an effective AB stacked bilayer with scaled coupling. We wish to open an gap under bias. Therefore, we clearly want the effective AB coupling, that is the phonon with added phase.

Upon application of the bias, the gap induced around the Dirac circle will be:

$$\Delta = 2m = \frac{2u_0 \tilde{\gamma}_0 K}{2} = \frac{2\pi u_0 \tilde{\gamma}_0}{a}. \quad (4.21)$$

Note the result is independent of the bias voltage, V_0 . This is expected, just as the gap in an AB bilayer under bias is independent of V_0 for large bias. In other words, as V_0 increases, the gap saturates. After the saturation point at $V_0 = \tilde{\gamma}_0$, V_0 controls the radius of the Dirac circle, while $\tilde{\gamma}_0$ controls the size of the gap.

We verify this result by performing a tight binding calculation. We take a system at 11.6° with coupling $f(r) = \gamma \exp(-r^2/l_r^2) \Theta(l_0 - r)$, where $l_r = 2\delta$ and $l_0 = 6\delta$. In Figure 4.3 we see the gap plotted against the amplitude of the phonon. The solid line shows the theoretical prediction is in good agreement for small amplitude.

4.4 Peierls Transition

With the mass term in hand, we can derive the prefactors necessary to find the critical temperature for a Peierls transition. First, we obtain the total electronic energy gained by

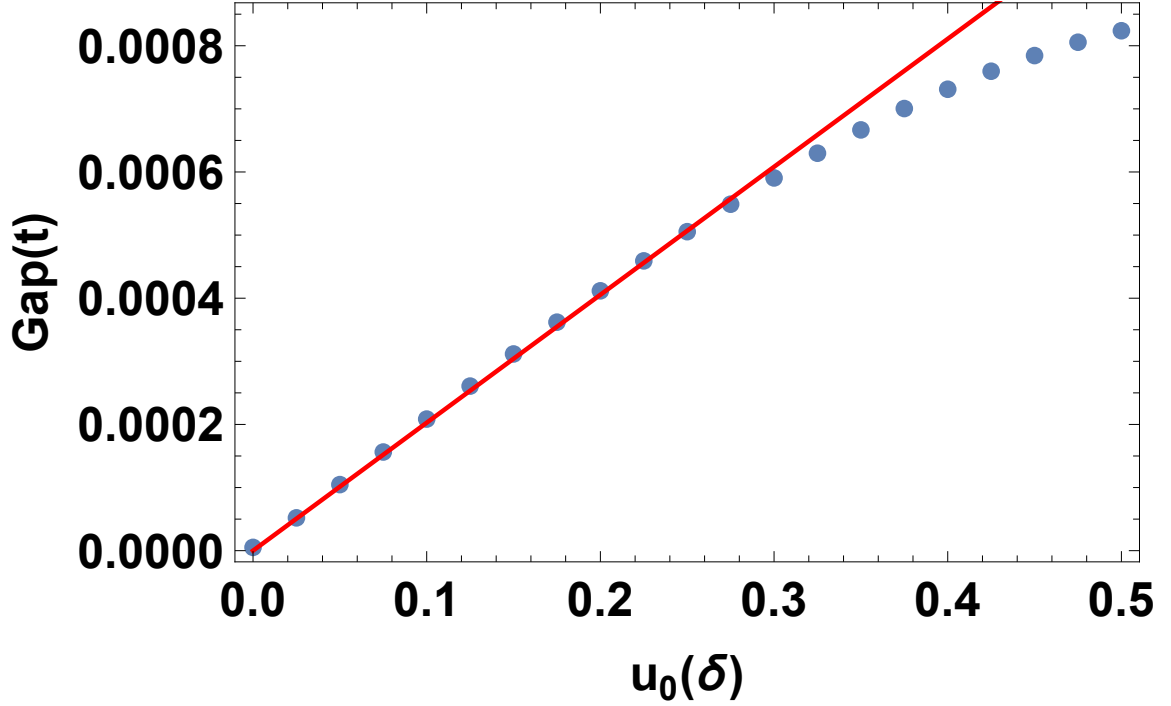


Figure 4.3: Gap induced by the phonon for a system at 11.6° . The solid line is the prediction derived in the text.

opening the mass gap. This is simply Equation 4.7 with the derived mass:

$$U_{\text{elec}} = 4 \frac{\tilde{\gamma}_0^2 \pi u_0^2 V_0}{a^2 v^2} \left(1 + 2 \log \frac{avk_f}{\tilde{\gamma}_0 \pi u_0} \right), \quad (4.22)$$

where the extra factor of four in front is for spin and valley degeneracy. Note both valleys are affected because we include both $\pm \delta \mathbf{K}$ in the phonon. Next, we obtain the elastic energy cost of this phonon per unit area. We use a continuum approximation. The elastic energy density for a single sheet of graphene is [36]:

$$\mathcal{U}_{\text{elas}} = \frac{\lambda_L}{2} (\partial_x u_x + \partial_y u_y)^2 + \mu_L \left[(\partial_x u_x)^2 + (\partial_y u_y)^2 + \frac{1}{2} (\partial_x u_x + \partial_y u_y)^2 \right], \quad (4.23)$$

where μ_L and λ_L are Lamé parameters. Since we are applying the phonon only to the top layer, we calculate the elastic energy density for a single layer of graphene. For

simplicity, we neglect the interlayer elastic energy cost. This is a competing effect that could also be investigated in future work.

To find the total elastic energy cost per unit area we calculate:

$$U_{\text{elas}} = \frac{1}{A} \int_{\text{supercell}} \mathcal{U}_{\text{elas}}. \quad (4.24)$$

For this specific phonon, we find:

$$U_{\text{elas}} = \frac{8\pi^2 u_0^2 [\lambda_L + 3\mu_L - (\lambda_L + \mu_L) \cos \theta]}{3a^2} (\sin \theta/2)^2 = \frac{4\pi^2 \mu_L}{3a^2} u_0^2 \theta^2 + \mathcal{O}(\theta^3), \quad (4.25)$$

where the second equality takes the lowest order term in θ . A Peierls transition will occur when $U_{\text{elec}} = U_{\text{elas}}$. Equating our expressions and solving for u_0 , we find:

$$u_0 = \frac{a\sqrt{e}k_f v}{\tilde{\gamma}_0 \pi} e^{-\mu_L \pi v^2 \theta^2 / 6\tilde{\gamma}_0^2 V_0} = \frac{a\sqrt{e}k_f v}{\tilde{\gamma}_0 \pi} e^{-3a^2 \mu_L / 32\pi V_0 \alpha^2}, \quad (4.26)$$

where in the second equality $\alpha = \tilde{\gamma}_0 / v\delta K$ must be small to stay within the perturbative regime of the interlayer coupling. The only experimental degrees of freedom are θ , which is buried in α , and V_0 . However, because α must remain small (equivalently, θ must remain large), we see immediately the exponential is extremely unfavorable.

We find the gap is:

$$\Delta = 2\sqrt{e}k_f v e^{-3a^2 \mu_L / 32\pi V_0 \alpha^2}. \quad (4.27)$$

If we use the values in Appendix A, and set $V_0 = t/2$ and $\alpha = 1/10$, we find a gap that corresponds to an energy of $1.5 \times 10^{-55} \text{K}$. This is far too small for observability in any reasonable experiment. The crux of the problem is the α^2 in the denominator being massively amplified by the exponential. Should we allow α to increase, we will enter the non-perturbative regime, which is beyond what this theory can handle. In the next chapter,

we turn to a non-perturbative regime where an analytic theory is possible.

CHAPTER 5

NON-PERTURBATIVE PEIERLS TRANSITION

In Chapter 4, we sought a Peierls transition using a bias to transform the graphene Fermi surface into a one dimensional object. While this argument is sound and a Peierls transition exists, the critical temperature is too low for observation. We now turn to the non-perturbative regime for a new idea [33].

We saw in Chapter 3 that a bilayer very close to commensuration produces a network of topologically protected states. The low energy electronic structure of this network includes a flat band. The system has a high density of states at the energy level of the flat band. Therefore, it will be highly susceptible to spontaneous symmetry breaking and distortion of the band, such as the one shown in Figure 5.1. If we partially fill the flat band, a distortion will lower the total electronic energy. This energy gain has the potential to be very large because the distortion will occur over the entire Brillouin Zone. Thus, we have a strong possibility for a Peierls transition at a reasonable temperature.

5.1 Scaling Argument

Without calculation, the standard Peierls transition argument guarantees a transition because it is a scaling argument. The appearance of a logarithmic term guarantees a critical

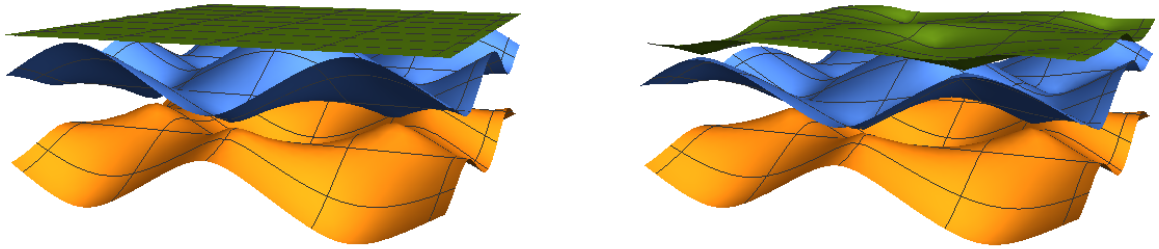


Figure 5.1: Schematic of near 38.2° with (right) and without (left) added phase on the links. The flat band undergoes a distortion.

temperature. We present a similar scaling argument for our new idea.

The first question is the mechanism by which a phonon will induce a flat band distortion. Recall the physics of the topologically protected midgap states in the network. These states originate from two Dirac cones displaced from the Dirac point of the bilayer. In Figure 5.2, we see these Dirac cones as we traverse between two nodes. Each midgap state will inherit the momentum of its respective Dirac cone as it traverses the link. The integral of its momentum along the link is the total phase picked up by a mode as it traverses the link.

The addition of a phonon will change the local stacking order of the bilayer, changing the local band structure and shifting the Dirac cones. This in turn will change the phase picked up by the midgap states. In Figure 5.1, we see the effect of adding different extra phases on different links within the network model. The flat band becomes distorted, as required.

We now present rough estimates of the electronic energy gain and elastic energy cost. Given a phonon that induces an extra phase of $\delta\psi$, we expect the electronic energy gain per unit area, U_{elec} , to have a linear term in $\delta\psi$. The maximum bandwidth is v/L , where L is the length of a link in the network model. We expect a generic band to have width of that order. The number of states per unit area is $1/A$. Thus, the total energy gain per unit area is:

$$U_{\text{elec}} \propto \frac{v}{LA} \delta\psi. \quad (5.1)$$

The distorting phonon couples through the interlayer coupling, which has strength $\tilde{\gamma}_{38}$. A distortion of order a completely changes the local lattice stacking, changing the energy by order $\tilde{\gamma}_{38}$. Integrated along the link, a change in energy will change the accumulated phase by a factor of L/v . Therefore, we expect $\delta\psi \propto \tilde{\gamma}_{38} u_0 L / av$. Thus,

$$U_{\text{elec}} \propto \frac{\tilde{\gamma}_{38} u_0}{Aa}. \quad (5.2)$$

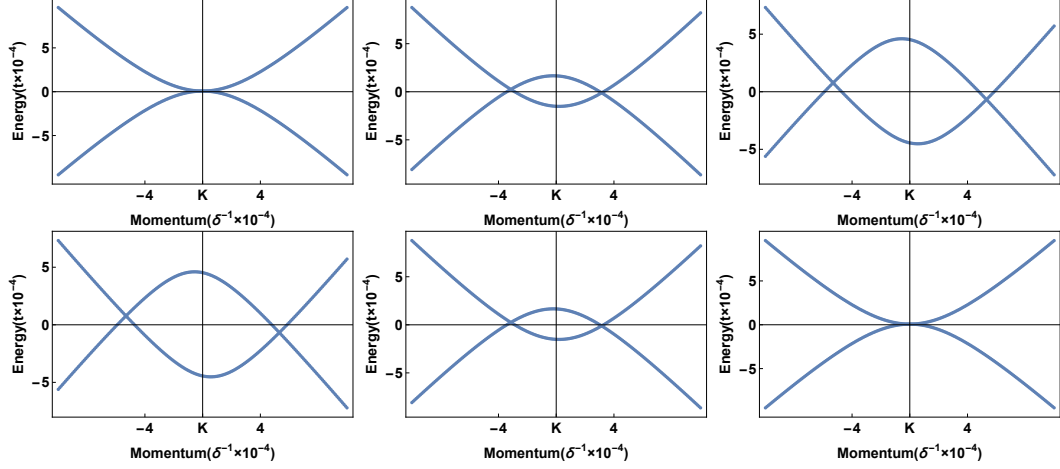


Figure 5.2: Local band structure along the line of degeneracy. Top left is one node and bottom right is the other node.

We can also estimate the elastic energy cost per unit area of the distorting phonon, U_{elas} . A distortion of order a completely separates neighboring sites, resulting in an energy cost of t . Thus, the energy cost per atom is of order $(u_0/a)^2 t$. We introduce the square because we expect elastic energy to follow a harmonic potential in u_0 . To get the elastic energy cost per unit area, we divide by the area associated with one atom a^2 . Therefore, we find:

$$U_{\text{elas}} \propto \left(\frac{u_0}{a}\right)^2 \frac{t}{a^2}. \quad (5.3)$$

We see that U_{elec} is linear in u_0 , while U_{elas} is quadratic in u_0 . Therefore, we are guaranteed a Peierls transition at small enough u_0 , and there must be a critical temperature for this transition. In addition, we no longer rely on the logarithm of the original Peierls argument. Therefore, we will no longer have the unfavorable exponential in transition temperature. We now turn to calculating the prefactors that will allow us to estimate this critical temperature.

5.2 Effective Model

The effective model for a bilayer near 38.2° is built on topologically protected midgap states scattering between SE odd nodes. The symmetries of the bilayer guarantee there is

only one free parameter. However, we may break these symmetries with a lattice distortion, introducing new parameters that distort the energy bands. If the energy gain from such a distortion exceeds the elastic energy cost, we expect a Peierls transition.

5.2.1 Added Phase

The phonon changes the local lattice stacking, and thus the effective low energy Hamiltonian throughout the supercell. This results in an extra phase picked up by modes traveling through the distorted region. Consider a mode traveling along an edge i between the nodes of our network. The mode that travels this path is a midgap state of the Dirac cone arising from the local effective Hamiltonian. As it travels between network nodes it acquires a phase $\exp(i\psi_i)$, where:

$$\psi_i = \int_{\text{Link}_i} \mathbf{k}_{\text{disp}}(\mathbf{r}) d\mathbf{r} \quad (5.4)$$

and $\mathbf{k}_{\text{disp}}(\mathbf{r})$ is the displacement of the midgap state in momentum space relative to the Dirac point. In other words, we integrate the momentum displacement of the midgap states along the link. The momentum displacement $\mathbf{k}_{\text{disp}}(\mathbf{r})$ depends on the local lattice stacking as we move through the supercell.

Our analysis of the twist-induced gauge fields describes how the momentum of the mode varies in the superlattice. In general, it depends on all four gauge fields. However, recall that momentum displacement of the pseudo-valleys is primarily provided by \mathbf{A}_x , \mathbf{A}_y , and \mathbf{A}_z . The primary effect of \mathbf{A}_0 is to shift the psuedovalleys in energy. For simplicity, we may neglect it because its effect is small compared to the other fields. In Figure 5.3, we see the comparative effect of \mathbf{A}_0 . We plot the momentum of zero energy states along the link connection SE odd nodes. The blue line shows this momentum with \mathbf{A}_0 included, and the yellow line shows this momentum with \mathbf{A}_0 excluded.

We derived the expression for $\mathbf{k}_{\text{disp}}(\mathbf{r})$ in this case in Equation 3.18, where we used the

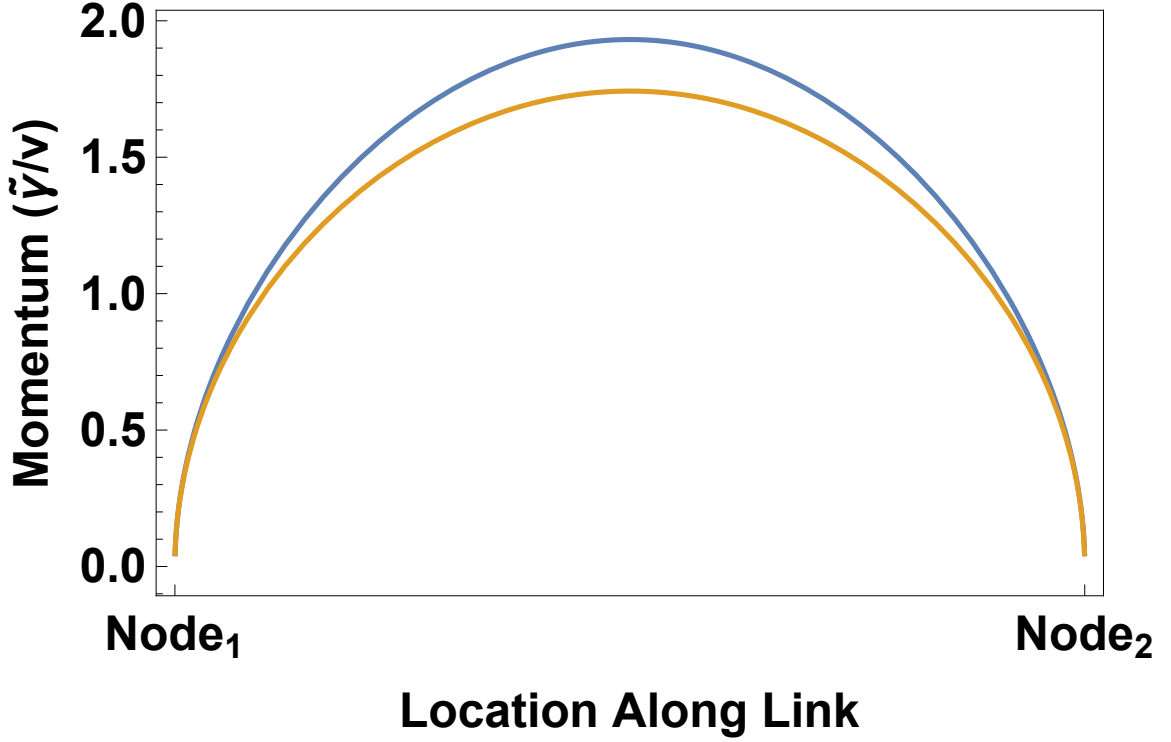


Figure 5.3: Momentum of a zero energy state with (blue) and without (yellow) A_0 .

polar coordinates k and ϕ .

The angle ϕ is constant along the entire link. In other words, the pseudo-valleys displace along a straight line in momentum space. In addition, the direction of the link is also constant. Therefore, we can rewrite the accumulated phase:

$$\psi_i = \cos w \int_{\text{Link}_i} k_{\text{disp}}(r) dr, \quad (5.5)$$

where w is the angular difference, from Equation 3.18, between the direction of the link and the pseudo-valley displacement in momentum space. A careful calculation reveals that $w = 0$ for all i . In other words, the displacement of the pseudo-valleys is parallel to the direction of the links. Therefore, we may set $\cos w = 1$ in what follows.

To calculate the integral, we parametrize k_{disp} along the path of the link. Let $\mathbf{r} = t_1 \mathbf{T}_1 + t_2 \mathbf{T}_2$ where \mathbf{T}_i are the supercell unit vectors. The link is parametrized by the path $t_1 = t_2 = s$ for $s \in [1/3, 2/3]$. By simplifying the gauge fields along this line, we find:

$$\begin{aligned}
k_{\text{disp}}(s) &= \frac{1}{v} \sqrt{||A_x^2 + A_y^2 + A_z^2||} \\
&= \frac{\tilde{\gamma}_{38}}{2\sqrt{7}v} \sqrt{2 \cos 4\pi s - 164 \cos 2\pi s - 81} \quad s \in [1/3, 2/3]. \quad (5.6)
\end{aligned}$$

The phase picked up by the mode is then the line integral of k_{disp} along the edge it is traversing. For instance, if there is no distortion, we find the accumulated phase:

$$\psi = \int_{\text{Link}} k_{\text{disp}}(r) dr = \int_{1/3}^{2/3} k_{\text{disp}}(s) \frac{dr}{ds} ds = \frac{3L\tilde{\gamma}_{38}}{2\sqrt{7}v} \int_{1/3}^{2/3} \sqrt{2 \cos 4\pi s - 164 \cos 2\pi s - 81} ds, \quad (5.7)$$

where we must calculate the integral numerically. We find $\psi = 1.35L\tilde{\gamma}_{38}/v$.

5.2.2 Distorted Flat Band

In the network model, there are three links, and thus, three phase parameters ψ_i . The added phases enter the network model through the transfer matrix, M , of Equations 3.31:

$$M = \begin{pmatrix} 0 & 0 & 0 & 0 & 0 & e^{i\psi_1} e^{-i2\pi k_1} \\ 0 & 0 & 0 & 0 & e^{i\psi_2} e^{-i2\pi k_2} & 0 \\ 0 & 0 & 0 & e^{i\psi_3} & 0 & 0 \\ 0 & 0 & e^{i\psi_3} & 0 & 0 & 0 \\ 0 & e^{i\psi_2} e^{i2\pi k_2} & 0 & 0 & 0 & 0 \\ e^{i\psi_1} e^{i2\pi k_1} & 0 & 0 & 0 & 0 & 0 \end{pmatrix}. \quad (5.8)$$

Without a phonon, all ψ_i are equal, and we may ignore them because they correspond to a rigid shift in all bands. However, the addition of different phases to different links distorts the flat band. We call the added phase on link i , $\delta\psi_i$. For instance, suppose we add a phase to two of the links: $\delta\psi_1 = -\delta\psi_2$. That is, a mode traversing link one picks up an

extra phase $\delta\psi_1$ and a mode traversing link two picks up an extra equal and opposite phase. The effect on the band structure is shown in Figure 5.4.

Semiclassically, a change of the sum of phases, $\sum \delta\psi_i$, shifts the chemical potential of the network modes, changing the electron number. However, in an experiment, an additional electric potential will build to maintain charge neutrality. Thus, we must maintain $\sum \delta\psi_i = 0$ in the calculation. Given this constraint, the flat band will distort without an overall shift in energy. Thus, if we partially fill the flat band, we expect a significant energy gain from this distortion. To calculate this energy gain, we set the chemical potential, μ , to the energy of the undistorted flat band and assume the flat band is half-filled. The band distorts symmetrically, and thus, the energy gain per unit area is due to all states that move below μ .

$$U_{\text{el}} = \frac{v}{L4\pi^2} \int_{\epsilon' < \mu} (\epsilon' - \epsilon) d^2k, \quad (5.9)$$

where ϵ and ϵ' are the logarithm of the eigenvalues of the network model in Equation 3.27 without and with distortion, and L is the length of an edge. The integral must be calculated numerically. For small added phase we keep the linear term:

$$U_{\text{elec}} = \frac{v}{LA} \xi \delta\psi_1 + \mathcal{O}(\delta\psi_1^2), \quad (5.10)$$

where A is the area of the supercell.

The dimensionless parameter ξ will be different depending on how phase is distributed among the links. We will seek a phonon that adds phase to the links and then calculate ξ numerically in each case.

5.3 In-Plane Phonon

We now examine the possibilities for a Peierls transition due to an in-plane distortion of one of the graphene layers.

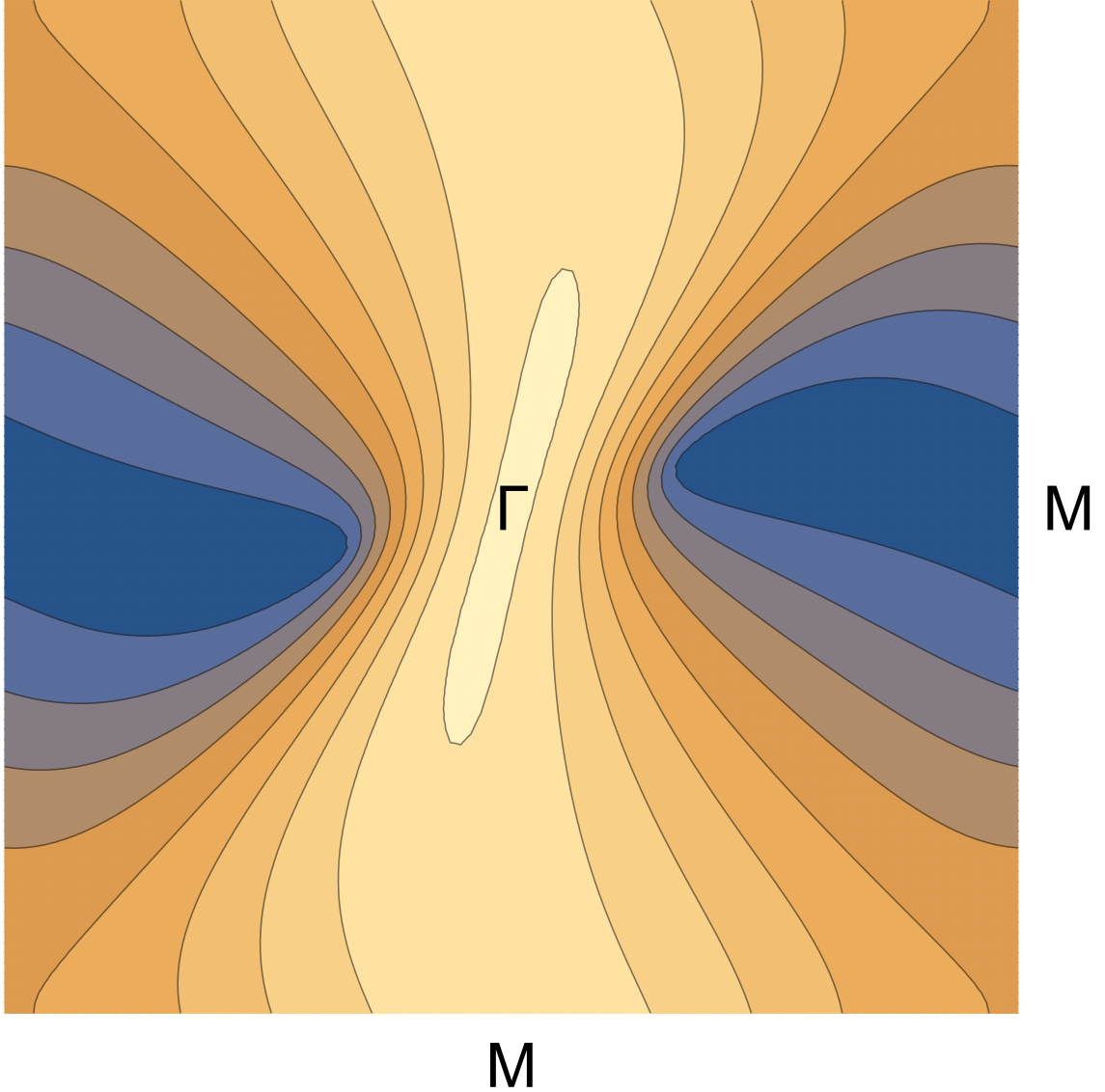


Figure 5.4: Distortion of flat band predicted by the network model when $\delta\psi_1 = -\delta\psi_2 = .2$ and $\delta\psi_1 = 0$. We use $\lambda = 1.3$. Note axes are not orthogonal.

5.3.1 Electronic Energy

To distort the flat band, we need a phonon that results in different phase accumulation along each of the links. Consider a general in-plane phonon, $\mathbf{u}(\mathbf{r})$, applied only to the top layer. This phonon will change the local interlayer translation and thus the local lattice stacking. While the phonon can not affect the gauge fields, it will distort their distribution throughout the supercell.

Suppose we are at position \mathbf{r} in the supercell. From Equation 3.3, we know this corresponds to an interlayer translation:

$$\mathbf{T} = F\mathbf{r}. \quad (5.11)$$

The phonon is an additional interlayer translation, $\mathbf{u}(\mathbf{r})$. Thus, the total local translation of the distorted system is $\mathbf{T}(\mathbf{r}) + \mathbf{u}(\mathbf{r})$. We want to find the point in the distorted system, \mathbf{r}' , where the local translation is equal to the local translation in the undistorted system. This occurs when \mathbf{r}' satisfies:

$$\mathbf{T}(\mathbf{r}') + \mathbf{u}(\mathbf{r}') = F\mathbf{r}. \quad (5.12)$$

Thus, we can view a phonon as a coordinate transformation:

$$\mathbf{r}' = \mathbf{r} - F^{-1}\mathbf{u}(\mathbf{r}'), \quad (5.13)$$

where F is the linear transformation between real space position and translation. Recall, we have already derived in Equation 3.3:

$$F = \begin{pmatrix} 1 - \cos \delta\theta & -\sin \delta\theta \\ \sin \delta\theta & 1 - \cos \delta\theta \end{pmatrix} \quad F^{-1} = \frac{1}{2} \begin{pmatrix} 1 & \cot \delta\theta/2 \\ -\cot \delta\theta/2 & 1 \end{pmatrix}. \quad (5.14)$$

For small amplitude phonons, we can approximate:

$$\mathbf{r}' = \mathbf{r} - F^{-1}\mathbf{u}(\mathbf{r}). \quad (5.15)$$

Thus, $F^{-1}\mathbf{u}(\mathbf{r})$ creates a flow throughout the supercell describing the distortion of real space. To calculate the phase along a link, we calculate the line integral of the same momentum function but along this new distorted path:

$$\psi = \int_{\text{Link}} \mathbf{k}_{\text{disp}}(\mathbf{r}') d\mathbf{r}'. \quad (5.16)$$

We already know a parametrization of $\mathbf{k}_{\text{disp}}(s)$ from Equation 5.6. Therefore, we write the distorted path as a function of this same parameter, $\mathbf{r}'(s)$. The difference in phase accumulated between the undistorted and distorted path is then:

$$\delta\psi = \int_{1/3}^{2/3} \mathbf{k}_{\text{disp}}(s) \left(\frac{d\mathbf{r}'(s)}{ds} - \frac{d\mathbf{r}(s)}{ds} \right) ds, \quad (5.17)$$

where \mathbf{r}' is the distorted path and \mathbf{r} is the undistorted path. Recall that for the undistorted path, $\rho = 0$. That is, the pseudovalleys displaced from the Dirac point in the same direction as the link. However, the distorted path may not have this property. In this case, ρ must be calculated.

5.3.2 Elastic Energy

We use a continuum approximation to calculate the elastic energy of the phonon. Given an in-plane phonon $\mathbf{u}(\mathbf{r})$, the elastic energy density is:

$$\mathcal{U}_{\text{elas}} = \frac{\lambda_L}{2} (\partial_x u_x + \partial_y u_y)^2 + \mu_L \left[(\partial_x u_x)^2 + (\partial_y u_y)^2 + \frac{1}{2} (\partial_x u_x + \partial_y u_y)^2 \right], \quad (5.18)$$

where we have neglected the interlayer energy change. This is justified because the

phonon will not have a large effect on the energy associated with interlayer coupling. The phonon alters the local lattice stacking in different regions of the supercell. Simply moving regions of different local lattice stacking around the supercell can not change the total interlayer energy. It is true that the phonon may expand or shrink local lattice stacking regions. For instance, the SE odd region of the supercell may expand at the expense of the SE even region. However, numerical calculations have found no energetic preference between lattice stackings at large angles [40]. In other words, the energy of SE odd or SE even regions is roughly the same. Therefore, the dominant contribution of the phonon is to change the in layer energy. Integrating this over the supercell and dividing by its area gives the elastic energy cost of the phonon per unit area:

$$U_{\text{elas}} = \frac{1}{A} \int_{\text{supercell}} \mathcal{U}_{\text{elas}}. \quad (5.19)$$

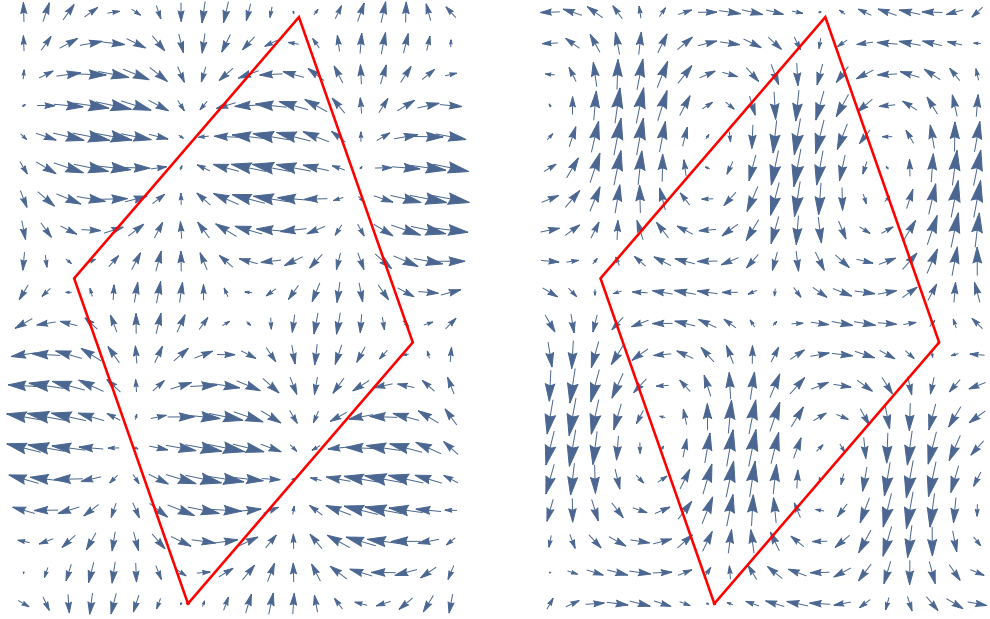
5.3.3 Calculations

We will consider two types of distortions: localized and extended. The localized phonon will be targeted to the links of the network model. It will alter the phase accumulated on these links and leave the rest of the network undisturbed. The cost of this precision is higher wavevector and higher elastic energy. The extended phonon will be low wavevector and low elastic energy. However, it will distort the entire network. In the limit of large enough system, we can make the phonon amplitude small enough to have minimum local effect but still result in significant phase accumulation along the entire link.

Extended Phonon

Consider a phonon of the form:

$$\mathbf{u}(\mathbf{r}) = u_0 \{ \hat{\mathbf{r}}_1 \sin [\mathbf{r}_1(\mathbf{r} + \mathbf{T}_2/2)] + \hat{\mathbf{r}}_2 \sin [\mathbf{r}_2(\mathbf{r} + \mathbf{T}_2/2)] \}, \quad (5.20)$$



(a) Real space phonon field

(b) Real space distortion induced by phonon

Figure 5.5: Extended phonon for system at 38.57°

where \mathbf{r}_i are the primitive reciprocal superlattice vectors and \mathbf{T}_i are the supercell vectors. In Figure 5.5, we show the real space form of the phonon and its real space distortion flow. In Figure 5.6, we show the distortion of the network caused by the flow field. One link is shortened, while the other two links are lengthened. The shortened link has the property that $w = 0$. This path is contracted, but the direction of travel on the link does not change. However, the lengthened links do have changing direction of travel. Thus, for those two links we will have to calculate w along the path.

We now turn to the calculation of the added phase. In what follows, all $\delta\psi_i$ will be calculated to lowest order in $\delta\theta$ and u_0 . In other words, we assume the system size is large and the phonon distortion is small: $u_0 \ll \delta \ll L$, where δ is the interatomic spacing of graphene.

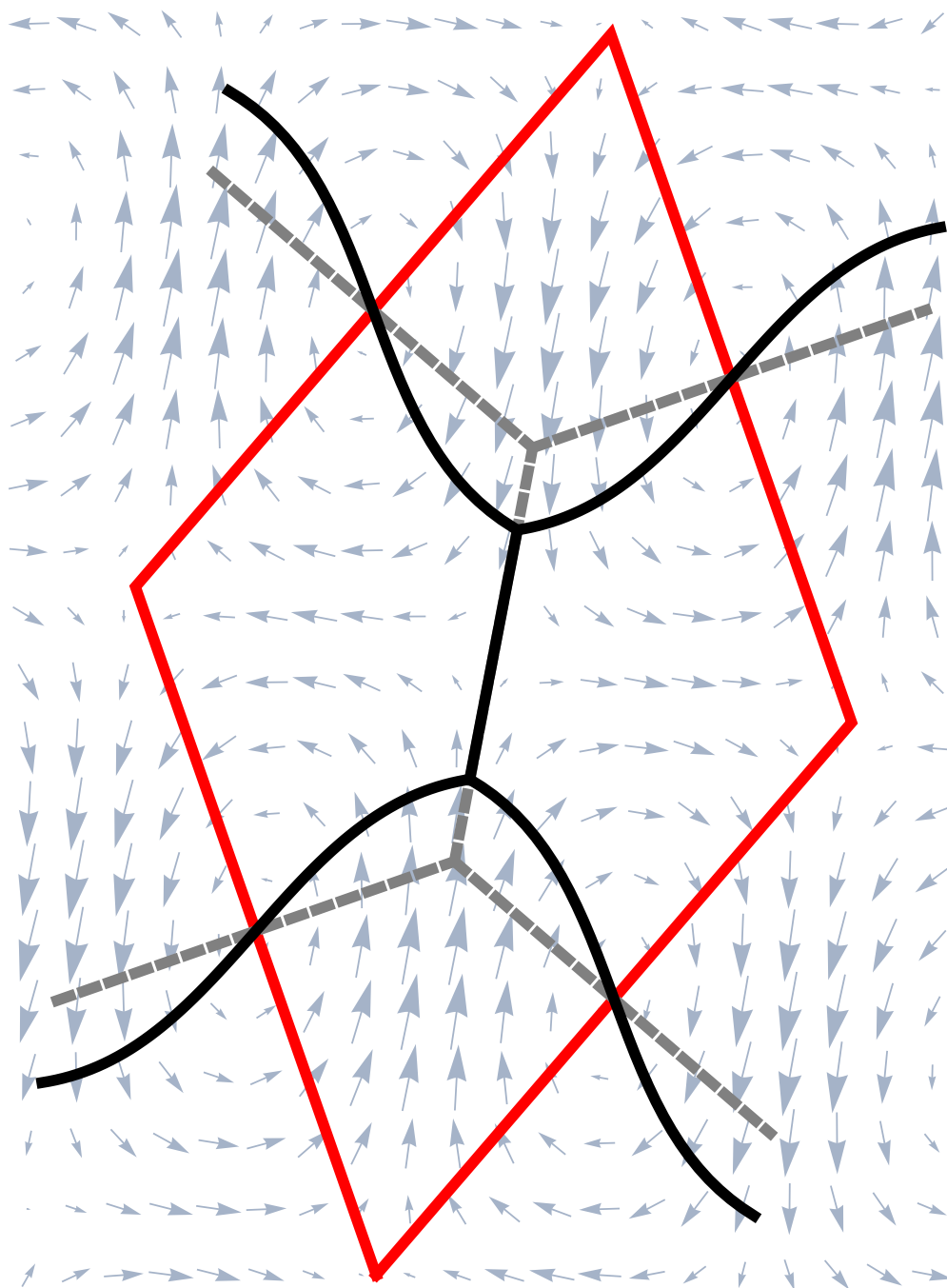


Figure 5.6: Distortion of the network caused by background phonon flow. Dashed lines are the undistorted network. Black lines are the distorted network. System is at 38.57° .

For the shortened path, we find:

$$\mathbf{r}(s) - \mathbf{r}'(s) = \frac{u_0 \sin 2\pi s}{\sqrt{7}\delta\theta} \left(\sqrt{3} \cos \pi s, \frac{9}{2} \right) + \mathcal{O}(\delta\theta^0). \quad (5.21)$$

We then calculate the line integral to find:

$$\begin{aligned} \delta\psi_3 &= \int_{1/3}^{2/3} \mathbf{k}_{\text{disp}}(s) \frac{\mathbf{r}(s) - \mathbf{r}'(s)}{ds} ds = \\ &= \frac{\sqrt{3}\pi\tilde{\gamma}_{38}u_0}{\sqrt{7}\delta\theta v} \int_{1/3}^{2/3} \cos(2\pi s) \sqrt{2 \cos 4\pi s - 164 \cos 2\pi s - 81} ds. \end{aligned} \quad (5.22)$$

The integral must be calculated numerically. We find:

$$\delta\psi_3 = \zeta \frac{2u_0\tilde{\gamma}_{38}}{v\delta\theta} + \mathcal{O}(\delta\theta^0), \quad (5.23)$$

where ζ is the integral to be numerically calculated:

$$\zeta = \frac{\sqrt{3}\pi}{2\sqrt{7}} \int_{1/3}^{2/3} \cos(2\pi s) \sqrt{2 \cos 4\pi s - 164 \cos 2\pi s - 81} ds = 2.13. \quad (5.24)$$

For the lengthened links, we repeat the same calculation:

$$\mathbf{r}(s) - \mathbf{r}'(s) = \frac{u_0}{2\sqrt{7}\delta\theta} \left\{ \sqrt{3}(\sin 2\pi s + 2 \sin 4\pi s), 4 \sin 4\pi s - 5 \sin 2\pi s \right\}. \quad (5.25)$$

Now we find:

$$\begin{aligned} \delta\psi_1 = \delta\psi_2 &= \int_{1/3}^{2/3} \mathbf{k}_{\text{disp}}(s) \frac{\mathbf{r}(s) - \mathbf{r}'(s)}{ds} ds = \\ &= -\frac{\sqrt{3}\pi\tilde{\gamma}_{38}u_0}{2\sqrt{7}\delta\theta v} \int_{1/3}^{2/3} \cos 2\pi s \sqrt{2 \cos 4\pi s - 164 \cos 2\pi s - 81} ds. \end{aligned} \quad (5.26)$$

To summarize, we found:

$$\delta\psi_1 = \delta\psi_2 = -\frac{\delta\psi_3}{2} = -\zeta \frac{2u_0\tilde{\gamma}_{38}}{v\delta\theta}. \quad (5.27)$$

Thus, to lowest order, this phonon has the nice property that the sum of added phase is zero, as required by the considerations above. Using the derived phase, we find the electronic energy gain per unit area:

$$U_{\text{elec}} = 4 \frac{v}{LA} \xi \delta\psi_1 = \frac{57\sqrt{7}\xi\zeta}{a^3} \tilde{\gamma}_{38} u_0 \delta\theta^2, \quad (5.28)$$

where the factor of 4 is for spin and valley degeneracy and ξ is calculated to be about .26. Next, we calculate the elastic energy cost per unit area of this phonon:

$$U_{\text{elas}} = \frac{56}{3a^2} (\lambda_L + 2\mu_L) \delta\theta^2 u_0^2 + \mathcal{O}(\delta\theta^3). \quad (5.29)$$

The Peierls transition will occur if we satisfy $U_{\text{elec}} < U_{\text{elas}}$, which translates to:

$$u_0 < \frac{3\sqrt{7}\xi\tilde{\gamma}_{38}\zeta}{\pi^2 a (\lambda_L + 2\mu_L)}. \quad (5.30)$$

Using the parameters given in Appendix A, along with the numerically calculated $\xi = .26$, we find $u_0 < 1.9 \times 10^{-5} \text{\AA} = 1.3 \times 10^{-5} \delta$.

The next question is whether the system can be cooled to a low enough temperature to allow this transition. To answer this, we calculate the mean energy deflection of the flat band at the phonon amplitude corresponding to the transition:

$$U_{\text{elec}} A = \frac{84\sqrt{3}\xi^2\tilde{\gamma}_{38}^2\zeta^2}{a^2(\lambda_L + 2\mu_L)\pi^2}. \quad (5.31)$$

For the same values, we find a mean deflection of $6.4 \times 10^{-8} t = 1.8 \times 10^{-7} \text{eV}$. This corresponds to a temperature of 2.1mK. The system must be cooled below this temperature to ensure we see the effect of the band distortion. At higher temperatures, thermal excitation

of the electrons will negate the energy gain of lower energy bands. In other words, electrons will not occupy many of the states that experience energy gain. Thus, this is an estimate of the critical temperature of the Peierls transition.

Localized Phonon

We now perform the same calculation for a different phonon, one that is localized along the links. We will see whether this provides a greater energy gain. We consider a phonon of the form:

$$\mathbf{u}(\mathbf{r}) = v_0 e^{-\|\mathbf{r}-\mathbf{r}_0\|^2/l_r^2} \|\mathbf{r} - \mathbf{r}_0\| 2 \sin \frac{\delta\theta}{2} \hat{\theta}, \quad (5.32)$$

where $\hat{\theta}$ is the unit vector perpendicular to $\mathbf{r} - \mathbf{r}_0$.

This phonon partially undoes the twist relative to the point \mathbf{r}_0 . The parameter v_0 is unitless and ranges from zero to one, controlling what fraction of the twist is undone. The parameter l_r controls the range of the phonon. In general, we will choose \mathbf{r}_0 to be the middle of a link and l_r small enough that the phonon decays before reaching the SE odd region. We show the phonon and its flow field in Figure 5.7. This phonon does not distort the network at all and does not affect the SE odd regions. The effect is simply to stretch the space on the link where phase accumulation is high and shrink space on the link where phase accumulation is low.

To calculate the added phase of this phonon, we first reparametrize the momentum according to:

$$s \rightarrow \frac{s}{3} + \frac{1}{2}, \quad (5.33)$$

which yields the new parametrized expression for $k(s)$:

$$k_{\text{disp}}(s) = \frac{\tilde{\gamma}_{38}}{2\sqrt{7}v} \sqrt{2 \cos 4\pi s/3 + 164 \cos 2\pi s/3 - 81} \quad s \in (-1/2, 1/2). \quad (5.34)$$

Recall that in Equation 3.4, we expanded the local lattice translation due to the twist to lowest order and found it has the same form as the phonon we are now considering. Thus, we may say that to lowest order in $\delta\theta$:

$$\mathbf{u}(\mathbf{r}) = v_0 e^{-\|\mathbf{r}-\mathbf{r}_0\|^2/l_r^2} F \mathbf{r}. \quad (5.35)$$

Using Equation 5.15 for the change of coordinates induced by the phonon:

$$\mathbf{r}' = \mathbf{r} - F^{-1} \mathbf{u}(\mathbf{r}) = \mathbf{r} - v_0 e^{-\|\mathbf{r}-\mathbf{r}_0\|^2/l_r^2} \mathbf{r}. \quad (5.36)$$

Therefore, the change of coordinates is a simple linear function. In our new parametrization, $s = 0$ corresponds to the origin of the phonon twist. Thus, we find the effect of the phonon with the following substitution:

$$s \rightarrow s \left(1 - v_0 e^{-s^2/\tilde{l}^2} \right), \quad (5.37)$$

where $\tilde{l} = l_r/L$. This substitution parametrizes the effect of the phonon. In Figure 5.8, we show how the phase accumulates along the link. The integral of the blue line is the phase accumulated without the phonon. The integral of the yellow line is the phase accumulated with the phonon. We see that by undoing the twist near the middle of the link, the local phase is increased.

To find the added phase, we first find the lowest order term of the difference in $k_{\text{disp}}(s)$

with and without the phonon, which we call δk_{disp} :

$$\delta k_{\text{disp}} = \frac{2e^{-s^2/\tilde{l}^2} \pi s (41 \sin 2\pi s/3 + \sin 4\pi s/3)}{3\sqrt{7}\sqrt{2 \cos 4\pi s/3 + 164 \cos 2\pi s/3 - 81}} \frac{\tilde{\gamma}_{38} v_0}{v} + \mathcal{O}(v_0^2). \quad (5.38)$$

We make the further observation that the s dependence of the denominator of δk_{disp} may be neglected for small \tilde{l} . In other words, localized phonons allow us to only consider the numerator near the midpoint of the link. Thus, we have:

$$\delta k_{\text{disp}} = \frac{2e^{-s^2/\tilde{l}^2} \pi s (41 \sin 2\pi s/3 + \sin 4\pi s/3)}{27\sqrt{7}} \frac{\tilde{\gamma}_{38} v_0}{v} + \mathcal{O}(v_0^2). \quad (5.39)$$

To find the accumulated phase, we integrate along the link:

$$\delta \psi = \frac{L\tilde{\gamma}_{38}}{v} \int_{-1/2}^{1/2} \delta k_{\text{disp}}(s) ds. \quad (5.40)$$

Since $\exp(-s^2/\tilde{l}^2) \ll 1$ beyond the limits of integration, we may extend the integration limits to infinity:

$$\delta \psi = \frac{L\tilde{\gamma}_{38}}{v} \int_{-\infty}^{\infty} \delta k_{\text{disp}}(s) ds = \frac{2L\tilde{\gamma}_{38}}{81\sqrt{7}v} e^{-4\tilde{l}^2\pi^2/9} (2 + 41e^{\tilde{l}^2\pi^2/3}) \tilde{l}^3 \pi^{5/2} v_0. \quad (5.41)$$

We will use two of these phonons on separate links and in opposite directions. Therefore, we will have $\delta \psi_1 = -\delta \psi_3 = \delta \psi$ and $\delta \psi_2 = 0$. The electronic energy gain per unit area is then:

$$U_{\text{elec}} = \frac{16\sqrt{7}\tilde{l}^3 \pi^{5/2}}{81\sqrt{3}a^2} e^{-4\tilde{l}^2\pi^2/9} (2 + 41e^{\tilde{l}^2\pi^2/3}) \xi \delta \theta^2 \tilde{\gamma}_{38} v_0, \quad (5.42)$$

where ξ is estimated to be around .15 and there was an extra factor of four for spin and valley degeneracy.

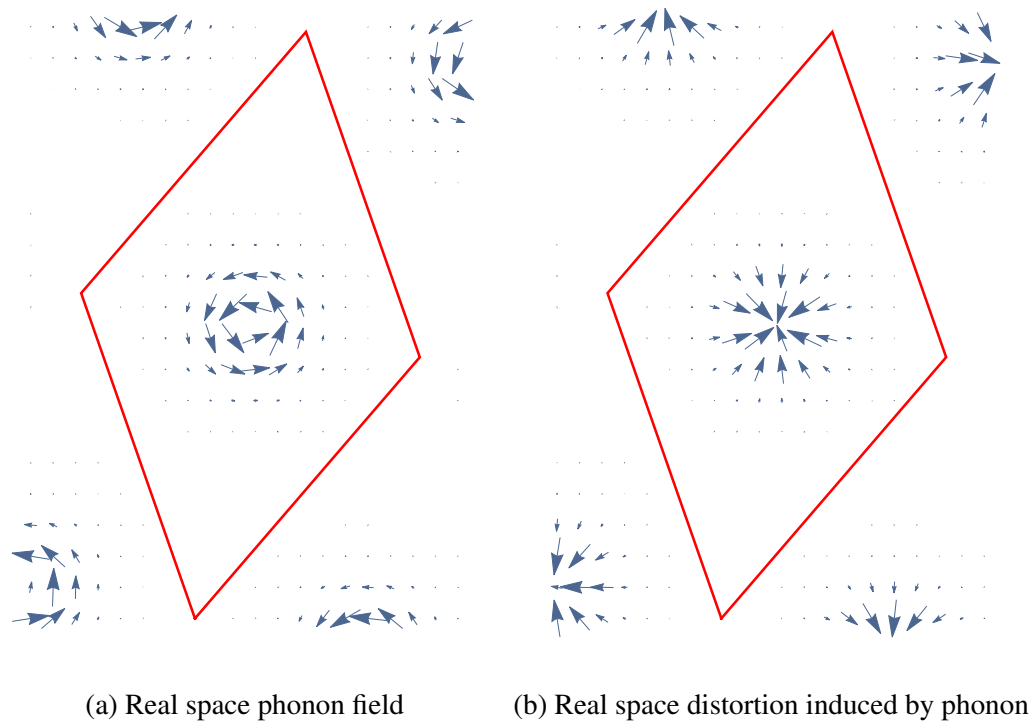


Figure 5.7: Localized phonon for system at 38.57°

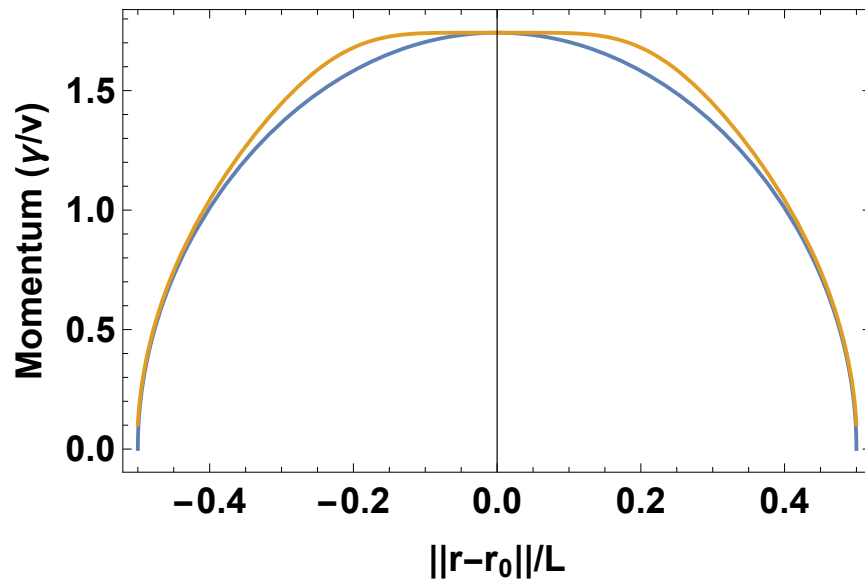


Figure 5.8: Phase along a link with (yellow) and without (blue) the phonon. Parameters are exaggerated.

Next, we calculate the elastic energy per unit area:

$$U_{\text{elas}} = \frac{1}{21A} a^2 \tilde{l}^2 \mu_L \pi v_0^2 + \mathcal{O}(\delta\theta^1), \quad (5.43)$$

where we have again extended the limits of integration to infinity. Note also there is a factor of two because we have two such phonons.

Equating the electronic and elastic energy, we find that the Peierls transition will occur at:

$$v_0 = \frac{8\sqrt{7}\tilde{l}\pi^{3/2}}{27a^2\mu_L} e^{-4\tilde{l}^2\pi^2/9} (2 + 41e^{\tilde{l}^2\pi^2/3}) \xi \tilde{\gamma}_{38}^2. \quad (5.44)$$

Using $\tilde{l} = .25$, we estimate $v_0 = 2.5 \times 10^{-4}$. The average distortion of the flat band is:

$$U_{\text{elec}} A = \frac{64\tilde{l}^4\pi^4}{2187a^2\mu_L} \xi^2 (2 + 41e^{\tilde{l}^2\pi^2/3})^2 \tilde{\gamma}_{38}^2. \quad (5.45)$$

We should choose a value for \tilde{l} that maximizes this function in order to have the best chance of observability. However, the maximum occurs around 1 which is too large to fulfill our limitations on the range of the phonon. Therefore, we choose the maximum reasonable value, $\tilde{l} = 1/4$. Thus, we estimate the mean distortion of the flat band to be 3.5×10^{-8} eV. This corresponds to 0.41 mK. This critical temperature is lower than for the extended phonon. Therefore, the extended phonon is more advantageous for a Peierls transition.

5.3.4 Verification of Phase Theory

We pause now to verify that the theory of phase connecting the network model to the full tight-binding model is approximately correct. We cannot hope for perfect agreement since our numerics cannot reach the large superlattice limit where the network model becomes exact. However, an order of magnitude check will be sufficient to verify the idea behind the theory. This idea ultimately concerns the scaling of elastic and electronic energy. Thus,

exact numerical results are not critical. However, we will see the agreement is more than sufficient.

For verification purposes, we consider a phonon:

$$\mathbf{u}(\mathbf{r}) = v_0 \|\mathbf{r} - \mathbf{r}_0\| 2 \sin\left(\frac{\delta\theta}{2}\right) \Theta(\|\mathbf{r} - \mathbf{r}_0\|^2 - l_0) \hat{\theta}. \quad (5.46)$$

That is, for positive v_0 , we partially undo the twist up to length l_0 . We do not include the gaussian prefactor in order to make the effect large enough to see for a small system. We center this phonon on the midpoint of one of the links. For a qualitative comparison, we compare the form of the flat band predicted by the network model and that obtained in a tight binding model. The result is shown in Figure 5.9. In the tight binding model, we choose $v_0 = \pm .2$ for a system with 12532 atoms at 38.6° . We see the qualitative agreement is good.

For a quantitative comparison, we compare the bandwidth of the flat band predicted by the network model and the bandwidth observed in the tight binding model. We use the same untwisting phonon with $v_0 = 1$ and a varying l_0 . In other words, we completely undo the twist on one link up to a distance of l_0 . The added phase is:

$$\delta\psi_3 = 3L \int_{1/2-l_0}^{1/2+l_0} k_{\text{disp}}(1/2) - k_{\text{disp}}(s) ds, \quad (5.47)$$

where $\tilde{l}_0 = l_0/L \in (0, 1/6)$. The integral must be computed numerically. Using the network model, we can predict the bandwidth, B , as a function of $\delta\psi_3$:

$$B = \beta \delta\psi_3 \frac{v}{L}, \quad (5.48)$$

where β is a numerically calculated dimensionless constant that captures bandwidth as a function of added phase to linear order. We calculate β from the network model by fitting a linear function to the numerically calculated bandwidth as a function of added phase, $\delta\psi_3$. We estimate $\beta = .68$. Finally, we compare the predicted bandwidth with the bandwidth

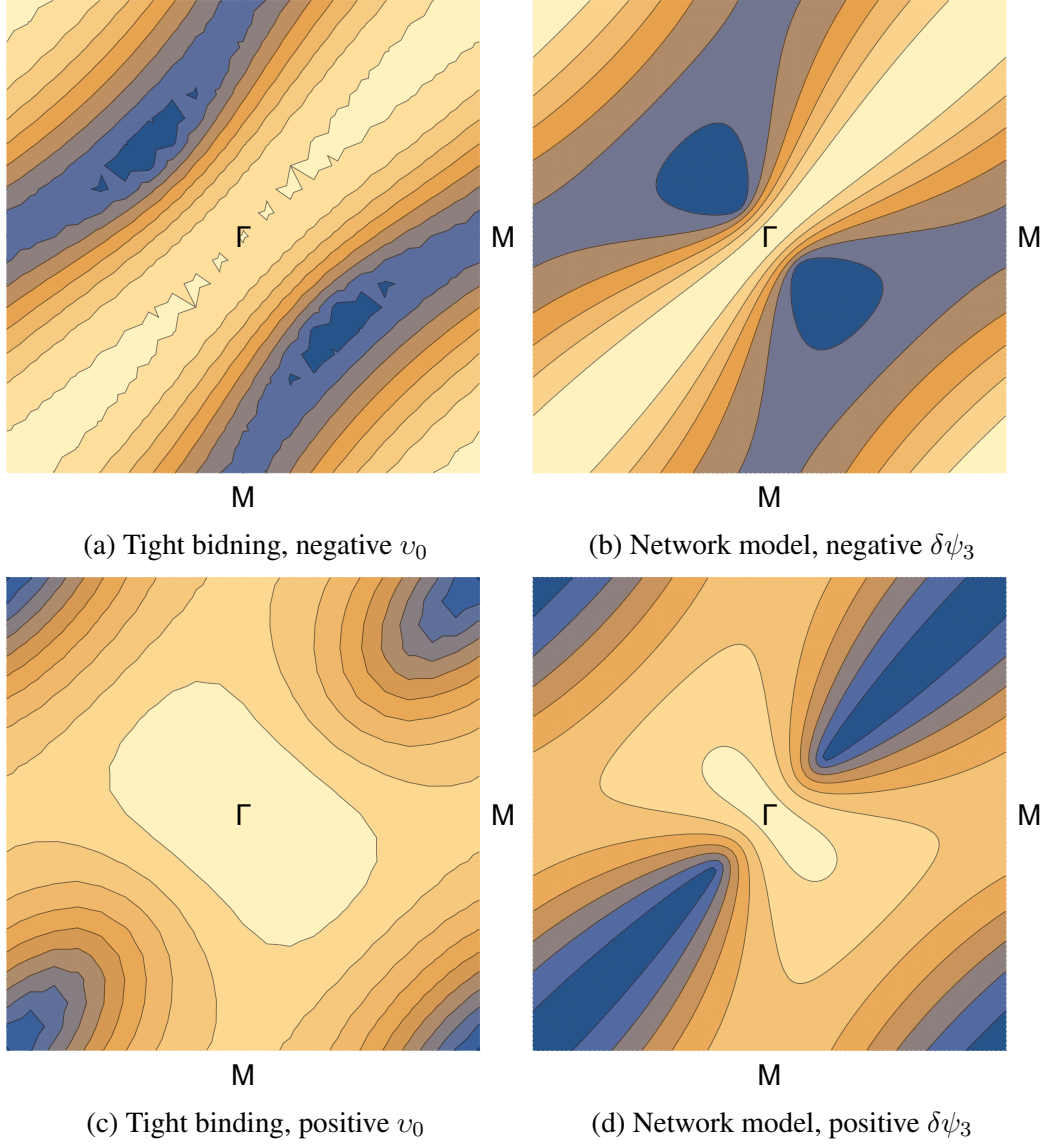


Figure 5.9: Flat band distortion for system at 38.57°

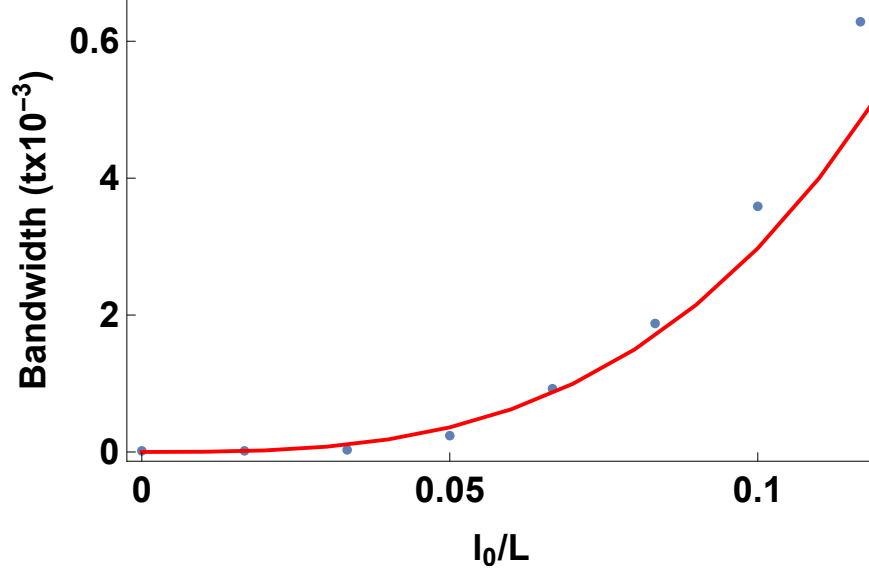


Figure 5.10: Predicted (solid) and measured bandwidth as a function of \tilde{l}_0 .

calculated directly from a tight binding model. We show the result in Figure 5.10. We see the agreement is remarkably good considering that we are not testing the limit where our analytic theory is applicable.

5.4 Peierls Transition in an Electric Field

Our previous work has focused on the possibility of a spontaneous Peierls transition in twisted bilayers at low temperature. We have demonstrated multiple mechanisms for such a transition. However, the stiffness of graphene is a formidable obstacle for observing these effects at reasonable temperatures. Thus, we turn to a transition that occurs with the application of an external electric field. In such a field, the total energy may be decreased by a flexural phonon.

This idea has several advantages. First, graphene is much more flexible in the out of plane direction, so we can expect larger phonons at a lower energy cost. Second, the applied electric field is an external experimental parameter. The experimenter can increase the field to drive the system to visible distortions and verify the dependence of distortion on field strength.

5.4.1 Electronic Energy

Consider the twisted bilayer in a uniform electric field E_0 , directed perpendicular to the plane. Suppose the bilayer has out of plane displacement $h(\mathbf{r})$ throughout the supercell. We assume h is very long wavelength. Recall from Equation 3.5, we have the effective local Hamiltonian, $H(\mathbf{r})$ throughout the supercell. By adding an electric field and out of plane phonon, our new local Hamiltonian is:

$$H_E(\mathbf{r}) = H(\mathbf{r}) + h(\mathbf{r})E_0\sigma_0\tau_0l_0. \quad (5.49)$$

We have neglected the potential difference between the layers. This is justified as long as $E_0d \ll \tilde{\gamma}_{38}$, where d is the distance between the layers. In other words, interlayer coupling dominates the potential difference between the layers. In this limit, we will still have the topologically protected network of states that produced the flat band. However, the momentum of the modes shifts due to the energy shift by $\delta k_{\text{disp}}(\mathbf{r}) = \pm h(\mathbf{r})E_0/v$, where the sign depends on whether we consider a right or left moving mode. The extra phase accumulated along a link is now the line integral:

$$\delta\psi = \int_{\text{Link}} \frac{h(\mathbf{r})E_0}{v} dr. \quad (5.50)$$

Note the sign cancels with the direction of travel of the mode. The phase difference accumulated is the same for modes travelling in both directions. Just as before, we find the total energy gain per unit area is:

$$U_{\text{elec}} = \frac{v}{LA} \xi \delta\psi, \quad (5.51)$$

where again ξ is a dimensionless constant that must be calculated numerically.

5.4.2 Elastic Energy

We use a continuum approximation for the elastic energy. For the phonon, $h(\mathbf{r})$, the elastic energy density is [36]:

$$\mathcal{U}_{\text{elas}} = \frac{\kappa_L}{2} (\partial_x^2 h + \partial_y^2 h)^2 + \frac{\lambda_L}{8} [(\partial_x h)^2 + (\partial_y h)^2]^2 + \frac{\mu_L}{2} \left[\frac{(\partial_x h)^4}{2} + \frac{(\partial_y h)^4}{2} + (\partial_x h \partial_y h)^2 \right], \quad (5.52)$$

where λ_L and μ_L are Lamé parameters and κ_L is the bending rigidity. Once again, the total elastic energy per unit area is the integral of the energy density over the supercell divided by the area of the supercell. We will also have to multiply by two because we are deforming both layers.

$$U_{\text{elas}} = \frac{2}{A} \int_{\text{supercell}} \mathcal{U}_{\text{elas}}. \quad (5.53)$$

5.4.3 Calculations

We will consider two types of phonons: extended and localized. The advantages and disadvantages are the same as in the in-plane case. The extended phonon is longer wavelength and lower energy. The localized phonon will not distort the network.

Extended Phonon

Consider a phonon of the form:

$$h(\mathbf{r}) = u_0 \cos(\mathbf{r}_1 \mathbf{r}), \quad (5.54)$$

where \mathbf{r}_1 is a reciprocal superlattice vector. We show the form of this phonon in Figure 5.11. We choose this phonon for its simplicity and low wavevector. We calculate the added

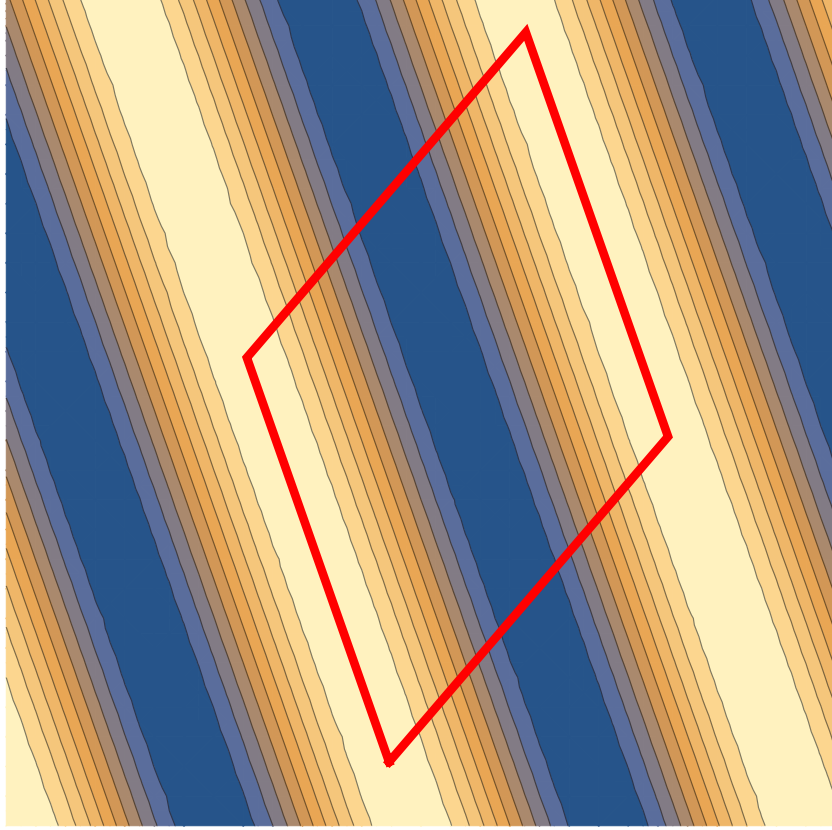


Figure 5.11: Extended phonon throughout the supercell. Displacement of both graphene layers is out of the page.

phases and find:

$$\delta\psi_1 = -\delta\psi_2 = -\delta\psi_3 = \frac{3\sqrt{3}E_0u_0L}{2\pi v} = \frac{3aE_0u_0}{2\sqrt{7}\delta\theta\pi v} + \mathcal{O}(\delta\theta^0). \quad (5.55)$$

Note that the sum of phases is not zero. We enforce $\sum \psi_i = 0$ by subtracting $-\delta\psi_1/3$ from all bands, as explained in Section 5.2.2.

The electronic energy gain per unit area is then:

$$U_{\text{elec}} = \frac{84\xi\delta\theta^2 E_0u_0}{\pi a^2}, \quad (5.56)$$

where ξ is measured to be about .18. The elastic energy per unit area is:

$$U_{\text{elas}} = \frac{784\pi^4(8\kappa_L u_0^2 + 3\mu_L u_0^4)}{9a^4} \delta\theta^4 + \mathcal{O}(\delta\theta^5). \quad (5.57)$$

To find the value of u_0 for which a Peierls transition occurs, we set equal U_{elec} and U_{elas} . The result is a cubic equation in u_0 of the form:

$$0 = (u_0^3 + \eta_1 u_0) \delta\theta^2 + \eta_2, \quad (5.58)$$

where $\eta_1 = 8\kappa/3\mu_L$ and $\eta_2 = -9a^2\xi E_0/28\mu_L\pi^5$. The lowest order term in the solution for u_0 is:

$$u_0 = \left(\frac{9a^2\xi E_0}{28\mu_L\pi^5\delta\theta^2} \right)^{1/3}. \quad (5.59)$$

Now we must ensure our solution fulfills the appropriate limits. We need $E_0 d \ll \tilde{\gamma}_{38}$ to ensure the interlayer coupling dominates the energy and the network is still present. Therefore, we set $E_0 d = \omega \tilde{\gamma}_{38}$ where $\omega \ll 1$. This translates to an electric field on the order of meV/Å. Therefore:

$$u_0 = \left(\frac{9a^2\xi\omega\tilde{\gamma}_{38}}{28\mu_L\pi^5 d \delta\theta^2} \right)^{1/3}. \quad (5.60)$$

Using $\omega = .1$ and $\delta\theta = .00017$ (our estimate for appearance of the network model), we estimate $u_0 = .46\delta = .64\text{\AA}$. This is well within the depth resolution of a scanning tunneling microscope, and should be visible. We also find the average deflection of the flat band is:

$$U_{\text{elec}} A = \frac{6\sqrt{3}\xi\omega\tilde{\gamma}_{38}u_0}{d\pi}, \quad (5.61)$$

which we estimate to be $2.6 \times 10^{-5}\text{eV}$. This corresponds to a temperature of 300mK. This is a reasonable temperature for experimental conditions.

Localized Phonon

Consider a phonon of the form:

$$h(\mathbf{r}) = u_0 e^{-\|\mathbf{r}-\mathbf{r}_0\|^2/l^2}. \quad (5.62)$$

That is, we have a Gaussian displacement with range l . We will place a phonon of opposite sign on each of two links, ensuring the added phase sums to zero. The added phase along one of the links is:

$$\delta\psi = \int_{-\infty}^{\infty} \frac{E_0 h(r)}{v} dr = \frac{E_0 l \sqrt{\pi} u_0}{v}, \quad (5.63)$$

where we have extended the limits of integration due to the short range of the phonon. Therefore, the electronic energy gain per unit area is:

$$U_{\text{elec}} = \frac{56 E_0 \tilde{l} \sqrt{\pi}}{\sqrt{3} a^2} u_0 \xi \delta\theta^2, \quad (5.64)$$

where $\tilde{l} = l/L$ and ξ is estimated to be .15. Next, we calculate the elastic energy per unit area, remembering to include a factor of four for the two localized phonon sites and two layers:

$$U_{\text{elas}} = \frac{1}{A} \left(\frac{168 \kappa_L \pi}{a^2 \tilde{l}^2} u_0^2 \delta\theta^2 + \frac{21 \mu_L \pi}{2 a^2 \tilde{l}^2} u_0^4 \delta\theta^2 + \frac{83349 \lambda_L \pi}{4096 a^6 \tilde{l}^6} u_0^8 \delta\theta^6 \right) + \mathcal{O}(u_0^{10}) \mathcal{O}(\delta\theta^7). \quad (5.65)$$

We can discard the highest order term in $\delta\theta$ and we have the same form of equation as in the extended case. By equating the elastic and electronic energies, we estimate that a Peierls transition will occur for:

$$u_0 = \left(\frac{8 \xi E_0 a^2 \tilde{l}^3}{21 \sqrt{\pi} \mu_L \delta\theta^2} \right)^{1/3} = \left(\frac{8 \xi \omega \tilde{\gamma}_{38} a^2 \tilde{l}^3}{21 \sqrt{\pi} d \mu_L \delta\theta^2} \right)^{1/3}, \quad (5.66)$$

where we have again made the substitution $E_0 = \omega\tilde{\gamma}_{38}/d$. Choosing $\tilde{l} = .1$, $\delta\theta = .00017$, and $\omega = .1$, we see $u_0 = 0.26\delta = .36\text{\AA}$. The average deflection of the flat band is:

$$U_{\text{elec}}A = \frac{4\xi\omega\tilde{\gamma}_{38}\tilde{l}\sqrt{\pi}u_0}{d} = \left(\frac{512\xi^4 E_0^4 \tilde{l}^6 \pi a^2}{21\mu_L \delta \theta^2} \right)^{1/3}. \quad (5.67)$$

Using the same parameters, we estimate this to equal $2.6 \times 10^{-6}\text{eV}$. This corresponds to a temperature of 30mK.

5.4.4 Verification

Once again, we verify our theory of phase accumulation using a tight binding model. First, we look for qualitative agreement between the network model and tight binding model. In the tight binding model, we apply an extra poential on one link of the form:

$$V_0(\mathbf{r}) = V_0\Theta(\|\mathbf{r} - \mathbf{r}_0\| - l_0). \quad (5.68)$$

That is, we shift the energy of both layers by V_0 if we are in a region within l_0 of the midway point of a link. This is the same effect we are considering with the phonon and electric field in Equation 5.49. In this case, $V_0 = E_0 h$, where we have $h = 0$ when $l > l_0$. The tight binding model should agree with the network model with added phase on the link. Thus, we can check the results of tight binding model against the results of the network model to ensure the effect is the same. We diagonalize a tight binding model for a system at 38.6° with $\tilde{l}_0 = l_0/L = .3$. The result is shown in Figure 5.12. We see good qualitative agreement with the network model.

Now we predict the bandwidth of the flat band with our network model and compare it to the tight binding model. The added phase is:

$$\delta\psi_3 = \frac{1}{v} \int_{1/2-l_0}^{1/2+l_0} V_0 = \frac{2V_0 l_0}{v} \quad (5.69)$$

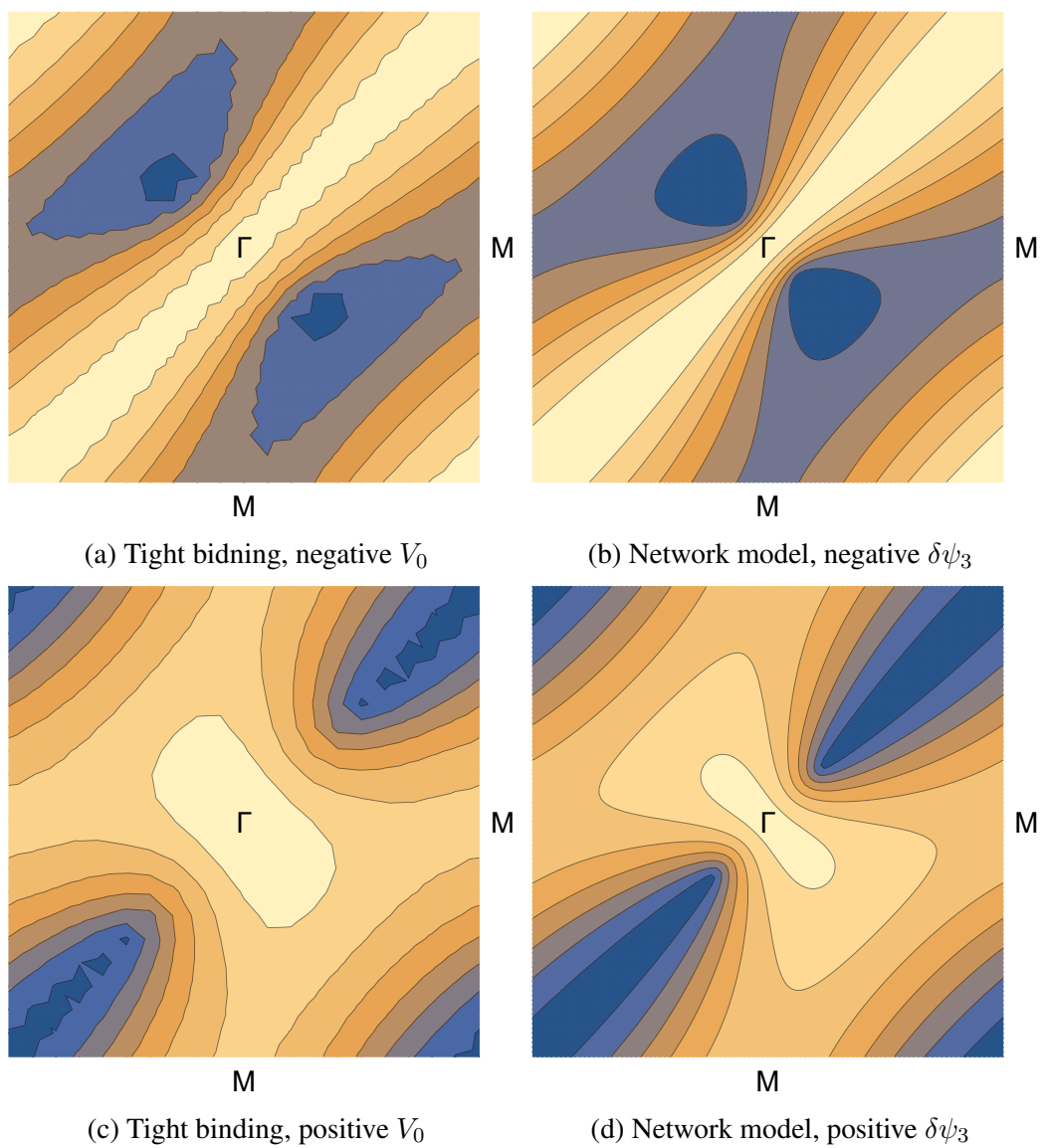


Figure 5.12: Flat band distortion for system at 38.6°

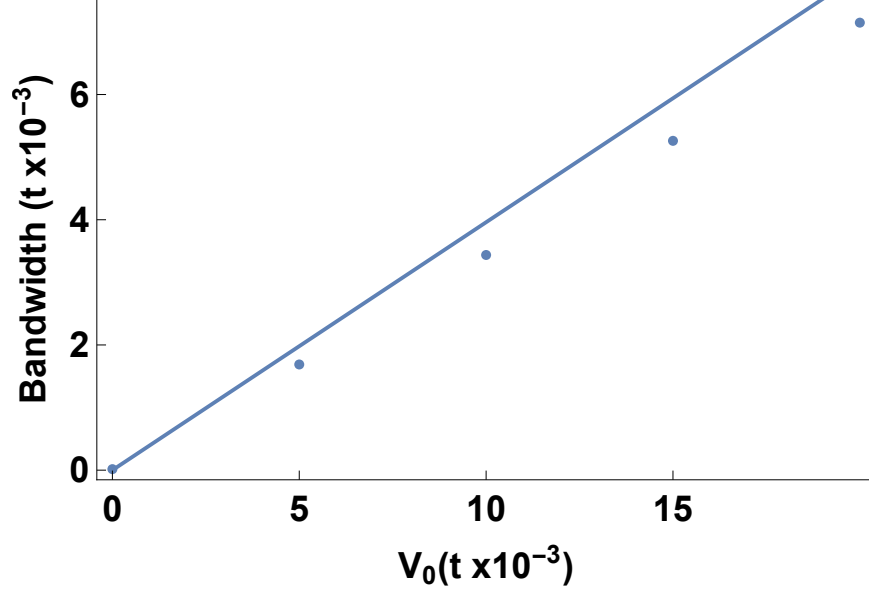


Figure 5.13: Predicted (solid) and measured bandwidth as a function of V_0 .

The predicted bandwidth, B , is:

$$B = \frac{\delta\psi_3\beta v}{L} = 2V_0\tilde{l}_0\beta, \quad (5.70)$$

where β is a dimensionless constant capturing the linear relationship of added phase to bandwidth in the network model. It is numerically estimated to be .68. We compare this prediction as a function of the bias strength V_0 to the result of a tight binding model in Figure 5.13. We see good agreement.

5.5 Summary

We have presented evidence for a Peierls like transition in the non-perturbative regime of twisted bilayer graphene. Our arguments for this transition originate in the scaling presented in Section 5.1. Thus, the existence of these transitions is guaranteed. We calculated an estimate for the critical temperature below which these effects should be visible in experiments. These temperatures are attainable.

A good method for detection is observation of the change in density of states with

temperature. As the twisted bilayer is cooled, the density of states at the energy of the flat band should soften and spread out as the flat band distorts. In the case of the bilayer in an electric field, the out of plane distortion is large enough to be observed with a scanning tunneling microscope.

In neither case did we try to optimize the phonon to produce the largest energy gain possible. Our calculations are a lower bound on the critical temperature and distortion size in the real system. Likely, there are other phonons that produce greater energy gains and larger effect sizes. However, because our calculation serves as a lower bound, we know any larger effect will be observable in experiments. Thus, our work has established the existence of a Peierls transition in this bilayer system.

CHAPTER 6

CONCLUSION

In this thesis, we had two main objectives. First, we extended the theory of twisted bilayer graphene to large angles in the non-perturbative limit. Second, we sought new regimes for Peierls transitions in bilayer graphene.

In Chapters 2 and 3, we accomplished the first objective. We provided a complete characterization of the interlayer coupling of bilayer graphene and targeted the non-perturbative regime, where the underlying physics is not understood. We demonstrated the existence of non-perturbative physics at large angles and the surprising flat bands that result. Furthermore, we provided an effective low energy model based on the band topology of this system.

In Chapters 4 and 5, we accomplished the second objective. We provided three different graphene bilayer setups where a Peierls transition is guaranteed by scaling arguments. The first system we examined was in the perturbative regime. This yielded a Peierls transition with temperature too low to be observed. However, the final two systems were in the non-perturbative regime. We found Peierls transitions that are observable in feasible experiments.

Bilayer graphene has proven to be a system with remarkably rich physics. In this thesis, we have seen how the interplay of Dirac equations and commensuration leads to regimes of surprising complexity. These ideas are not just applicable to graphene bilayers but all layered two dimensional materials. The construction of such heterostructures is just beginning [41, 42]. Further development and application of these methods in these new systems should lead to interesting results in the future.

Appendices

APPENDIX A

PHYSICAL CONSTANTS OF GRAPHENE

We present useful physical constants for graphene that we use throughout this thesis.

Constant	Symbol	Value	Reference
Graphene Lattice Constant	a	2.46 \AA	[16]
Interlayer Spacing	d	3.35 \AA	[24]
In-layer Hopping	t	2.8 eV	[16]
Fourier Component 0°	$\tilde{\gamma}_0$	$.11 \text{ eV}$	[24]
Fourier Component 38°	$\tilde{\gamma}_{38}$	$.0023 \text{ eV}$	[22]
Lamé Coefficient	λ	2 eV \AA^{-2}	[36]
Lamé Coefficient	μ	10 eV \AA^{-2}	[36]
Bending Rigidity	κ	1 eV	[36]

APPENDIX B

GAUGE FIELDS NEAR 0°

We present the non-zero gauge fields for a system near 0° . For simplicity, we choose a non-orthogonal basis: $\mathbf{r} = t_1 \mathbf{T}_1 + t_2 \mathbf{T}_2$ such that \mathbf{T}_1 and \mathbf{T}_2 are the supercell basis vectors.

$$\mathcal{A}_{0,x} = \tilde{\gamma}_0 [\cos(2\pi t_1) + \cos(2\pi t_2) + 1] \quad (\text{B.1})$$

$$\mathcal{A}_{0,y} = \tilde{\gamma}_0 [\sin(2\pi t_2) - \sin(2\pi t_1)] \quad (\text{B.2})$$

$$\mathcal{A}_{x,x} = \tilde{\gamma}_0 [\cos(2\pi t_1) - \cos^2(\pi t_2)] \quad (\text{B.3})$$

$$\mathcal{A}_{x,y} = \frac{\tilde{\gamma}_0}{2} [-2 \sin(2\pi t_1) - \sin(2\pi t_2)] \quad (\text{B.4})$$

$$\mathcal{A}_{y,x} = -\tilde{\gamma}_0 \sqrt{3} \sin^2(\pi t_2) \quad (\text{B.5})$$

$$\mathcal{A}_{y,y} = \frac{\tilde{\gamma}_0}{2} \sqrt{3} \sin(2\pi t_2) \quad (\text{B.6})$$

APPENDIX C

GAUGE FIELDS NEAR 38.2°

We present the non-zero gauge fields for a system near 38.2° . For simplicity, we choose a non-orthogonal basis: $\mathbf{r} = t_1 \mathbf{T}_1 + t_2 \mathbf{T}_2$ such that \mathbf{T}_1 and \mathbf{T}_2 are the supercell basis vectors.

We also use the symbol $w = \tan^{-1} \left(\frac{11}{5\sqrt{3}} \right) / 2$.

$$\begin{aligned} \mathcal{A}_{0,x} = & \frac{\tilde{\gamma}_{38}}{4\sqrt{7}(5+\sqrt{3})} \left(- \left(3 + 5\sqrt{3} \right) \sin \left[\frac{2}{7}\pi (t_1 + 5t_2) \right] + \left(5 + \sqrt{3} \right) \cos \left[\frac{2}{7}\pi (t_1 + 5t_2) \right] + \right. \\ & \left. 2 \cos (\pi t_1) \left\{ \left(3 + 5\sqrt{3} \right) \sin \left[\frac{1}{7}\pi (5t_1 + 4t_2) \right] + \left(5 + \sqrt{3} \right) \cos \left[\frac{1}{7}\pi (5t_1 + 4t_2) \right] \right\} \right) \end{aligned} \quad (\text{C.1})$$

$$\begin{aligned} \mathcal{A}_{0,y} = & \frac{\tilde{\gamma}_{38}}{4\sqrt{7}(5+\sqrt{3})} \left(\left(5 + \sqrt{3} \right) \sin \left[\frac{2}{7}\pi (t_1 + 5t_2) \right] + \left(3 + 5\sqrt{3} \right) \cos \left[\frac{2}{7}\pi (t_1 + 5t_2) \right] + \right. \\ & \left. 2 \cos (\pi t_1) \left\{ \left(3 + 5\sqrt{3} \right) \cos \left[\frac{1}{7}\pi (5t_1 + 4t_2) \right] - \left(5 + \sqrt{3} \right) \sin \left[\frac{1}{7}\pi (5t_1 + 4t_2) \right] \right\} \right) \end{aligned} \quad (\text{C.2})$$

$$\begin{aligned}
\mathcal{A}_{x,x} = & \frac{\tilde{\gamma}_{38}}{2} \left(\sin \left(\frac{12\pi t_1}{7} + \frac{4\pi t_2}{7} + \frac{\pi}{12} - w \right) + \right. \\
& \sin \left(\frac{2\pi t_1}{7} + \frac{10\pi t_2}{7} + \frac{\pi}{12} - w \right) + \\
& \cos \left(-\frac{12\pi t_1}{7} - \frac{4\pi t_2}{7} + \frac{\pi}{4} - w \right) + \\
& \cos \left(-\frac{2\pi t_1}{7} + \frac{4\pi t_2}{7} + \frac{\pi}{4} - w \right) - \\
& \cos \left(-\frac{2\pi t_1}{7} + \frac{4\pi t_2}{7} + \frac{\pi}{12} + w \right) - \\
& \left. \cos \left(\frac{2\pi t_1}{7} + \frac{10\pi t_2}{7} + \frac{\pi}{12} + w \right) \right)
\end{aligned} \tag{C.3}$$

$$\begin{aligned}
\mathcal{A}_{x,y} = & \frac{\tilde{\gamma}_{38}}{2} \left(\sin \left(-\frac{12\pi t_1}{7} - \frac{4\pi t_2}{7} + \frac{\pi}{4} - w \right) - \right. \\
& \sin \left(-\frac{2\pi t_1}{7} + \frac{4\pi t_2}{7} + \frac{\pi}{4} - w \right) + \\
& \sin \left(-\frac{2\pi t_1}{7} + \frac{4\pi t_2}{7} + \frac{\pi}{12} + w \right) - \\
& \sin \left(\frac{2\pi t_1}{7} + \frac{10\pi t_2}{7} + \frac{\pi}{12} + w \right) + \\
& \cos \left(\frac{12\pi t_1}{7} + \frac{4\pi t_2}{7} + \frac{\pi}{12} - w \right) - \\
& \left. \cos \left(\frac{2\pi t_1}{7} + \frac{10\pi t_2}{7} + \frac{\pi}{12} - w \right) \right)
\end{aligned} \tag{C.4}$$

$$\begin{aligned}
\mathcal{A}_{y,x} = & \frac{\tilde{\gamma}_{38}}{2} \left(\sin \left(-\frac{12\pi t_1}{7} - \frac{4\pi t_2}{7} + \frac{\pi}{4} - z \right) + \right. \\
& \sin \left(-\frac{2\pi t_1}{7} + \frac{4\pi t_2}{7} + \frac{\pi}{4} - w \right) + \\
& \sin \left(-\frac{2\pi t_1}{7} + \frac{4\pi t_2}{7} + \frac{\pi}{12} + w \right) + \\
& \sin \left(\frac{2\pi t_1}{7} + \frac{10\pi t_2}{7} + \frac{\pi}{12} + w \right) - \\
& \cos \left(\frac{12\pi t_1}{7} + \frac{4\pi t_2}{7} + \frac{\pi}{12} - w \right) - \\
& \left. \cos \left(\frac{2\pi t_1}{7} + \frac{10\pi t_2}{7} + \frac{\pi}{12} - w \right) \right)
\end{aligned} \tag{C.5}$$

$$\begin{aligned}
\mathcal{A}_{y,y} = & \frac{\tilde{\gamma}_{38}}{2} \left(\sin \left(\frac{12\pi t_1}{7} + \frac{4\pi t_2}{7} + \frac{\pi}{12} - w \right) - \right. \\
& \sin \left(\frac{2\pi t_1}{7} + \frac{10\pi t_2}{7} + \frac{\pi}{12} - w \right) - \\
& \cos \left(-\frac{12\pi t_1}{7} - \frac{4\pi t_2}{7} + \frac{\pi}{4} - w \right) + \\
& \cos \left(-\frac{2\pi t_1}{7} + \frac{4\pi t_2}{7} + \frac{\pi}{4} - w \right) + \\
& \cos \left(-\frac{2\pi t_1}{7} + \frac{4\pi t_2}{7} + \frac{\pi}{12} + w \right) - \\
& \left. \cos \left(\frac{2\pi t_1}{7} + \frac{10\pi t_2}{7} + \frac{\pi}{12} + w \right) \right)
\end{aligned} \tag{C.6}$$

$$\begin{aligned}
\mathcal{A}_{z,x} = & \frac{3\tilde{\gamma}_{38}}{4\sqrt{7}(5+\sqrt{3})} \left((3+5\sqrt{3}) \sin \left[\frac{2}{7}\pi(t_1+5t_2) \right] + 3(5+\sqrt{3}) \cos \left[\frac{2}{7}\pi(t_1+5t_2) \right] + \right. \\
& \left. 2\cos(\pi t_1) \left\{ 3(5+\sqrt{3}) \cos \left[\frac{1}{7}\pi(5t_1+4t_2) \right] - (3+5\sqrt{3}) \sin \left[\frac{1}{7}\pi(5t_1+4t_2) \right] \right\} \right)
\end{aligned} \tag{C.7}$$

$$\begin{aligned}
\mathcal{A}_{z,y} = & -\frac{3\tilde{\gamma}_{38}}{4\sqrt{7}(5+\sqrt{3})}(-3(5+\sqrt{3})\sin\left[\frac{2}{7}\pi(t_1+5t_2)\right] + (3+5\sqrt{3})\cos\left[\frac{2}{7}\pi(t_1+5t_2)\right] + \\
& 2\cos(\pi t_1)\left\{3(5+\sqrt{3})\sin\left[\frac{1}{7}\pi(5t_1+4t_2)\right] + (3+5\sqrt{3})\cos\left[\frac{1}{7}\pi(5t_1+4t_2)\right]\right\}) \\
& \tag{C.8}
\end{aligned}$$

SYMBOL INDEX

A , 56	Δ , 75	\mathcal{G}_c , 17
a , 3	δK , 20	\mathcal{G}_c^i , 17
$\mathbf{A}_C(\boldsymbol{\kappa})$, 6	δK_c , 20	\mathbf{G}_l^i , 18
A_i , 33	δk_{disp} , 96	\mathbf{G}_l , 14
\mathbf{a}_i , 2	$\delta \mathbf{K}_n$, 70	
\mathbf{A}_i , 33	$\delta \psi$, 80	$H_{\perp, vv'}^{(1)}$, 19
$\mathcal{A}_{i,j}$, 33	$\delta \psi_i$, 84	\bar{H} , 9
$a_{\boldsymbol{\kappa}\sigma}$, 3	$\delta \theta$, 24	\bar{H}_{\perp} , 9
α , 23	Det, 35	H_{BG} , 8
$a_{l\sigma i}$, 13	δ_i , 2	H_E , 102
$a_{l\sigma\kappa}$, 14	diag $_i$, 54	$H_{(l)}$, 52
$a_{\sigma i}$, 3	$\delta_{l\sigma B}$, 14	H_l , 13
A_0 , 14		$h(\mathbf{r})$, 102
	$\mathcal{E}(\theta)$, 19	H_{\perp}^i , 55
B , 52	ϵ , 49	$H_{\perp}^{(n)}(\theta)$, 15
$\mathbf{B}_C(\boldsymbol{\kappa})$, 6	E_0 , 102	H^0 , 23
β , 99		$H^{(v)}$, 4
\mathbf{b}_i , 2	F , 31	H_0 , 54
	$f(\mathbf{r})$, 13	H^{θ} , 8
\mathbf{C} , 6	$\tilde{f}(\boldsymbol{\kappa})$, 14	$H^{\theta/2}$, 9
χ , 19		H_{\parallel}^u , 71
C_v , 7	γ , 57	H_{\perp}^u , 71
	$\tilde{\gamma}_c$, 17	$H_{\perp}^{u,-}$, 73
δ , 3	$\tilde{\gamma}_c^i$, 17	$H_{\perp}^{u,+}$, 73
d , 102	$\tilde{\gamma}(\boldsymbol{\kappa})$, 14	

H^0 , 4	l_0 , 56	rot, 31
I_3 , 51	M , 49	$\mathbf{R}_{lj\sigma}^u$, 73
J_j , 50	m , 67	SE, 11
$J_{j,0}$, 50	μ , 85	S_i , 31
$J_{j,i}$, 50	μ_L , 76	σ_i , 5
$J_{j,r}$, 50	N_A , 56	σ_l , 54
$J_0(r)$, 14	N_c , 17	T , 31
K , 71	n_c^i , 17	t, 3
\mathbf{k} , 4	\mathcal{N}_c , 17	τ_i , 5
κ , 3	$\mathcal{O}(\theta)$, 19	θ , 8
κ_L , 103	ω , 105	$\hat{\theta}$, 31
$\mathbf{k}_{\text{disp}}(\mathbf{r})$, 82	P , 33	T_i , 83
k_f , 68	p , 59	T_1 , 59
k_i , 51	ϕ , 5	t_{\parallel} , 71
\mathbf{K}_{lv} , 11	ψ_i , 82	U , 49
\mathbf{K}_{lv}^n , 70	$ \psi\rangle_I$, 48	U_{elas} , 70
\mathbf{K}_v , 3	$ \psi_{lg}(\boldsymbol{\kappa})\rangle$, 15	$\mathcal{U}_{\text{elas}}$, 76
L , 49	$ \psi_{lgv}\rangle$, 15	U_{elec} , 70
l , 8	$ \psi\rangle_O$, 48	U_i , 49
λ , 51	\mathbf{q}_l^i , 52	$\mathbf{u}(\mathbf{r})$, 70
λ_j , 50	$q(\theta)$, 19	v_0 , 94
λ_L , 76	\mathbf{R}_i , 31	u_0 , 68
$\lambda^{(0)}$, 51	\mathbf{r}_i , 90	v , 4
$\lambda_j^{(0)}$, 50	$\mathbf{R}_{i\sigma}$, 3	V_0 , 38
l_r , 56	$\mathbf{R}_{l\sigma i}$, 13	w , 83
L_0 , 23		

ξ , 85

ζ , 92

REFERENCES

- [1] P. Wallace, Phys. Rev. **71**, 622 (1947).
- [2] A. K. Geim and K. S. Novoselov, Nat. Mater. **6**, 183 (2007).
- [3] K. Novoselov *et al.*, Nature **438**, 197 (2005).
- [4] C. Berger *et al.*, J. Phys. Chem. B **108**, 19912 (2004).
- [5] Y. Zhang, Y.-W. Tan, H. L. Stormer, and P. Kim, Nature **438**, 201 (2005).
- [6] C. Berger *et al.*, Science **312**, 1191 (2006).
- [7] Y.-M. Lin *et al.*, Science **327**, 662 (2010).
- [8] F. Schwierz, Nature nanotechnology **5**, 487 (2010).
- [9] C. L. Kane and E. J. Mele, Phys. Rev. Lett. **95**, 146802 (2005).
- [10] K. Novoselov *et al.*, Science **315**, 1379 (2007).
- [11] K. Bolotin *et al.*, Nature **462**, 196 (2009).
- [12] J. Hicks, K. Shepperd, F. Wang, and E. H. Conrad, J. Phys. D: Appl. Phys. **45**, 154002 (2012).
- [13] J. A. Garlow *et al.*, Sci. Rep. **6** (2016).
- [14] J. Hass *et al.*, Phys. Rev. Lett. **100**, 125504 (2008).
- [15] E. McCann, *Graphene Nanoelectronics: Metrology, Synthesis, Properties and Applications* (Springer Berlin Heidelberg, Berlin, Heidelberg, 2012), chap. Electronic Properties of Monolayer and Bilayer Graphene, pp. 237–275.
- [16] A. C. Neto, F. Guinea, N. Peres, K. S. Novoselov, and A. K. Geim, Rev. Mod. Phys. **81**, 109 (2009).
- [17] M. Berry, Proc. Royal Soc. A **392**, 45 (1984).
- [18] B. A. Bernevig and T. L. Hughes, *Topological insulators and topological superconductors* (Princeton University Press, 2013).
- [19] T. Fukui *et al.*, J. Phys. Soc. Jpn. **81**, 114602 (2012).
- [20] M. Ezawa, J. Phys. Soc. Jpn. **84**, 121003 (2015).
- [21] Z. Tan *et al.*, ACS Nano (2016).

- [22] E. J. Mele, Phys. Rev. B **81**, 161405 (2010).
- [23] E. J. Mele, Phys. Rev. B **84**, 235439 (2011).
- [24] J. M. B. Lopes dos Santos, N. M. R. Peres, and A. H. Castro Neto, Phys. Rev. Lett. **99**, 256802 (2007).
- [25] R. Bistritzer and A. H. MacDonald, Proc. Natl. Acad. Sci. U.S.A. **108**, 12233 (2011).
- [26] Y. Cao *et al.*, Nature doi:10.1038/nature26154, (2018).
- [27] Y. Cao *et al.*, Nature doi:10.1038/nature26160, (2018).
- [28] G. Trambly de Laissardière, D. Mayou, and L. Magaud, Nano Lett. **10**, 804 (2010).
- [29] P. San-Jose and E. Prada, Phys. Rev. B **88**, 121408 (2013).
- [30] J. C. Song, A. V. Shytov, and L. S. Levitov, Phys. Rev. Lett. **111**, 266801 (2013).
- [31] H.K. Pal, S.T. Spitz, and M. Kindermann, arXiv preprint arXiv:1803.07060 (2018).
- [32] F. Zhang, A. H. MacDonald, and E. J. Mele, PNAS **110**, 10546 (2013).
- [33] S.T. Spitz and M. Kindermann, to be published.
- [34] V. M. Pereira, R. M. Ribeiro, N. M. R. Peres, and A. H. Castro Neto, Phys. Rev. B **79**, 045421 (2009).
- [35] Y. Ono and T. Hamano, J. Phys. Soc. Jpn. **69**, 1769 (2000).
- [36] P. L. de Andres, F. Guinea, and M. I. Katsnelson, Phys. Rev. B **86**, 144103 (2012).
- [37] H. K. Pal, S. Carter, and M. Kindermann, arXiv preprint arXiv:1409.1971 (2014).
- [38] R. E. Peierls *Quantum theory of solids* No. 23 (Oxford University Press, 1955).
- [39] J. Chalker and P. Coddington, J. Phys. C **21**, 2665 (1988).
- [40] J.-W. Jiang, B.-S. Wang, and T. Tabczuk, J. Appl. Phys. **113** 194304 (2013).
- [41] A. Geim and I. Grigorieva, Nature **499**, 7459 (2013).
- [42] K. Novoselov *et al.*, Science **353**, 9439 (2016).